博士論文

Study on Flexible Spintronic Devices Based on Magnetoelastic Coupling

(磁気弾性結合を利用したフレキシブル
スピントロニクスデバイスに関する研究)

太田 進也

Contents

Chapter 1

Introduction

1.1 Spintronics and flexible electronics

Spintronics is a research field that use degree of freedom of spin as well as charge of electron. One of the most important discovery is the giant magnetoresistance (GMR) effect [1, 2]. The GMR effect couples magnetization (spin) and electric resistance, enabling magnetic field control of the electric charge transport. Magnetoresistance effects, including the GMR effect, attract many researchers to the field since it is not only scientifically interesting but also industrially useful for the development of magnetic sensors or information storage devices. In recent years, magnetic random access memory, which has non-volatility, is being developed as the researches on the spin transfer torque [3] or the spin orbit torque [4, 5] effects have advanced and magnetization control by not magnetic field but electric current has become possible. In the future, information storage or processing devices will be developed to reduce their energy consumption and increase their information recording density.

On the other hand, flexible electronics devices have attracted attentions recently [6–8]. Either partial or full use of organic materials adds stretchability, bendability, or lightness to conventional electronic devices based on metal or semi-conductor. Such characteristics are expected to be used for soft robotics, wearable sensors and devices. Furthermore, if a large area printing process can be applied, the production cost will be reduced and flexible devices will become more practical [9].

In this thesis, flexible spintronics is studied. A flexible spintronic device was firstly

reported in 1992, where GMR multilayers were fabricated on a flexible polyimide substrate [10]. Later, wearable imperceptible magnetic sensor was realized using an extremely thin (~14 μm) flexible substrate [11] [Fig.1.1 (a)]. Even apart from them, many examples for flexible spintronic devices are reported [12–31]. One of the characteristics required for these flexible spintronic devices is that their properties are invariant with a strain caused by the deformation of the device [Fig.1.1 (b)]. Use of strain-insensitive magnetic material or pre-
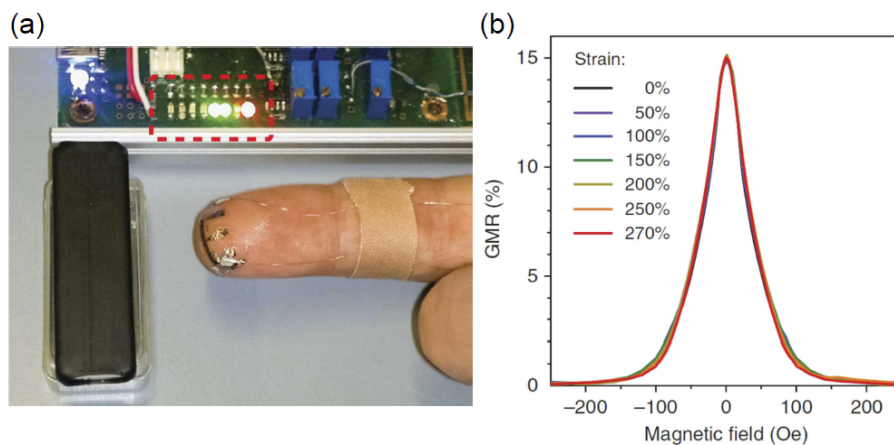
Figure 1.1: (a) A wearable magnetic sensor mounted on a finger. (b) Magnetoresistance curves invariant with strain application. These figures are taken from Ref. [11].

stretched substrate is effective to achieve this requirement [11]. In contrast to these devices, the aim of this thesis is to add mechanical function by proactively utilizing the strain applied to the device. The magnetoelastic coupling, which is introduced in the next section, connects the strain with the magnetism and accordingly with the spintronic properties.

1.2 Magnetoelastic coupling

In this section, the magnetoelastic coupling [32–34] is introduced. Representative phenomena of the magnetoelastic coupling are magnetostriction and inverse magnetostriction effects. The latter is particularly important for the realization of mechanical functions.

1.2.1 Magnetostriction effect

The magnetostriction is a phenomenon that the size of a ferromagnetic material changes when a magnetization of the ferromagnetic material is changed by a magnetic field. When a demagnetized material with its length l is magnetized by magnetic field parallel to the length measurement direction to saturation and the length changes to $l + \Delta l$, the magnetostriction constant λ is defined as

$$\lambda = \frac{\Delta l}{l}. \tag{1.1}$$

Thus a positive (negative) magnetostriction constant corresponds to an expansion (contraction) of the material in the magnetized direction. The absolute value of the magnetostriction constant of $3d$-transition metal ferromagnets is on the order of 10^{-6}-10^{-5}. In general, the value depends on the crystal orientation. Two independent values of λ_{100} and λ_{111} are usually used for a cubic crystalline case.

Origin of the magnetostriction and inverse magnetostriction effects is expressed using the energy of the interaction between spins. The dipole interaction is particularly important. The dipole interaction energy w of a pair of parallel spins is expressed as

$$w(r, \cos \varphi) = w(r) \left(\cos^2 \varphi - \frac{1}{3} \right), \tag{1.2}$$

where r is a distance between the parallel spin pair and φ is the angle between the axis that connects the two spins and the direction of the spins. Though the above equation is for a spin pair, when considering all the nearest spin pairs in cubic crystal and energy changes with a strain (strain tensor : ε_{xx}, ε_{yy}, ε_{zz}, ε_{xy}, ε_{yz}, ε_{xz}), the magnetoelastic coupling energy E_{magel}

is derived as

$$E_{\mathrm{magel}} = B_1 \left[\varepsilon_{xx} \left(\alpha_x^2 - \frac{1}{3} \right) + \varepsilon_{yy} \left(\alpha_y^2 - \frac{1}{3} \right) + \varepsilon_{zz} \left(\alpha_z^2 - \frac{1}{3} \right) \right]$$
$$+ B_2 (\varepsilon_{xy} \alpha_x \alpha_y + \varepsilon_{yz} \alpha_z \alpha_y + \varepsilon_{xz} \alpha_x \alpha_z). \tag{1.3}$$

Here, $(\alpha_x, \alpha_y, \alpha_z)$ are direction cosines of x, y, z axes, respectively. Higher order terms of $(\alpha_x, \alpha_y, \alpha_z)$ are ignored. Coefficients B_1, B_2 are the magnetoelastic coupling constants. When a magnetization direction is $(\alpha_x, \alpha_y, \alpha_z)$, the strain $(\varepsilon_{xx}, \varepsilon_{yy}, \varepsilon_{zz}, \varepsilon_{xy}, \varepsilon_{yz}, \varepsilon_{xz})$ that minimizes the sum of E_{magel} and the elastic energy E_{el}, is the spontaneous strain of the magnet. In cubic crystal, E_{el} is expressed using the elastic constants c_{11}, c_{12}, c_{44} as

$$E_{\mathrm{el}} = \frac{1}{2} c_{11} \left(\varepsilon_{xx}^2 + \varepsilon_{yy}^2 + \varepsilon_{zz}^2 \right) + \frac{1}{2} c_{44} \left(\varepsilon_{xy}^2 + \varepsilon_{yz}^2 + \varepsilon_{zx}^2 \right)$$
$$+ c_{12} (\varepsilon_{yy} \varepsilon_{zz} + \varepsilon_{zz} \varepsilon_{xx} + \varepsilon_{xx} \varepsilon_{yy}). \tag{1.4}$$

The conditions that minimize $E = E_{\mathrm{magel}} + E_{\mathrm{el}}$, i.e. $\partial E / \partial \varepsilon_{ij} = 0$ $(i, j = x, y, z)$, determine the strain tensor to be

$$\varepsilon_{ii} = \frac{B_1}{c_{12} - c_{11}} \left(\alpha_i^2 - \frac{1}{3} \right),$$
$$\varepsilon_{ij} = \frac{B_2}{c_{44}} \alpha_i \alpha_j \ (i \neq j). \tag{1.5}$$

Here the strain in a measurement direction, whose direction cosines is $(\beta_x, \beta_y, \beta_z)$, is

$$\lambda = \varepsilon_{xx} \beta_x^2 + \varepsilon_{yy} \beta_y^2 + \varepsilon_{zz} \beta_z^2 + \varepsilon_{xy} \beta_x \beta_y + \varepsilon_{yz} \beta_y \beta_z + \varepsilon_{xz} \beta_x \beta_z. \tag{1.6}$$

Therefore, when the magnetization directs [100], the strain in the same direction λ_{100} is derived to be

$$\lambda_{100} = -\frac{2}{3} \frac{B_1}{c_{11} - c_{12}}, \tag{1.7}$$

from $(\alpha_x, \alpha_y, \alpha_z) = (\beta_x, \beta_y, \beta_z) = (1, 0, 0)$. Similarly in [111] direction,

$$\lambda_{111} = -\frac{1}{3} \frac{B_2}{c_{44}}, \tag{1.8}$$

from $(\alpha_x, \alpha_y, \alpha_z) = (\beta_x, \beta_y, \beta_z) = (\frac{1}{\sqrt{3}}, \frac{1}{\sqrt{3}}, \frac{1}{\sqrt{3}})$. Thus, the magnetoelastic coupling constants are related to the magnetostriction and elastic constants.

1.2.2 Inverse magnetostriction effect

When a strain is externally applied to a magnet, the magnetism is changed. This is called inverse magnetostriction effect. Eq. (1.3) shows magnetic anisotropy, i.e. energy dependence on the magnetization direction $(\alpha_x, \alpha_y, \alpha_z)$, when the strain tensor ε_{ij} is externally determined. For simplicity, Eq. (1.3) is often expressed as

$$E_{\text{magel}} = -\frac{3}{2}\lambda_{\text{eff}} Y \varepsilon \cos^2 \theta, \tag{1.9}$$

where λ_{eff} and Y are the effective magnetostriction constant and Young's modulus, respectively. In this thesis, ε is a uniaxial strain applied to a flexible substrate, on which magnetic film is deposited, and its coefficient $B_{\text{eff}} = 3\lambda_{\text{eff}}Y/2$ is an effective magnetoelastic coupling constant. Here $B_{\text{eff}} > 0$, accordingly $\lambda_{\text{eff}} > 0$, means that the material becomes easier to be magnetized in the direction of an external tensile strain. The angle between the strain axis and magnetization direction is expressed by θ If the magnet is poly-crystalline, λ_{eff} is known to be connected to λ_{100} and λ_{111} as

$$\lambda_{\text{eff}} \approx \frac{2\lambda_{100} + 3\lambda_{111}}{5}. \tag{1.10}$$

In case of an oriented poly-crystalline material, which is often the case for thin films, the discussion is rather complex [35]. The effective magnetoelastic coupling constant for in-plane magnetization (B_{xy}) in a (111)-oriented poly-crystalline film is derived to be

$$B_{xy} = -\frac{B_1 + B_2}{3}(1 + \nu_{\text{sub}}), \tag{1.11}$$

where ν_{sub} is Poisson's ratio, i.e. $\varepsilon_{yy} = -\nu_{\text{sub}}\varepsilon_{xx}$. See Appendix A.1 for the details of the derivation.

Using the inverse magnetostriction effect, electric field manipulation of magnetic properties has been reported using a piezoelectric element [36–43]. A strain is applied to a thin

magnetic film deposited on the piezoelectric element when an electric field is applied to the piezoelectric element. Figure 1.2 shows magnetization property of Ni film depending on the electric field applied to the $BaTiO_3$ substrate. Under 4 kV/cm, the hysteresis curve is almost square. On the other hand, the squareness of the hysteresis curve reduces under -0.6 kV/cm as a result of a magnetic anisotropy change with the inverse magnetostriction effect. In addition to the control of the basic magnetic properties, change in a velocity of magnetic domain wall motion [44, 45] has also been observed and a logic device based on it has been demonstrated [46]. Although these researches based on the piezoelectric elements are interesting and have potentials for practical applications, the magnetic anisotropy changes are usually not so large because of the limitation of the amount of the strain that can be applied via piezoelectric elements ($\varepsilon \sim 0.1\%$).
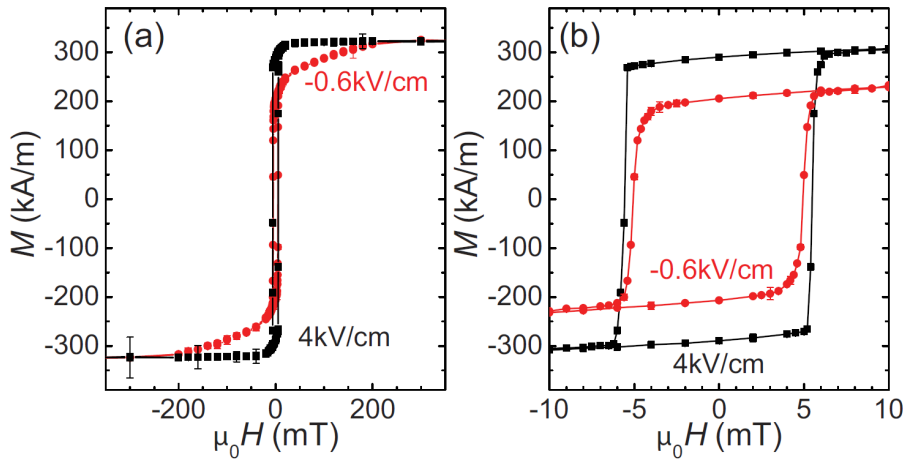
Figure 1.2: (a) Magnetization curves depending on applied electric fields. (b) Enlarged view of low magnetic field region. These figures are taken from Ref. [43].

Use of a flexible film as a substrate largely enhances the limit of the applicable strain. The elastic limit of flexible films is usually $\varepsilon \sim$1-2%. Although the plastic deformation occurs at $\varepsilon \sim$0.1% in usual bulk metals, increase in yield strength in thin films on a flexible substrate has been experimentally observed [47–49]. Figure 1.3 shows yield strength dependence on thickness of Cu film. The yield strength of the thinnest film (~100 nm) exceeds 1000 MPa, which corresponds to the yield strain of ~1%. Therefore, the yield strength of a thin (~10 nm) metal film is expected to be even larger. Though the Hall-Petch relation, the strengthening by a smaller grain size, can be an origin of the strengthening in thin films, Ref. [49] has reported

that the strengthening in thin films occurs even in the sample series with the same grain size. A model considering the plastic constraint at the interface of metal and the substrate seems to simulate the relation most successfully so far [50].
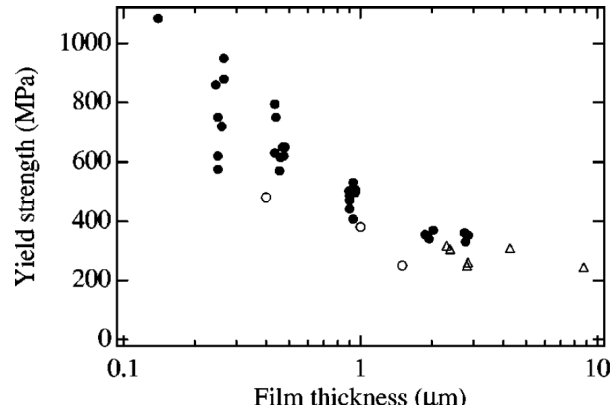
Figure 1.3: Yield strength of Cu films on a polyimide film dependence on Cu film thickness. The figure is taken from Ref. [49].

In fact, the large modulation of magnetic anisotropy with a large strain on a magnetic thin film on a flexible substrate has been observed [51–54]. Figure 1.4 shows magnetic easy axis switching with a tensile strain application. A 6 nm TbFeCo alloy layer with under
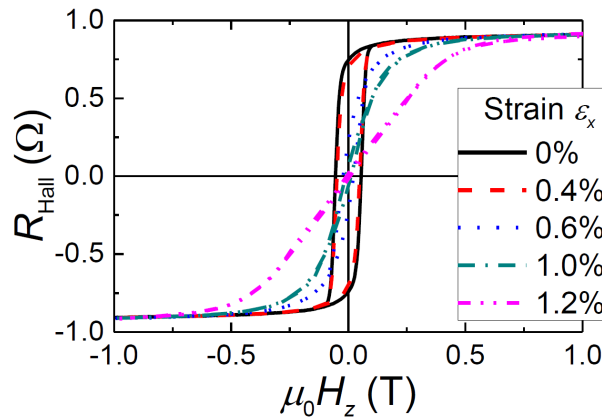
Figure 1.4: Anomalous Hall resistance vs magnetic field perpendicular to film plane under different strain. The figure is taken from Ref. [53] and modified.

and capping Pt layers was deposited on a flexible substrate. The anomalous Hall resistance was measured while sweeping a magnetic field perpendicular to the film plane. The curves correspond to magnetization curves since the anomalous Hall resistance is proportional to

the perpendicular component of the magnetization. Without strain, the sample showed the easy axis magnetization curve, suggesting perpendicular magnetic anisotropy. On the other hand, when a strain is applied, it changes to the hard axis magnetization curve, suggesting that the easy axis is switched to the in-plane direction with positive B_{eff}. Although the λ_{eff} derived using Eq. 1.9 was much smaller than the magnetostriction constant of bulk TbFeCo, the change in the magnetic anisotropy field is huge (sub-Tesla order) mainly due to the large strain. It was also confirmed that the change is reversible.

The large magnetic anisotropy change was also confirmed using a simple substance of $3d$ transition metal Ni [54] (Fig.1.5). The magnetic anisotropy was measured using the
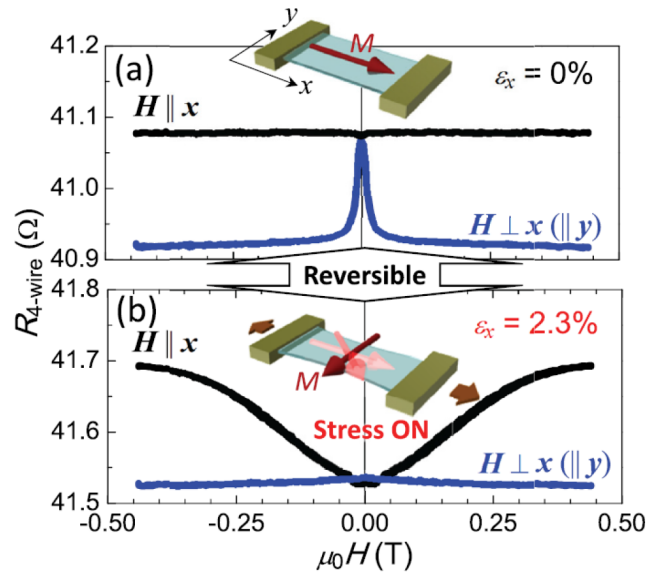
Figure 1.5: Magnetoresistance curves with (b) and without (a) strain. Black and blue lines are measured under magnetic field in x and y directions, respectively. The figure is taken from Ref. [54].

anisotropic magnetoresistance effect. The magnetic easy axis of Ni was in x direction before the strain application. It changes to y direction with the application of tensile strain in x direction due to the negative B_{eff} of Ni.

1.3   Purpose and outline of this thesis

In this section, the purpose and the outline of this thesis is stated. The aim of the thesis is to utilize the inverse magnetostriction effect proactively in flexible spintronic devices. The inverse magnetostriction effect should have been suppressed in the conventional spintronic devices in order to avoid any characteristic change. However, as shown in the previous section, the magnetic easy axis direction can easily be changed by a strain application to the flexible substrate. In other words, magnetization direction is controlled by a strain. Combination of this phenomenon with other effects can result in new functions. For example, use of magnetoresistance effects enables change of resistance by the strain, leading to a function of strain sensing.

After this Chap. 1, the general introduction for this thesis, experimental methods that are in common for the following experiments are explained in Chap. 2. Chapter 3 shows the inverse magnetostriction effect of Co thin films with various structure. Analysis of the actual strain that is applied to the Co layer using the extended X-ray absorption fine structure spectroscopy is also done.

In Chap. 4, the GMR effect is combined with the inverse magnetostriction effect. The (pseudo) spin valve structure, consisting of two ferromagnetic layers separated by a non-magnetic layer, is investigated. Strain effect on the magnetoresistance curve is elucidated and the function of the strain sensing is confirmed. Furthermore, use of the exchange bias, which is an internal magnetic field from an antiferromagnetic layer, improves the sensitivity and makes it unnecessary to apply an external field. Thanks to the improvement, a brief demonstration of bio-metric measurement is conducted.

In Chap. 5, formation of the magnetic tunnel junctions on a flexible substrate is performed in order to enhance the magnetoresistance ratio. The magnetoresistance ratio of ~200% is obtained, which is comparable to that of the sample on a rigid substrate. Strain effects and durability are also checked. In addition, features of the magnetoelastic strain sensors are discussed

In Chap. 6, heat transport properties are controlled by the strain application, in contrast to the control of the electric transport properties in the former chapters. The anomalous Ettingshausen effect, which produces a heat current depending on the magnetization direction,

is mainly controlled by the inverse magnetostriction effect.

Finally in Chap. 7, conclusion and the future research directions are stated.

Chapter 2

Experimental methods

In this chapter, experimental methods that are in common for experiments in the following chapters are shown.

2.1 Sample preparation

2.1.1 Flexible substrates

Poly-ethylene naphthalate (PEN) or polyimide films were used as flexible substrate. The PEN has a molecular structure similar to that of the poly-ethylene terephthalate often used for beverage bottles, with better characteristics in mechanical strength, chemical stability, or heat resistance. The PEN films used in this thesis are Teonex® Q65H (Dupont-Teijin Films Ltd.) with thickness of 38 or 50 μm. Teonex® Q65H has been developed for use in flexible electronics, having high transparency and surface flatness. A surface image of Teonex® Q65H measured with the atomic force microscope (AFM) is shown in Fig. 2.1 (a). The surface roughness R_a is sub-nanometer. The strain-stress curve of the PEN film measured using a tensile machine (see Sec. 2.2.2 for details) is shown in Fig. 2.1 (b). The linear relationship is maintained up to around $\varepsilon = 2\%$, where reversible strain application to the film is expected. The Young's modulus is 6.2 GPa.

The polyimide film was used when thermal treatment was necessary. The glass transition temperature T_g of the polyimide is around 300°C (cf. $T_g \sim 120$°C for PEN). Kapton® EN (Dupont-Toray Co., Ltd.) with various product lines for thickness or UPILEX® S50 (Ube
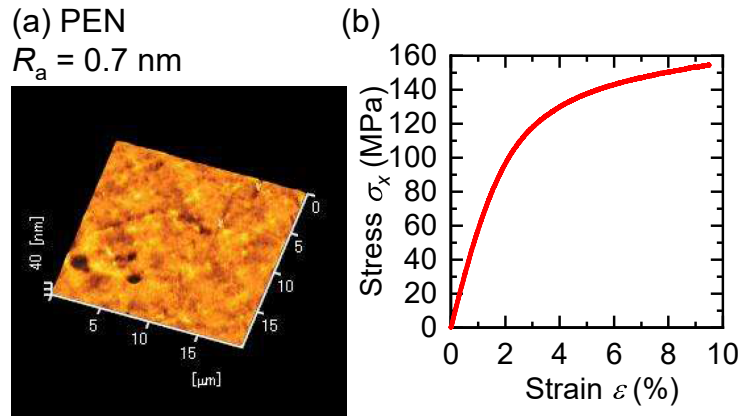
Figure 2.1: (a) An AFM image of the surface of PEN film (Teonex® Q65H) in the area of 20×20 μm^2. (b) A strain-stress curve of the PEN film.

Industries, Ltd.) with a flat surface. Figures 2.2 (a) and (b) show the AFM images of the Kapton® and UPILEX®, respectively. In contrast to the rough surface of Kapton, UPILEX has a flat surface comparable to the PEN substrate. Although T_g is no more than 400°C, reduction of the elastic modulus is moderate over T_g, especially in the UPILEX®. Therefore, annealing of the sample up to 500°C is performed in chapter 5. Magnetic thin films are formed on these flexible substrates.
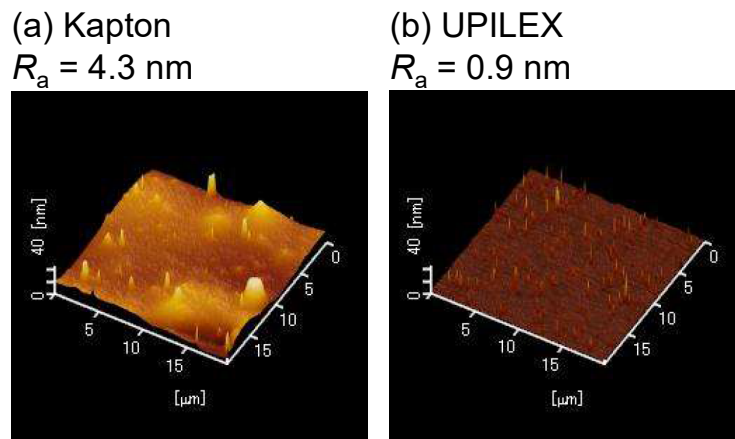
Figure 2.2: AFM images in the area of 20×20 μm^2 for (a) Kapton® 200EN and (b) UPILEX® S50.

15

2.1.2 Film deposition

Magnetic films used in this thesis were deposited by radio frequency (RF) sputtering manufactured by EIKO Engineering (see Fig. 2.3). The sputtering method is one of the physical vapor deposition methods. Noble gas is ionized, accelerated and crashed into a plate of target material by an RF voltage. Though the voltage source is not necessarily be alternative for deposition of metal, the RF voltage was used, enabling deposition of insulative materials (e.g. MgO). Atoms of the target material is then, burst out from the plate and adhere to the substrate or the sample. Ar and Xe gases were used and the pressure was maintained to be around 0.6 and 0.2 Pa, respectively, during the deposition. The base pressure of the sputtering machine was on the order of 10^{-7}-10^{-6} Pa. Thickness of the deposited film and the deposition rate were monitored by the quartz crystal microbalance thickness monitor. The deposition rate of materials was in the range of 0.1-0.3 Å/s in the thickness monitor. The actual thickness of the deposited films can be checked with X-ray reflectivity measurements using SmartLab® (Rigaku Corporation). Ratio of the actual thickness and the thickness displayed in the thickness monitor was checked in advance for each material.
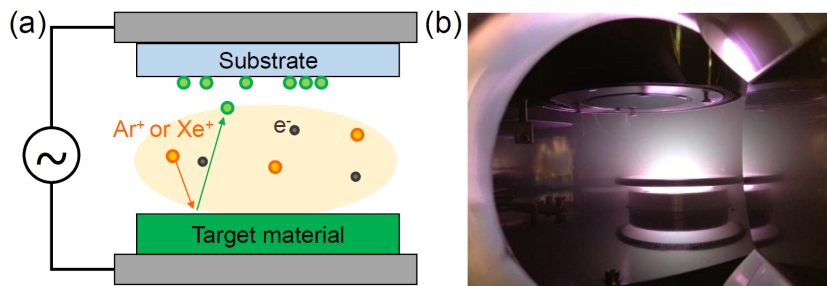
Figure 2.3: (a) A schematic and (b) a picture of the sputtering machine.

2.1.3 Fabrication process

The deposited films were processed into a pattern of thin wires and electrodes for the 4-wire resistance measurement with the photolithography and Ar ion milling, which is schematically shown in Fig. 2.4. Details of the procedure is written below. See Sec. 5.2 for the procedure for fabricating magnetic tunnel junctions.
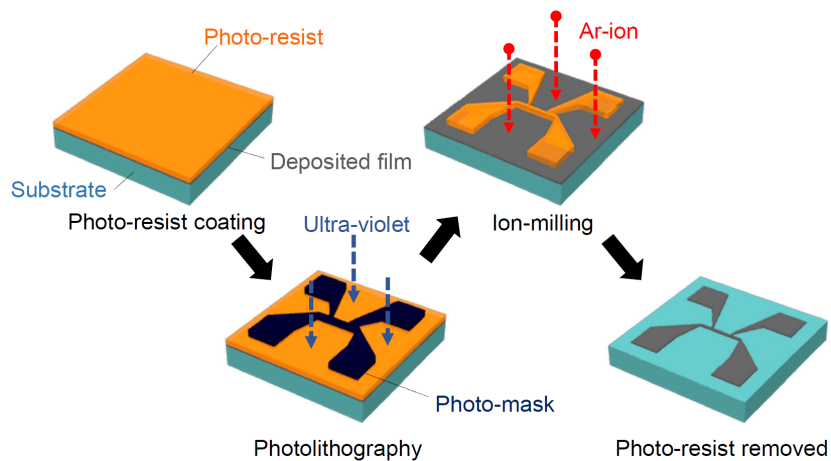
Figure 2.4: Schematics of sample fabrication process by photolithography and Ar ion milling.

1. The positive photo-resist microposit® S1813G (Shipley) was coated on the sample surface. A spin coater MS-B100 (MIKASA Co., Ltd.) was used to rotate the sample at the speed around 4000 rpm. The sample was baked on a hot plate at 90°C for no less than 2 minutes.

2. A photo-mask made of glass and a Cr layer patterned into an intended shape was put on the sample with the photo-resist and ultra-violet was irradiated on them for 30 s. Mask aligner M-1S (MIKASA Co., Ltd.) was used for this procedure.

3. The sample was put into microposit® MFCD-26 developer (Rohm and Haas Company) for about 30 s. This makes the photo-resist where exposed to the ultra-violet resolves selectively.

4. The sample was etched with Ar ion milling apparatus IBE-NS10-TU-DC (EIKO Engineering). This method etches the area not covered by the photo-resist by crashing the ionized high energy Ar into the sample surface . The etching time depends on the total film thickness (e.g. about 2 minutes for 10-nm-thick metal). Films on flexible substrates required longer time compared to those on rigid substrate. This seems to be related to oxidization of the bottom layer as can be seen in Fig. 4.5 in Chap. 4. After the milling, the residual photo-resist was removed by the ultrasonic cleaning in acetone and ethanol.

During the procedures, double sided tapes were used to fix the flexible sample, instead of vacuum chucks or clamping tools usually used for processing rigid samples.

The sample after the above procedure can be measured with a probing device. On the other hand, wires were connected to the samples for tensile testing. Cu wires of 0.05 mm in diameter were connected using the CircuitWorks® Conductive Epoxy (Chemtronics). The epoxy was dried for a few hours at room temperature. Figure 2.5 (a) shows a single device, whose four electrodes are connected. Figure 2.5 (b) shows a sample cut into a strip for the tensile testing.

(a) (b)
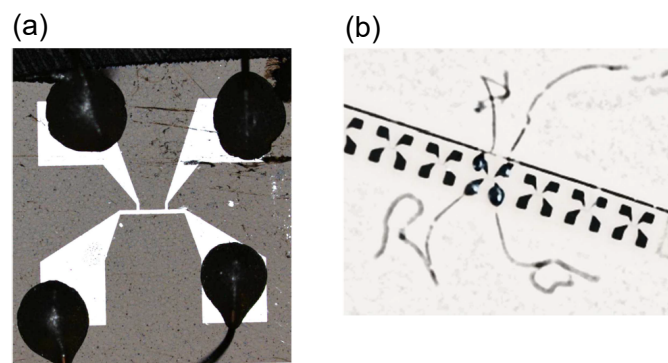
Figure 2.5: (a) A microscope image of a single pattern with four Cu wires connected by Conductive Epoxy. (b) A strip for tensile testing. One of the devices has wires.

2.2 Strain application

In this section, methods of tensile testing for the sample prepared with above procedure (Fig. 2.5) are explained. Tensile jigs and automated motor-driven tensile machines were used. Although the tensile jigs are inferior to the auto-tensile machine in the precision of strain application, the tensile jigs provide higher degree of freedom for surrounding experimental setup.

2.2.1 Tensile jig
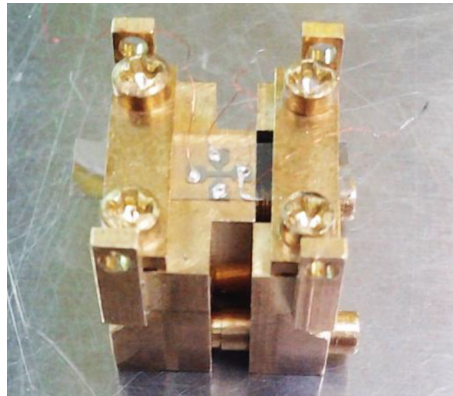
Figure 2.6: A small tensile jig made of brass

A small tensile jig with the size of $\sim 1.5 \times 1.5 \times 1.5$ cm^3, which was designed by the author following the advice of Prof. Takahiro Namazu and made by Sanwa Trading (Fig. 2.6), was used. Being small and free from ferromagnetic material, the jig is suitable for use under a high magnetic field, which is often narrow. Both ends of the strip sample were fixed with grippers. The grippers have tooth-like projections at the side touching to the sample in order to fix tightly. The differential mechanism enables small strain application, i.e. the jig consists of two parts connected by a screw that has part with different pitches (0.35 mm and 0.40 mm). With a rotation of the screw, two parts respectively move 0.35 and 0.40 mm against the screw, thus move 0.05 mm relatively to each others. With the sample length ~1 cm, the elongation of 0.05 mm corresponds to a strain $\varepsilon \sim 0.5\%$

The actual strain applied to the metal was calibrated using a microscope. A square metal pattern of $\sim 1 \times 1$ mm^2 on a PEN substrate was prepared and captured by a CCD camera

19

attached to the microscope [Fig. 2.7 (a)]. The lengths (l_x and l_y) of the edges of the square (~ 1 mm) corresponded to ~800 pixels. The length in the direction of the tensile strain applied is defined to be l_x. Value of the strain is derived from

$$\varepsilon_{x(y)} = \frac{l_{x(y)} - l^0_{x(y)}}{l^0_{x(y)}}, \tag{2.1}$$

where $l^0_{x(y)}$ is a reference length for the zero strain state. The strains obtained with multiple measurements are shown in Fig. 2.7. Though $l^0_{x(y)}$ should originally be measured at a state without strain, it was measured at 0.5 rotation of the screw after fixing the sample, because it was difficult to set the zero strain state manually. The result is that the strain is $\varepsilon_x = 0.60 \pm 0.04\%$ per rotation of the screw and Poisson's ratio of the PEN film is $\nu = -\varepsilon_y/\varepsilon_x = 0.43 \pm 0.07$, which is consistent with a previous work [55]. Judging from the strain value and scars on the substrate after the tensile testing, the tooth-like projections at farthest from the center work as grippers.
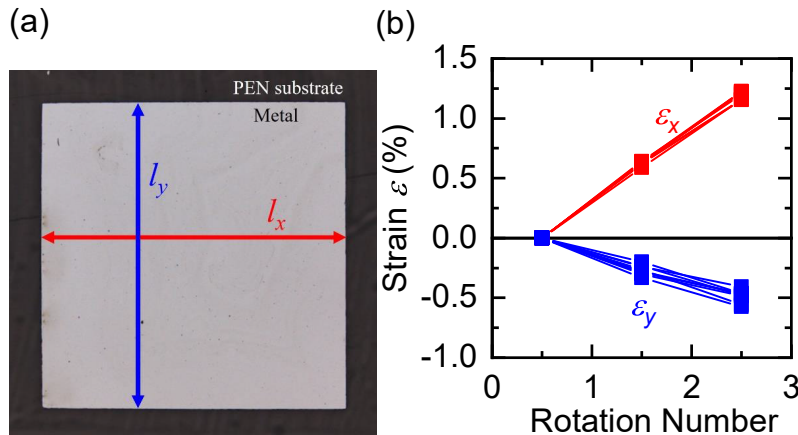
Figure 2.7: (a) An example of the microscope image used for the strain calibration. (b) Strain dependence on rotation number of the screw. ε_x and ε_y denote the strains in the tensile direction and that in the direction perpendicular to the tensile strain, respectively.

For the extended X-ray absorption fine structure (EXAFS) spectroscopy in Sec. 3.3, where a larger sample was required, a large tensile jig shown in Fig. 2.8 (a) was used. Main body of the jig was provided by Prof. Takahiro Namazu and attachments were made by the author. Figure 2.8 (b) shows the relationship between nominal strain and the strain actually

observed with the method mentioned above. The actual strain matches the nominal strain within the error bar.
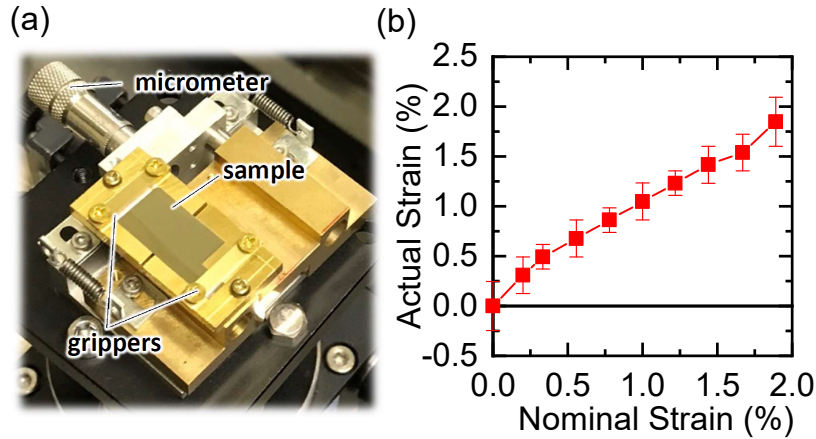
Figure 2.8: (a) A large tensile jig. The sample size is $\sim 1 \times 2$ cm^2. (b) A relation between the actual strain observed with a microscope and the nominal strain.

2.2.2 Automatic tensile machine

Figure 2.9 shows an automatic motor-driven tensile machine made by Wyseroad co.Ltd. The strip sample (Fig. 2.5 (b)) was fixed with the gap of 10 mm, where the fixed length was 11 mm with 0.5-mm-wide tooth-like projections. The gap was controlled by a screw connected to a stepper motor with microstep control. A pulse to the stepper motor changes the gap by ~ 0.1 μm, corresponding to 0.001% strain. The actual displacement was monitored by a linear encoder with 0.1 μm resolution. The load applied to the sample (F) is monitored by a load cell with 0.01 N resolution. The stress σ applied to the substrate is $\sigma = F/tw$ where t and w are the thickness and width of the substrate, respectively. The initial ($\varepsilon = 0$) state was set by reducing the gap from a state with a measurable tensile stress until the stress becomes zero.

The four Cu wires from the sample were connected to solder terminal blocks (Fig. 2.9 (b)), accordingly to a measuring instrument 2450 SourceMeter® (KEITHLEY). The 4-wire resistance mode, with a source current of 50-300 μA was used for the resistance measurement. For the measurement of magnetic tunnel junction samples in Chap. 5, the voltage source mode was used.
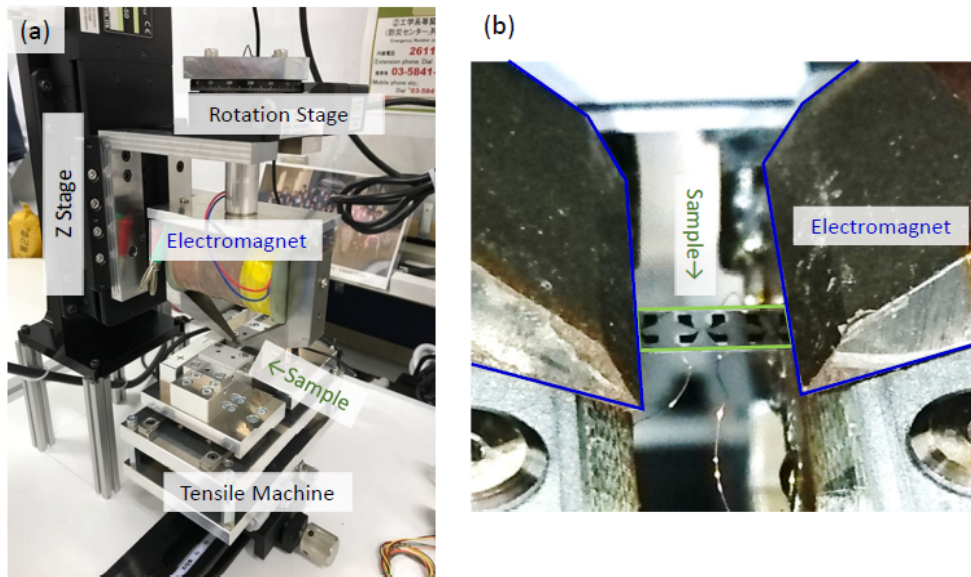
Figure 2.9: (a) An overview of the automatic motor-driven tensile machine and surroundings. (b) An enlarged view around the sample.

An in-plane magnetic filed was applied by an electromagnet above the sample. A current was applied to the coil with a bipolar power supply BP4610 (NF Corporation). The magnetic flux is lead to the sample via iron arms. Although the magnetic field is not uniform around the tip of the arms, the distance between the sample and the magnet was set by a highly reproducible Z stage [Fig. 2.9 (a)]. With a rotation stage, the magnetic field direction was controlled.

Chapter 3

Inverse magnetostriction effect on single magnetic layer

In this chapter, the inverse magnetostriction effect of samples with one magnetic layer is discussed. Section 3.1 shows a method for determining the effective magnetoelastic coupling constant B_{eff}. In Sec. 3.2, results for Co samples with various structure are discussed. In Sec. 3.3, the atomic distance change in magnetic Fe or Co layer is measured with the extended X-ray absorption structure spectroscopy.

3.1   Determination of effective magnetoelastic constant

The anisotropic magnetoresistance (AMR) effect was used to obtain the magnetic information from electric resistance. The AMR effect refer to the resistance R dependence on the angle between an electric current and magnetization direction (ϕ) as

$$R = R_0 + \Delta R \cos^2 \phi, \tag{3.1}$$

where R_0 is the resistance when $\phi = 90°$ and $\Delta R / R_0$ is the AMR ratio. This phenomenon is intuitively understood as following: the electron cloud distribution spread in the directions perpendicular to the magnetization (spin) direction because of the spin-orbit interaction, therefore the conductivity in the direction the electron cloud spread is better. In the sample

with in-plane magnetic anisotropy, which is the case for Co film thicker than 1 nm, ϕ correspond to the azimuthal angle of the magnetization.
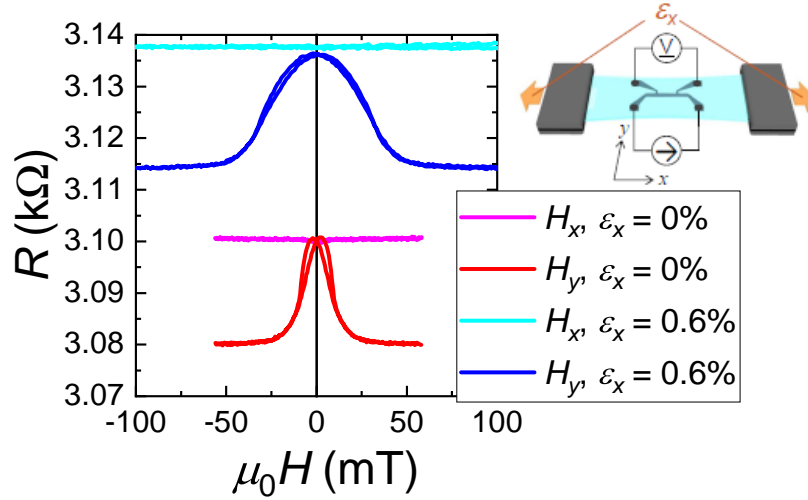
Figure 3.1: Example of the AMR curves with different field directions and strain values. The right upper inset shows the experimental configuration.

Figure 3.1 shows examples of the AMR curves of a Co sample with positive B_{eff} under different magnetic field directions (H_x, H_y) and strains ($\varepsilon_x = 0$, 0.6%). Note that a small strain is already applied for $\varepsilon_x = 0$% in order to avoid the multi-domain state. With the tensile strain in x direction and the positive B_{eff}, magnetic easy axis is in x direction. The AMR curves under H_x have negligible change because the magnetization directs $+x$ or $-x$ during the H_x sweeping. On the other hand under H_y, a clear resistance change is seen. When H_y is large, magnetization direct $\pm y$ obeying the field, and when H_y is small, magnetization direct $\pm x$ due to the magnetic anisotropy induced by the inverse magnetostriction effect. Thus, the saturation field roughly corresponds to the anisotropy field H_k. When the strain is increased ($\varepsilon_x = 0.6$%), H_k clearly increases. At the same time, R increases due to the strain. The resistance R of the metal depend on the size as

$$R = \rho \frac{l}{tw},\tag{3.2}$$

where ρ is the resistivity and l, t, w are length, thickness and width, respectively. The tensile strain in x direction increases l and decreases t and w with the Poisson's compression.

Figure 3.2 shows normalized hard axis magnetization curves. The R_0 and ΔR can be
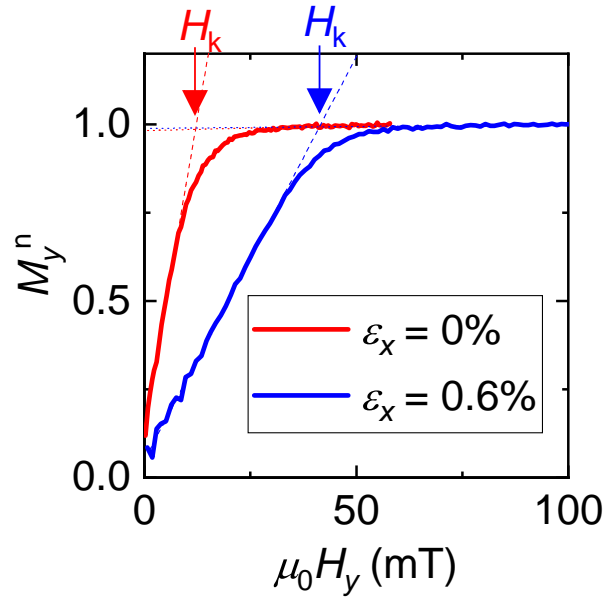
Figure 3.2: Normalized hard axis magnetization curves under different strain values.

respectively determined from the R when magnetization is saturated to the current direction (x) and the direction perpendicular to the current (y). Thus $\cos^2 \phi$ can be known from R under arbitrary magnetic field. Here, $\sin \theta$ is the y component of a normalized magnetization. The saturation field H_k is determined from the extrapolation of a linear fitting of the magnetization curve.

The magnetic anisotropy energy K_u is determined by

$$K_u = \frac{\mu_0 M_s H_k}{2}, \tag{3.3}$$

where μ_0 is the magnetic permeability of vacuum and M_s is the saturation magnetization. In this thesis, a literature data for bulk Co, $M_s = 1.79$ T [56] is used. The change in K_u per unit strain change corresponds to B_{eff}.

25

3.2 Magnetoelastic constant dependence on Co film structure

The effective magnetoelastic coupling constant B_{eff} of Co films with various structures is summarized in Fig. 3.3. The layer structures Ta(3.3 nm)/NMU(2.0 nm)/Co(t_{Co})/NMC(2.0 nm) from the substrate side were deposited on the PEN substrate. The NMU and NMC stand for under and capping non-magnetic layers (Cu or Pt), respectively. Thickness of the Co layer is denoted as t_{Co}.
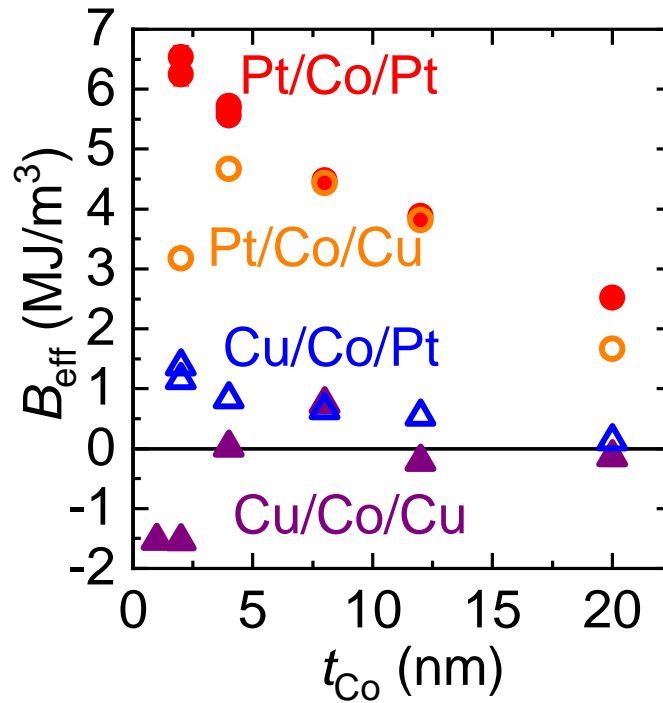
Figure 3.3: B_{eff} of Co films with various structures. NMB/Co/NMC shows the layer structure from the bottom side, omitting the Ta layer [e.g. Pt/Co/Pt means PEN/Ta(3.3 nm)/Pt(2.0 nm)/Co(t_{Co})/Pt(2.0 nm)]. The figure is taken from Ref. [57].

There are three features that can be extracted from Fig. 3.3.

1. The samples with Pt under layer have large B_{eff} compared to the Cu under layer samples.

2. In thin Co ($t_{Co} < 5$ nm), large differences in B_{eff} are seen depending on the capping layer material.

26

3. Absolute values of B_{eff} tend to be smaller for larger t_{Co}.

For the first feature, the under layer material dependence, crystalline structure is supposed to be important. Figures 3.4 (a) and (b) show the transmission electron microscope (TEM) images of Pt and Cu under layer samples, respectively. Although the TEM images show that
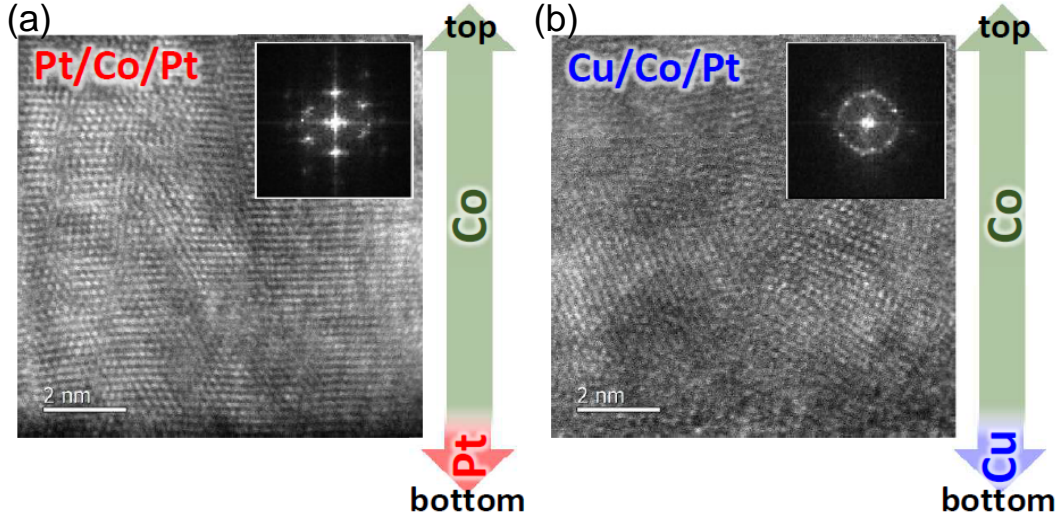
Figure 3.4: The TEM images of Co samples ($t_{\text{Co}} = 12$ nm) with (a) Pt and (b) Cu under layers. Insets show the FFT images of the TEM images. The figures are taken from Ref. [57].

the Co layers are polycrystalline in both cases, the two dimensional fast Fourier transform (FFT) reveals a difference. The Co layer on Cu has a random crystalline orientation, suggested by the ring-shaped FFT image. On the other hand in the Pt under layer case, the FFT shows clear spots indicating the face centered cubic (fcc) (111) texture. The crystalinity was also checked for other structures of the Co films on a thermally oxidized Si substrate using the X-ray diffraction (XRD) as shown in Fig. 3.5. It is confirmed that the Pt under layer samples show the large peak for fcc (111) of Co. An existence of the peak for fcc (111) of Pt suggests that the fcc (111) crystal orientation of the under layer is passed to the Co layers. Although data of the magnetoelastic constants in bulk fcc Co are absent, one can attribute the large B_{eff} to the fcc (111) textured structure because the similarly stacked hexagonal close packed (hcp) (0001) textured structure is calculated to have a large $B_{\text{eff}} = 11.3$ MJ/m^3 (see Appendix A.2 for details).

The second feature, the capping layer dependence, is similar to the surface or interface
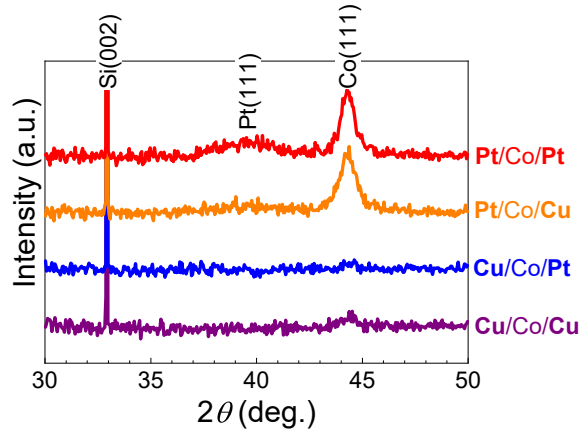
Figure 3.5: The XRD measurement of four types of Co samples ($t_{\text{Co}} = 20$ nm) on thermally oxidized Si substrates. The figure is taken from Ref. [57].

effect of the magnetoelastic effect [58, 59]. This phenomenon is expressed as

$$B_{\text{eff}} = B_{\text{bulk}} + \frac{B_{\text{surf}}}{t - t_0}, \tag{3.4}$$

where B_{bulk} is the magnetoelastic constant for bulk, B_{surf} is a coefficient for the surface or interface effect, t is the thickness of magnetic material and t_0 is a constant. This suggests that the interface or surface of the magnetic layer has different magnetoelastic property. In our Co case, Pt and Cu capping layers seem to have positive and negative interface magnetoelastic effects, respectively. Alloying of the interface or lattice strain due to the lattice mismatch are supposed to be the origins for the interface effect. The magnetoelastic effect may occur also in the magnetic moment induced to the non-magnetic material [60], which can contribute to the interface effect.

The third feature, the overall reduction of magnetoelastic effect in the thicker sample, is partially explained by degree of strain-transfer. This is further discussed in the next section by measurement of atomic distance. Other parts of the t_{Co} dependence can also be attributed to the difference in conditions of Co. For example, degradation of the crystalinity or change in lattice constant for thicker samples may explain such thickness dependence.

3.3 Strain in magnetic film

In this section, the atomic distance change in the magnetic layer with substrate stretching is measured using the extended X-ray absorption fine structure (EXAFS) spectroscopy.

3.3.1 Basics of EXAFS

An example of the EXAFS spectrum for a bulk Fe foil is shown in Fig. 3.6 (a). The axes μ and E are X-ray absorption coefficient and energy of the incident X-ray, respectively. The EXAFS refers to the oscillation at energy above the absorption edge in X-ray absorption spectrum. The X-ray with energy higher than the absorption edge excites photoelectrons, and the photoelectrons interact with the surrounding atoms [Fig. 3.6 (b)]. Therefore, the EXAFS
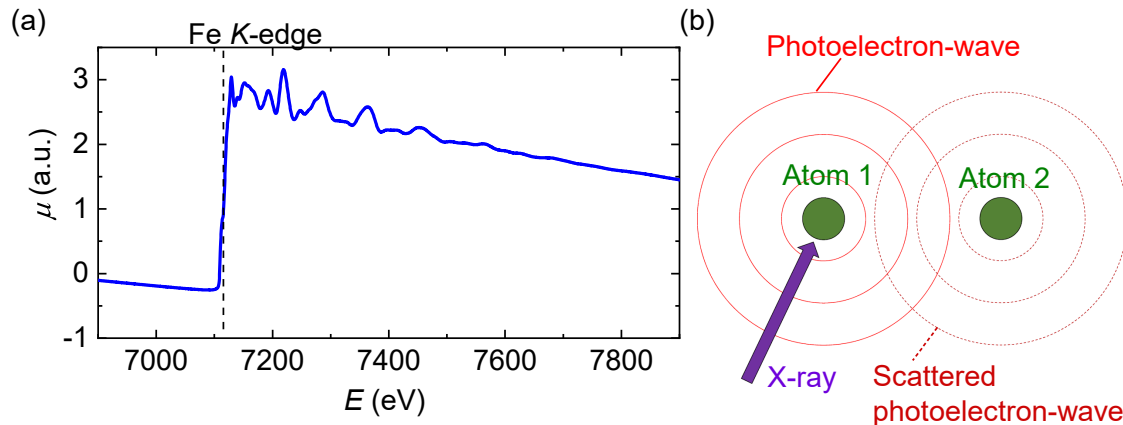
Figure 3.6: (a) The EXAFS spectrum of the Fe foil. μ and E are X-ray absorption coefficient and energy of the incident X-ray, respectively. (b) Schematics of the EXAFS. The incident X-ray excites photoelectron-wave from the atom 1 and the photoelectron-wave interacts with surrounding atoms, e.g. the atom 2.

oscillation reflects the structure around the atoms of the specific element of the absorption edge [61]. The EXAFS oscillation is often expressed in a form of the EXAFS modulation function $\chi(k)$,

$$\chi(k) = \frac{\mu - \mu_s}{\mu_0}, \tag{3.5}$$

where μ_s is a smooth component (background) of the absorption coefficient and μ_0 is the edge jump. A wave number of the photoelectron (k) is converted from E as

$$k = \sqrt{\frac{2m}{\hbar}(E - E_0)}, \tag{3.6}$$

where m, $\hbar$ and E_0 are the mass of electron, Dirac's constant and the absorption edge energy, respectively. Figure 3.7 shows the EXAFS spectrum in k space, converted from Fig. 3.6. In order to compensate the decay in the high k range, the spectrum is weighted with k^3. By
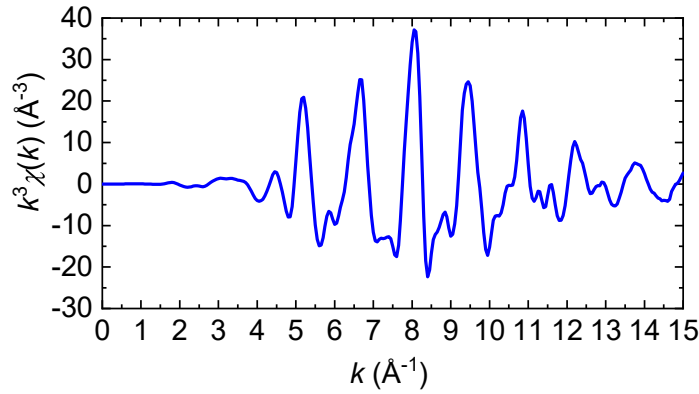
Figure 3.7: The EXAFS spectrum of the Fe foil in k space. $k^3\chi(k)$ is the EXAFS modulation function with k^3 weight.

the Fourier transform, a radial distribution function $\chi(R)$, whose peaks corresponding to the atomic bond distances, is obtained (Fig. 3.8). R is the radial coordinate. The first peak ($R \sim 2.2$ Å) and its shoulder ($R \sim 2.5$ Å) correspond respectively to the nearest and second nearest bonds of body center cubic (bcc) Fe. Fitting analysis is useful for determining the coordination number, atomic distance r and the Debye-Waller factor σ of each peak. In this thesis the fittings were performed in so-called q space, the inverse Fourier transform of $\chi(R)$ in a selected R range. The analysis, including the data conversion, the background elimination, Fourier transform, and fitting was performed with Demeter software [62]. Theoretical scattering phase shifts and amplitudes were calculated using a calculation code, FEFF 6 [63].
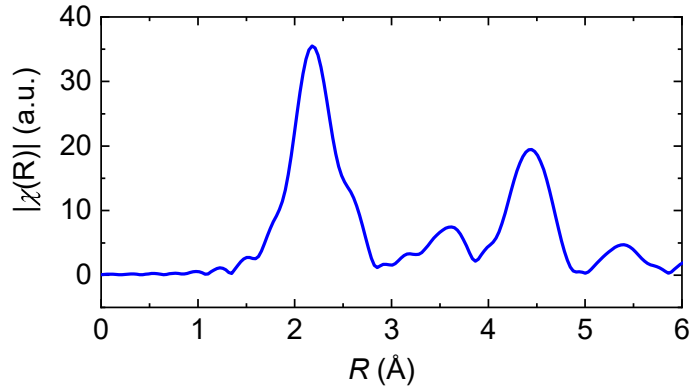
Figure 3.8: The EXAFS spectrum of the Fe foil in R space. $\chi(R)$ is the radial distribution function.

3.3.2 EXAFS measurement under strain

The EXAFS experiments were performed for Fe and Co samples deposited on a PEN substrate. The Fe sample is Ta(4.0 nm)/Fe(8.0 nm)/Pt(3.0 nm) and the Co sample is Ta(3.0 nm)/Pt(2.0 nm)/Co(7.0 nm)/Pt(2.0 nm) from the substrate side. The large tensile jig (Fig. 2.8) was used to apply the tensile strain ε_{FS} to the samples with the size of $\sim 1 \times 2$ cm^2. The EXAFS spectra were collected around the Fe (Co) K-edge [$\sim$7116 (7715) eV] at room temperature at beam line BL01B1 in SPring-8 [64]. The incident X-rays were monochromatized by a Si (111) double-crystal monochromator. The higher harmonics in the incident X-rays were removed by Rh-coated mirrors. The EXAFS spectra were measured in a fluorescence mode using a 19-element Ge solid state detector. In the EXAFS experiment, ε_{FS} was changed as 0% → 1.6% (→ 0.8% → 0.3%). Figure 3.9 shows two experimental configurations for different X-ray polarization. The electric field vector $\boldsymbol{E}$ of the incident X-ray is nearly parallel and perpendicular to the tensile strain ε_{FS} in ∥ and ⊥ configurations, respectively. The glancing angle of the incident X-ray was set to $\sim$4° in both configurations. The EXAFS spectra mainly reflects atomic structure in the polarization direction [65], i.e. the atomic distance in the tensile strain direction (the direction perpendicular to the film plane) can be investigated using ∥ (⊥) configuration.

Figure 3.10 shows EXAFS spectra in k space of the Fe sample at $\varepsilon_{FS} = 0$, 1.6% in ∥ and ⊥ configurations. The shape of the spectra is similar to that of a bulk polycrystalline
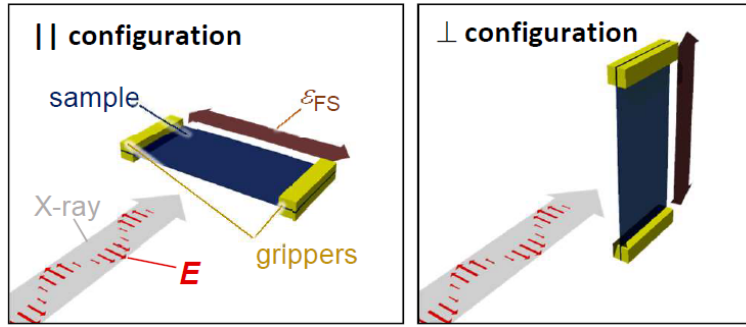
Figure 3.9: Schematics of ∥ and ⊥ configurations. The information of atomic bonds in the direction of an electric field E has a larger contribution.

Fe reference sample (Fig. 3.7), indicating that the obtained spectra are mainly attributed to Fe-Fe bonds. Importantly, in ∥ configuration, the spectrum is compressed slightly toward smaller k and the amplitude is lowered by the strain application. These results suggest the atomic distance elongation and increase of disorder. On the other hand, almost no change can be seen in ⊥ configuration. Although it is difficult to see corresponding peak shifts in the Fourier transforms in Fig. 3.11, fitting analysis reveals an significant effect of ε_{FS} application as shown in Fig 3.12. Four parameters of atomic distances for the nearest neighbor r_{Fe_NN}, the second nearest neighbor r_{Fe_SN} and the Debye-Waller factors for the nearest and second nearest neighbors were used for the fitting. The coordination numbers were set to be constant independent of ε_{FS}. Data in 1.7 Å < R < 2.9 Å were used to perform the fitting in q space. Significant increase beyond the error bar is confirmed in r_{Fe_NN} and r_{Fe_SN} as increasing ε_{FS}. In addition to the increase in the atomic distances, increase in the Debye-Waller factors suggesting the change in structural disorder is also seen (not shown). The amplitude lowering in the spectra is supposed to be caused by an anisotropic atomic distance change due to the uniaxial strain application. On the other hand in ⊥ configuration, almost no atomic distance change is seen.

Similar results are obtained for the Co sample as shown in Fig 3.13. The peak at $R \sim 2.2$ Å was fitted assuming the nearest neighbor of fcc Co, with its atomic distance r_{Co_NN} and the Debye-Waller factor being the parameters. The fitting was performed using data in 1.7 Å < R < 2.5 Å.

So far, atomic distance are mainly discussed. From here atomic strain, i.e. change ratio

Figure 3.10: EXAFS spectra in k space of the Fe sample at $\varepsilon_{FS} = 0$, 1.6% in $\parallel$ and $\perp$ configurations.
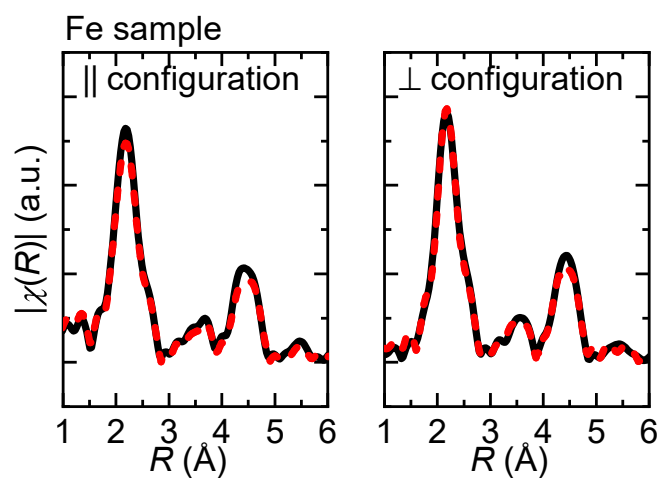
Figure 3.11: Radial distribution functions of the Fe sample at $\varepsilon_{FS} = 0$, 1.6% in $\parallel$ and $\perp$ configurations.
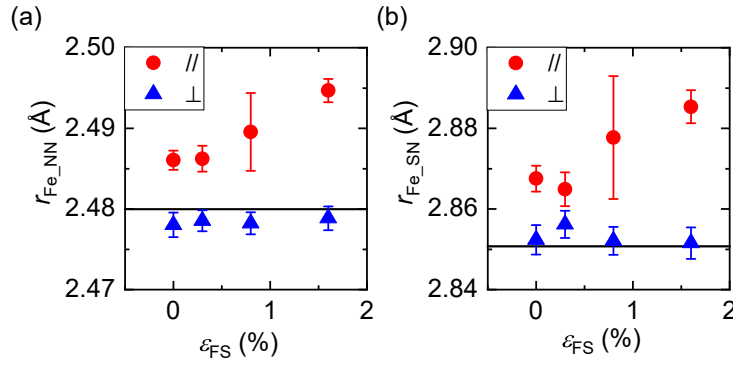
Figure 3.12: Dependence on ε_{FS} of fitting parameters, atomic distances for (a) the nearest neighbor r_{Fe_NN} and (b) the second nearest neighbor r_{Fe_SN}.

of atomic distance $[r(\varepsilon_{FS} = 1.6\%) - r(\varepsilon_{FS} = 0\%)]/r(\varepsilon_{FS} = 0\%)$, is discussed. The atomic strains for the Fe sample calculated from Fig. 3.12 are summarized at the row of "EXAFS fitting results" in Tab. 3.1. The atomic strains for the Co sample calculated from Fig. 3.13 (c) is also summarized at the row of "EXAFS fitting results" in Tab. 3.2. We note that the atomic

Path_Configuration	NN_$\parallel$	NN_$\perp$	SN_$\parallel$	SN_$\perp$
EXAFS fitting results	+0.35±0.11%	-0.03±0.12%	+0.62±0.25%	-0.03±0.27%
Calculation for bcc (110)	+0.82%	-0.13%	+0.69%	+0.04%
Calculation for bcc (100)	+0.56%	+0.21%	+1.08%	-0.48%

Table 3.1: Atomic strains of experimental results for the Fe sample and of calculations at $\varepsilon_{FS} = 1.6\%$ with 100% strain-transfer. NN and SN stand for the nearest neighbor and second nearest neighbor paths, respectively.

Path_Configuration	NN_$\parallel$	NN_$\perp$
EXAFS fitting results	+0.26±0.14%	0.00±0.11%
Calculation for fcc (111)	+0.82%	-0.13%

Table 3.2: Atomic strains of experimental results for the Co sample and calculations at $\varepsilon_{FS} = 1.6\%$ with 100% strain-transfer. NN stands for the nearest neighbor path.

strains for $r_{Fe(Co)\_NN}$ and r_{Fe_SN} obtained in $\parallel$ configuration (+0.3-0.6%) are pretty smaller than $\varepsilon_{FS} = 1.6\%$. In addition, the reduction in $r_{Fe(Co)\_NN}$ and r_{Fe_SN} for $\perp$ configuration is also smaller than a prediction from the Poisson compression ($\sim$ -0.5%, assuming the Poisson's ratio of $\nu = 0.3$). However, these results do not necessarily suggest that the strain in the flexible substrate fails to be transferred to the Fe or Co layers. In order to discuss quantitatively the degree of the strain-transfer, the ideal value, i.e. the ratio of the change in the atomic distance
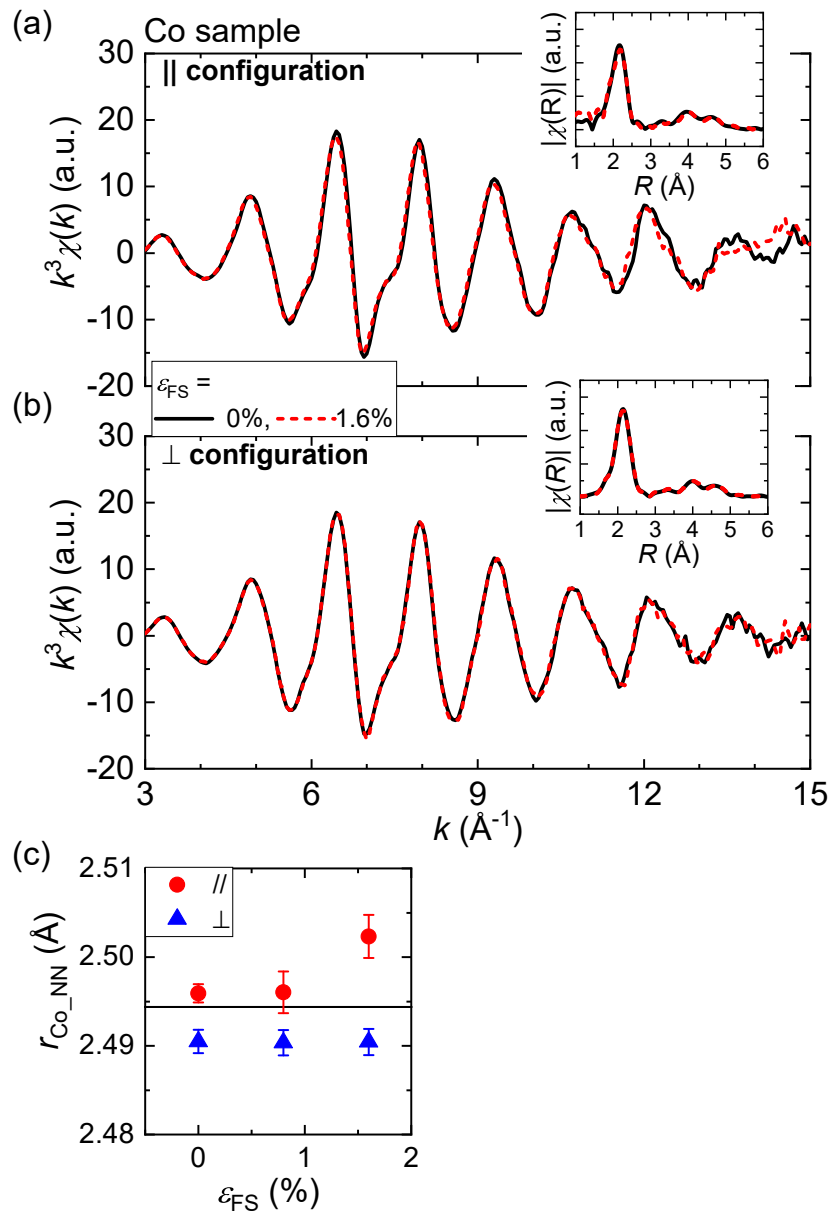
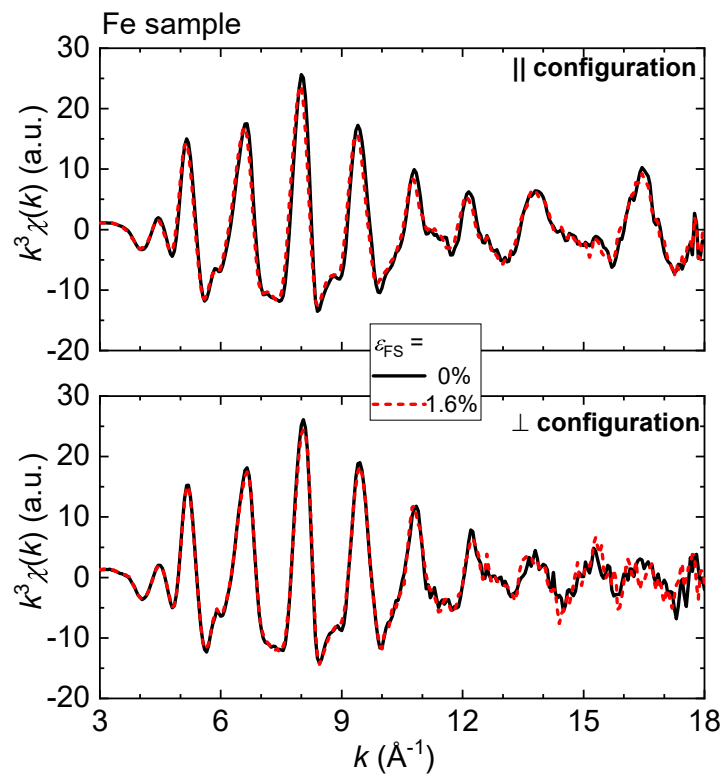Figure 3.13: EXAFS spectra in k space of the Co sample at $\varepsilon_{FS} = 0$, 1.6% in (a) $\parallel$ and (b) $\perp$ configurations. Insets show radial distribution functions. (c) Dependence on ε_{FS} of atomic distance for the nearest neighbor r_{Co_NN}.

for the 100% strain-transfer case is needed. The rows of "Calculation" in Tabs. 3.1 and 3.2 are results of the calculation considering the Poisson's compression, crystalline orientations of the ferromagnetic metals, and polarization of the X-ray (see Appendix B for the detail of the calculation). The atomic distance changes are shown with respect to different crystalline textures. These calculation values also appear to be smaller than 1.6%. The essence is that the change in distance of oblique atomic bonds, whose angle with the strain direction or X-ray polarization direction is non-zero, is relatively small.

The crystalline structure of the Fe layer is supposed to be a weak bcc (110) texture, because a corresponding XRD peak is obtained for an Fe sample on a thermally oxidized Si substrate while it is not seen on the Fe sample on a PEN substrate. However it seems difficult to explain the experimental results for the Fe sample with the calculation only assuming bcc(110) texture, and the relatively large r_{Fe_SN} change compared with the $r_{Fe(Co)\_NN}$ change in $\parallel$ configuration is rather qualitatively reproduced by the calculation for bcc (100) texture. On the other hand in $\perp$ configuration, calculation for bcc (110) texture shows better matching with the experiment. Therefore, the Fe layer is expected to have a mixed structure of bcc (110) and (100) textures. As a result, the above calculation suggests that at least about 60% of ε_{FS} is transferred to the Fe layer, although the crystalline structure is unclear in the present sample. Note that the difference of the atomic strains between the nearest and the second nearest neighbor atoms never appears when a polycrystal with perfectly random orientation is assumed.

Next, the atomic strain for the Co sample is briefly discussed. Although the Co sample includes hcp (0001) structure [Fig. 3.4 (a)], calculation was performed using fcc (111) texture as shown in Tab. 3.2, because the nearest neighbor paths in hcp and fcc are almost the same. As a result, the strain transferred to the Co layer is estimated to be about 30% of that in the substrate. The difference of the strain-transfer ratio between the Fe and Co samples may arise from the under layers. For example, existence of the additional Pt under layer in the Co sample may introduce a larger strain relaxation. It will be important to compare samples with various layer structures, in order to identify determinants of the strain-transfer. Since B_{eff} is derived using ε_{FS} in Sec. 3.2, actual magnetoelastic constants of the Co layers are three times larger, which means B_{eff} can be tripled if a perfect strain-transfer is realized.

3.3.3 Thickness dependence of Co sample

The EXAFS measurements were also performed for Co samples Ta(2.9 nm)/Pt(t_{Pt})/Co(t_{Co})/ Pt(1.6 nm) from the substrate side, with different Co thickness t_{Co} and under layer Pt thickness t_{Pt}. The EXAFS spectra were obtained only in ∥ configuration for ε_{FS} = 0 and 1.6%. Figures 3.14 (a) and (b) show t_{Co} dependence of r_{Co_NN} of the Co samples with t_{Pt} = 1.6 nm and corresponding atomic strains, respectively. The right axis of Fig. 3.14 (b) is the ratio of strain-transfer assuming that the atomic strain of 0.82% is the perfect strain-transfer value as calculated above. A tendency of the atomic strain reduction with increased t_{Co} is seen, which is though within the error bars. This suggest that the B_{eff} decrease in Fig. 3.3 is related to the decrease of strain-transfer. The measurements were also performed for various bottom
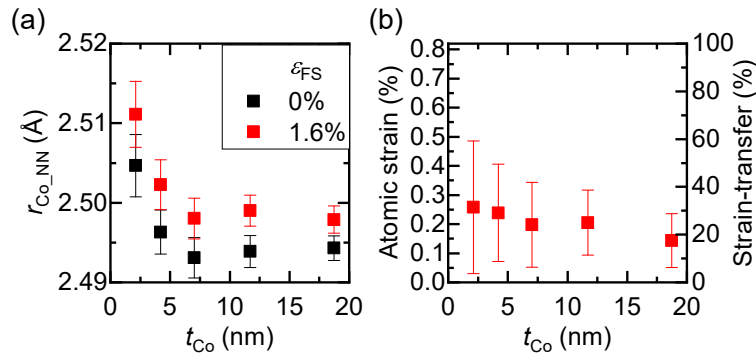
Figure 3.14: (a) Co thickness t_{Co} dependence of r_{Co_NN} of Co samples with t_{Pt} = 1.6 nm at ε_{FS} = 0, 1.6%. (b) Corresponding atomic strains and ratio of the strain-transfer.

Pt thickness. Figures 3.15 (a) and (b) show t_{Pt} dependence of r_{Co_NN} of the Co samples with t_{Co} = 11.7 nm and the corresponding atomic strains, respectively. Cu under layer is used for the case of t_{Pt} = 0 nm. A slight increase tendency of atomic strain with t_{Pt} increase can be seen. The Cu insertion is particularly responsible for the smaller strain-transfer. This suggest that the B_{eff} dependence on the under layer material species is attributed to the difference in the strain-transfer as well as the crystalline orientation.

Figures 3.16 (a) and (b) show B_{eff} dependence on t_{Co} and t_{Pt} for the same samples used for the EXAFS measurements. Figure 3.16 (a) shows a stronger t_{Co} dependence compared with Fig. 3.3. This difference may be attributed to the slight difference in the layer structure (e.g. thinner Pt layers). By comparing these thickness dependence of B_{eff} with that of the atomic
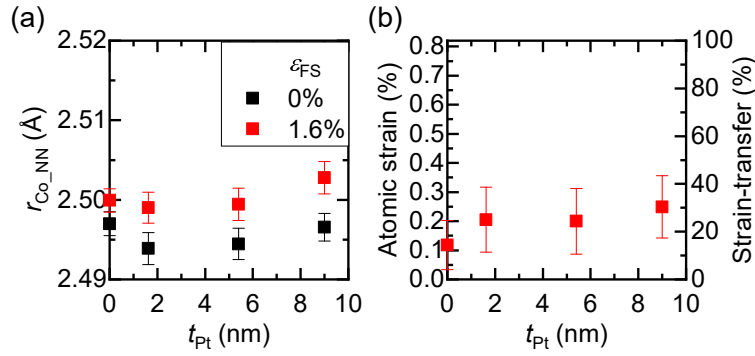
Figure 3.15: (a) Bottom Pt thickness t_{Pt} dependence of r_{Co_NN} of Co samples with $t_{Co} = 11.7$ nm at $\varepsilon_{FS} = 0, 1.6\%$. (b) Corresponding atomic strains and ratio of the strain-transfer. $t_{Pt} = 0$ nm denotes that 2.0 nm Cu layer is used instead of the Pt under layer.

strains (Figs. 3.14 and 3.15), it is concluded that only a limited part of the B_{eff} dependence on thickness is attributed to the strain-transfer decrease.

Figures 3.17 (a) and (b) show the Debye-Waller factor of nearest neighbor bonds of Co (σ_{Co_NN}) dependence on t_{Co} and t_{Pt}, respectively. As the measurement temperature is the same, σ_{Co_NN} is affected by the static structural fluctuation. The clear t_{Co} dependence reflects different Co conditions at the Pt/Co interfaces, which can be induced by the lattice misfit. This reinforces that the interface effect (Eq. 3.4) is seen in the range ($t_{Co} < 5$ nm) as discussed in the previous section. On the other hand, the B_{eff}-t_{Co} relation at a thicker range is not explained by the σ_{Co_NN}-t_{Co} relation. Therefore, the bulk state of the Co layer is supposed to be dependent on t_{Co}.
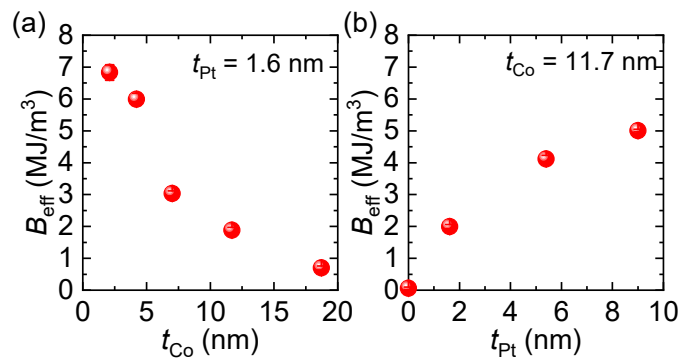
Figure 3.16: The effective magnetoelastic constant B_{eff} dependence on (a) Co thickness t_{Co} and (b) bottom Pt thickness t_{Pt} of Co samples. $t_{Pt} = 0$ nm denotes that 2.0 nm Cu layer is used instead of the Pt under layer.
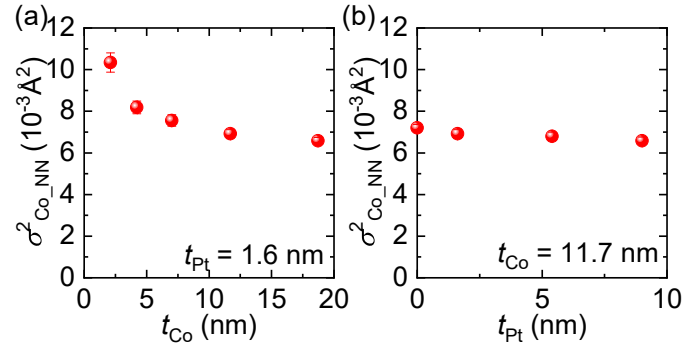
Figure 3.17: The Debye-Waller factor of nearest neighbor bonds of Co (σ_{Co_NN}) dependence on (a) Co thickness t_{Co} and (b) bottom Pt thickness t_{Pt} of the Co samples. $t_{Pt} = 0$ nm denotes that 2.0 nm Cu layer is used instead of the Pt under layer.
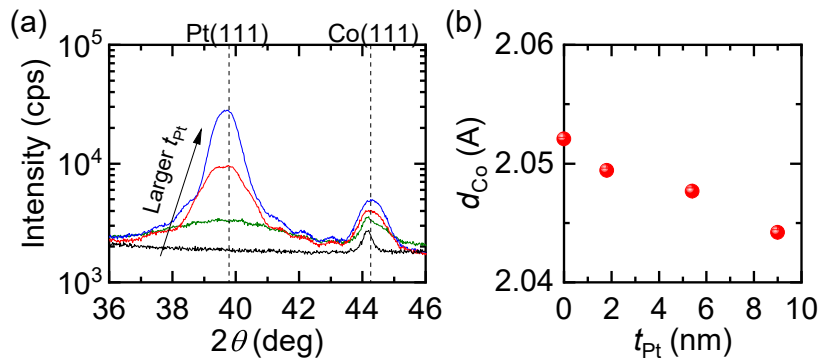
Figure 3.18: (a) XRD spectra for the Co samples on a PEN substrate with different t_{Pt} and fixed $t_{Co} = 11.7$ nm. (b) A dependence of lattice spacing of Co (d_{Co}) on t_{Pt}. $t_{Pt} = 0$ nm denotes that 2.0 nm Cu layer is used instead of the Pt under layer. The peaks were fitted using the split-type pseudo-Voigt function in Rigaku PDXL2.

For the t_{Pt} dependence, the slight σ_{Co_NN}-t_{Pt} relation may reflect Co crystalinity enhancement with the thicker Pt under layer, which is also confirmed by peak heights in XRD measurements [Fig. 3.18 (a)]. It is suggested that a thicker Pt under layer leads to the better fcc (111) crystalline orientation of the Pt and Co layers, and accordingly the larger B_{eff}. At the same time, the out-of-plane lattice distance of Co (d_{Co}) is obtained from the peak of Co (111) as shown in Fig. 3.18 (b). The thicker Pt under layer seems to reduce d_{Co} by enhancing in-plane lattice constant which is also seen in Fig. 3.15 (a). This in-plane lattice strain may be the origin of the B_{eff}-t_{Pt} relation, as a theoretical study insists that a larger lattice constant of Pt/Co system enhances magnetoelastic constants [66]. The B_{eff}-t_{Co} dependence can be also attributed the lattice constant change of Co since the lattice of a thinner Co layer is strongly affected by the Pt under layer, which is seen in Fig. 3.14 (a).

3.4   Summary of this chapter

In this chapter, the inverse magnetostriction effect of Co thin films on a flexible PEN substrate has been studied. The effective magnetoelastic coupling constant B_{eff} largely depends on the layer structure. With a Pt under layer, the Co layer has fcc (111) texture, which leads to a relatively large positive B_{eff}. On the other hand with a Cu under layer, the Co layer shows a randomly oriented polycrystalline structure, resulting in an either positive or negative B_{eff} with a small absolute value. Pt and Cu capping layers add the interface magnetoelastic effect. B_{eff} of the thin Co layer (with the thickness smaller than 5 nm) deviates to positive and negative directions when the Co layer is capped by Pt and Cu layers, respectively. Furthermore, the larger Co thickness tends to reduce the absolute value of B_{eff}.

The EXAFS spectroscopy shows that a part of the B_{eff} dependence on the Co thickness is attributed to the reduction of the strain-transfer from the substrate to the Co layer. A large part of the origin of the Co thickness dependence, however, remains to be unclear, which rather means that the magnetoelastic property truly depends on the Co thickness through the differences in crystalinity or lattice constant. The EXAFS also shows that the strain-transfer is not perfect (30-60% depending on sample structures), suggesting that B_{eff} can be further increased by somehow enhancing the strain-transfer.

These findings advance comprehensive understanding of the inverse magnetostriction effect in thin films, where previous studies have reported sample-by-sample results [36–43, 51–54] . Such a control of the inverse magnetostriction effect will be useful for developing flexible spintronic devices proposed in the following chapters.

Chapter 4

Strain sensor with giant magnetoresistance effect

In this chapter, the inverse magnetostriction effect is combined with the giant magnetoresistance (GMR) effect. Section 4.1 briefly introduces the GMR effect. In Sec. 4.2, changes in the magnetoresistance curves with strain application to flexible GMR samples are discussed. In Sec. 4.3, the strain sensing characteristics of the GMR samples or are discussed.

4.1   Giant magnetoresistance effect

The GMR effect is firstly found in multilayer structures of ferromagnetic and non-magnetic layers [1]. The magnetoresistance (MR) ratio reaches tens of % with the multilayer structures with tens of repeated ferromagnetic and non-magnetic layers, where the MR ratio is usually defined as $\Delta R/R_\mathrm{P}$, with the resistance change ΔR and the resistance when magnetization directions of the ferromagnetic layers align parallel to each others (R_P). The GMR effect also occurs in a tri-layer structure where a non-magnetic layer is sandwiched by two ferromagnetic layers [2]. The resistance R depends on the relative angle α of the two ferromagnetic layers as

$$R = R_\mathrm{P} + R_\mathrm{AP}\frac{1 - \cos\alpha}{2}, \tag{4.1}$$

where R_AP is the resistance when magnetization directions of the ferromagnetic layers align anti-parallel to each others [67].

The origin of the GMR effect is mainly explained by the spin-dependent scattering [1,68], i.e. up-spin and down-spin electron flows have different resistance and contribute as parallel circuit. The spin-dependent scattering occurs in ferromagnetic transition metals because the d bands are spin-split due to the exchange interaction. Suppose that an up(down)-spin electron feels resistance of $R_\uparrow$ when conducting through a ferromagnetic layer with up(down)-magnetization, an up(down)-spin electron feels resistance of $R_\downarrow$ when conducting through a ferromagnetic layer with down(up)-magnetization. For simplicity, spin-flip scattering is ignored. The tri-layer structure accordingly has resistances of $R_P = 2R_\uparrow R_\downarrow/(R_\uparrow + R_\downarrow)$ and $R_{AP} = (R_\uparrow + R_\downarrow)/2$ for parallel and antiparallel magnetization configuration, respectively. Here $R_{AP} > R_P$, if $R_{AP} \neq R_P$, $R_P > 0$, $R_{AP} > 0$ can be easily confirmed.

Some tips are often needed to obtain a good MR curve, in other words, to make α change largely during a magnetization sweeping. The inter layer exchange coupling tries to align the magnetization directions either parallel or anti-parallel, depending on the non-magnetic spacer layer thickness [69]. The spacer thickness of ~1 nm often shows the anti-parallel coupling, which is useful to obtain the GMR effect since α becomes $0°$ when a large magnetic field is applied and α becomes $180°$ when the magnetic field becomes small. Another frequently used technique is the exchange bias, i.e. the internal magnetic field applied to a ferromagnetic material from a proximity antiferromagnetic material [70]. The magnetization of one of the magnetic layers is fixed by the exchange bias while the magnetization of the other magnetic layer can be changed freely by an external magnetic field [67]. Such a device is called spin-valve, since an electric current is controlled by its magnetic (spin) property. Even in the case without the exchange bias or the anti-parallel inter layer exchange coupling, the GMR effect can be observed if a difference in coercivities of the two ferromagnetic layers is made, by using different material, thickness or so on for the ferromagnetic layers. These are called pseudo spin-valves.

In this thesis, we apply a strain to the (pseudo) spin valves. The inverse magnetostriction effect changes α, resulting in a resistance change through the GMR effect. As a matter of fact, however, a number of researchers reported the idea of combining the inverse magnetostriction effect with the GMR effect [71–81]. Most of them showed that the MR curves changes as a strain is induced (Fig. 4.1), insisting that the devices can be used as strain sensors. However,
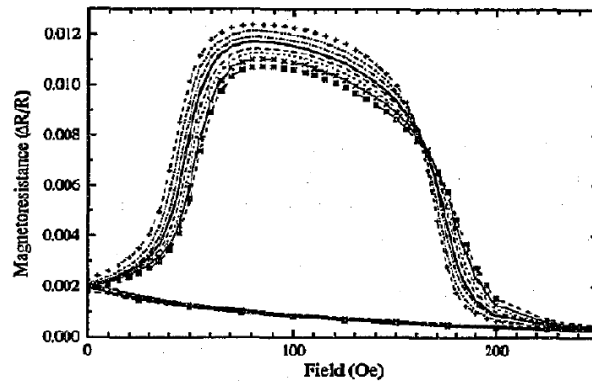
Figure 4.1: Magnetoresistance curves of a polyimide/(Fe 4 nm)/(Cu 5 nm)/(Co 4 nm)/(Cu 5 nm) sample with different compressive strains of -0.03---0.16%. The figure is taken from the first report for combining the magnetoresistance and inverse magnetostriction effects [71].

the MR curve change has been subtle and the strain sensing property has not actually been checked in many cases. The use of a rigid substrate or a poorly designed magnetic property is supposed to cause the subtle strain effects. Here we use flexible substrates enabling a large strain application and design the magnetoelastic property of our (pseudo) spin valves to realize a strain direction sensing, which takes an advantage of magnetism.

4.2 Strain effect on magnetoresistance curve

4.2.1 Basic strain effect

Firstly, the basic inverse magnetostriction effect on our GMR device is schematically explained. Figure 4.2 shows the results of the strain application to a sample of PEN/Ta(2.5 nm)/Pt(1.5 nm)/Co(3.5 nm)/Cu(5.0 nm)/Co(4.1 nm)/Cu(2.5 nm)/Pt(0.3 nm) (hereinafter, referred to as the basic sample). A tensile strain ε_x, whose direction is defined to be x, was applied using the motor-driven tensile machine (Fig. 2.9). The GMR effect was measured in the current-in-plane configuration using the four-terminal method with a direct current in the x direction. The magnetoresistance (MR) curves were measured under external magnetic fields parallel (H_x) and perpendicular (H_y) to ε_x, which is shown in Figs. 4.2 (b) and (c), respectively. The MR ratio (MRR) is defined as $(R - R_\mathrm{P})/R_\mathrm{P}$, where R is the four-wire resis-
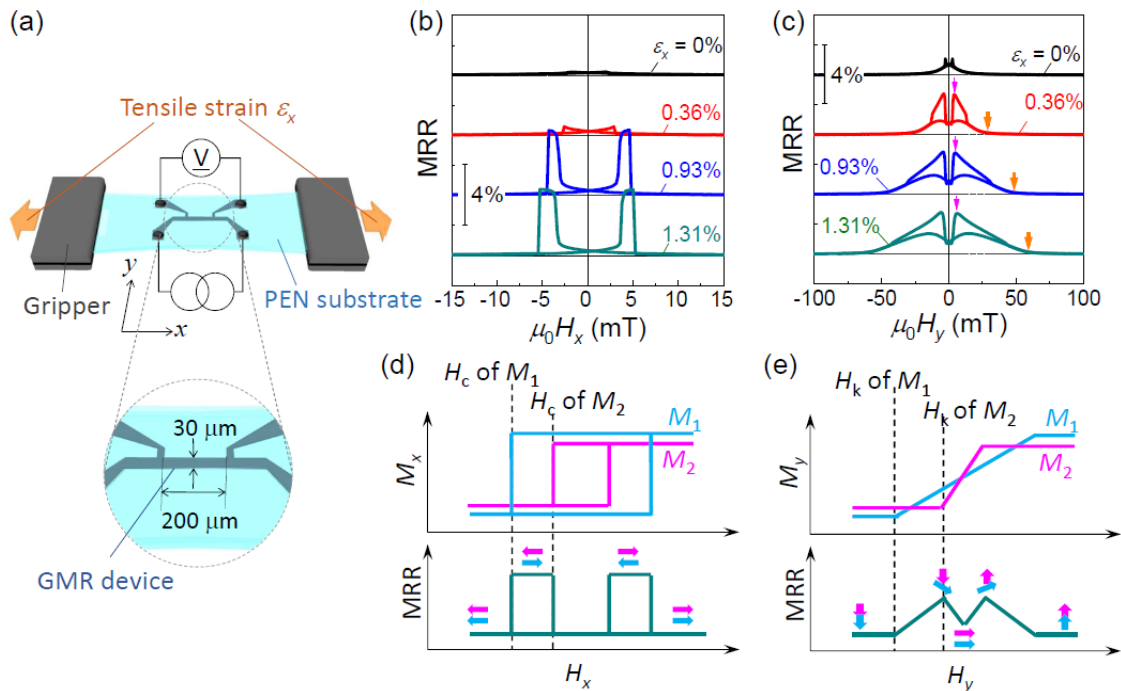
Figure 4.2: (a) Experimental configuration and the devise size. Magnetoresistance curves with different strains ε_x under external magnetic fields (b) parallel and (c) perpendicular to the tensile strain direction. Each curve has an offset in the magnetoresistance ratio (MRR). Schematics of magnetization curves and corresponding MR curves under magnetic fields (d) parallel and (e) perpendicular to the tensile strain direction. The figures are taken from Ref. [57].

45

tance and R_P is the R value at a sufficiently high magnetic field, where the magnetizations of the Co layers are in the parallel configuration.

At $\varepsilon_x = 0\%$, almost no change in the resistance is observed under the H_x sweeping, probably because the magnetizations switch simultaneously in the two Co layers, and thus an antiparallel magnetization configuration is not realized. In contrast, typical GMR curves are observed at $\varepsilon_x \geq 0.93\%$. A schematics for the typical GMR curve and its underlying magnetization curves of the two magnetic layers (M_1, M_2) are shown in Fig. 4.2 (d). Coercivities H_c of M_1 and M_2 correspond to the fields where abrupt changes appear in the MR curve. Therefore, it is supposed that the typical GMR curves are observed under the strains because the coercivity difference increases due to a difference in the positive magnetoelastic constants B_{eff} of the Co layers.

When a magnetic field is applied perpendicular to ε_x, the MR curves develop into a different shape, as shown in Fig. 4.2 (c). At $\varepsilon_x = 0\%$, only a small MR effect, which is mainly due to the anisotropic MR (AMR) effect, is seen. In contrast, a relatively large MR effect is observed under the larger ε_x. Schematics for such a GMR curve and its underlying magnetization curves of two magnetic layers (M_1, M_2) are shown in Fig. 4.2 (e). Assuming hard axis magnetization curves for M_1 and M_2, one can suppose that the fields for the peak and saturation correspond to the anisotropy fields H_k of M_1 and M_2, respectively. This is discussed in detail at Sec. 4.2.4.

4.2.2 Contribution of AMR

Based only on the GMR effect, the resistance under zero and high magnetic fields in y direction should be the same in Fig. 4.2 (e), since M_1 and M_2 align parallel in both states. Therefore, the difference in the resistance between the two states are attributed to the AMR effect of the two Co layers. Figure 4.3 shows MR curves under different ε_x of the basic sample, where the vertical axis ΔR is a resistance difference from the resistance at zero field instead of MRR. At $\varepsilon_x = 0\%$, the resistance under a large H_y is smaller than that under a large H_y, which is consistent with the AMR effect. Judging from the negligible MR effect under H_x, the magnetic easy axis is in the x direction even at the initial state ($\varepsilon_x = 0\%$). At $\varepsilon_x = 1.31\%$, the AMR ratio, the resistance difference between under large H_x and H_y, is
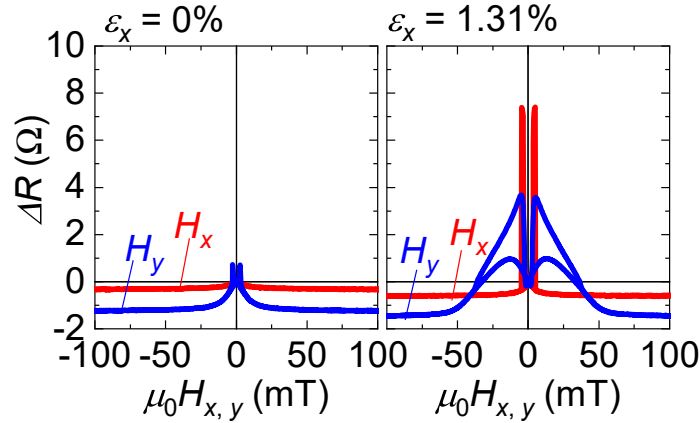
Figure 4.3: Magnetoresistance curves under magnetic fields in *x* and *y* directions with strains $\varepsilon_x = 0, 1.31\%$. The vertical axis ΔR is a resistance difference from the resistance at zero field. The figures are taken from Ref. [57].

almost the same for that at $\varepsilon_x = 0\%$. The resistance at $H_x = 0$ mT is, however, slight larger than that at a high H_x, indicating that the magnetization slightly deviates from the single domain state under zero magnetic field. Because simulations in Sec. 4.2.4 assume the single domain state, this deviation is not preferred in the viewpoint of analysis.

4.2.3   Interlayer exchange coupling
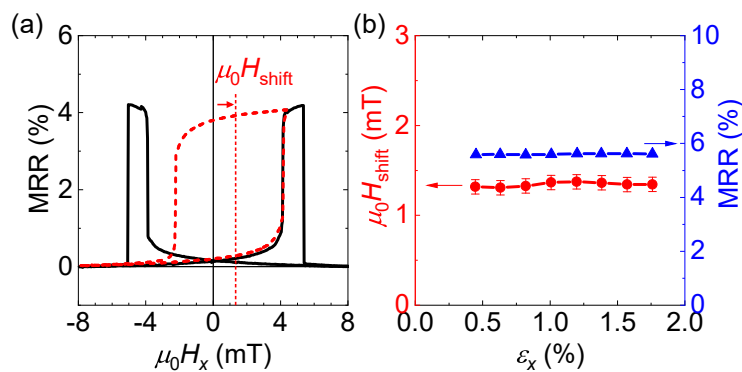
Figure 4.4: (a) Major and minor magnetoresistance loops of the basic sample. (b) Strain ε_x dependence of the shifting field H_{shift} and the magnetoresistance ratio (MRR) of a sample in Sec. 4.2.6. The figures are taken from Ref. [57].

Figure 4.4 (a) shows MR curves including the minor curve (red dashed line) of the basic

sample. The minor curve apparently shifts toward positive H_x, indicating a presence of a ferromagnetic interlayer exchange coupling. The origin of the coupling can be either the carrier-mediated interlayer exchange coupling [69] or the Néel's orange peel coupling [82]. The latter contributes to the ferromagnetic interlayer coupling due to the magnetostatic coupling caused by the interface roughness. Although crystallinity and a line profile of elements distribution of the flexible GMR film [Fig. 4.5 (d)] are similar to those of the GMR film deposited on a thermally oxidized Si substrate [Fig. 4.5 (c)], wavy interfaces due to the roughness of the PEN substrate are apparently seen in Fig. 4.5 (b), which is supposed to enhance the Néel's orange peel coupling.
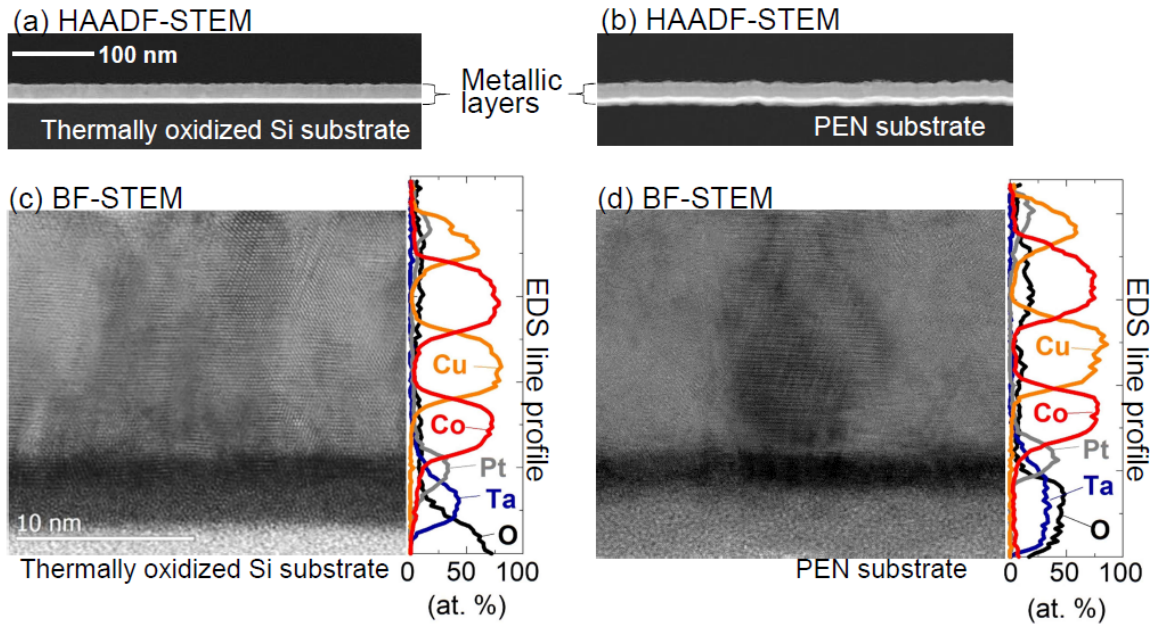
Figure 4.5: Transmission electron microscope (TEM) analysis of the basic sample deposited on different substrates. High angle annular dark field scanning TEM (HAADF-STEM) images in a wide range for the samples on (a) thermally oxidized Si and (b) PEN substrates. Bright field scanning TEM (BF-STEM) images and energy dispersive X-ray spectroscopy (EDS) line profiles for the sample on (a) thermally oxidized Si and (b) PEN substrates. The figures are taken from Ref. [57].

In the simulation in the following section, however, this inter layer exchange coupling is ignored. It was also checked that the shift of the minor loop ($\mu_0 H_{\text{shift}}$) and the MRR are invariant with ε_x, where another sample in Sec. 4.2.6 was used because the ε_x range where the minor loop can be observed is narrow for the basic sample.

4.2.4 Simulation

Here, numerical simulation of the MR curves in Fig. 4.2 (c) using the coherent magnetization rotation model, or the Stoner-Wohlfarth model, is discussed. The model assumes the energy densities E_1 and E_2 of the two ferromagnetic layers 1 and 2 respectively, to be

$$\frac{E_{1(2)}}{M_{s1(2)}} = -\frac{\mu_0 H_{k1(2)}}{2} \cos^2 \phi_{1(2)} - \mu_0 H \cos(\phi_H - \phi_{1(2)}). \tag{4.2}$$

$M_{s1(2)}$ and $\phi_{1(2)}$ are the saturation magnetization and magnetization direction angle of the ferromagnetic layer 1(2). The first and second terms represent the uniaxial magnetic anisotropy and magnetostatic energy, respectively. $H_{k1(2)}$ is the anisotropy field of the ferromagnetic layer 1(2), where positive and negative $H_{k1(2)}$ indicate that $\phi_{1(2)} = 0°$ and $\phi_{1(2)} = 90°$ are the easy axis directions, respectively. H and ϕ_H are the magnitude and direction of the external magnetic field respectively. Figure 4.6 (a) shows the configuration for the model. According
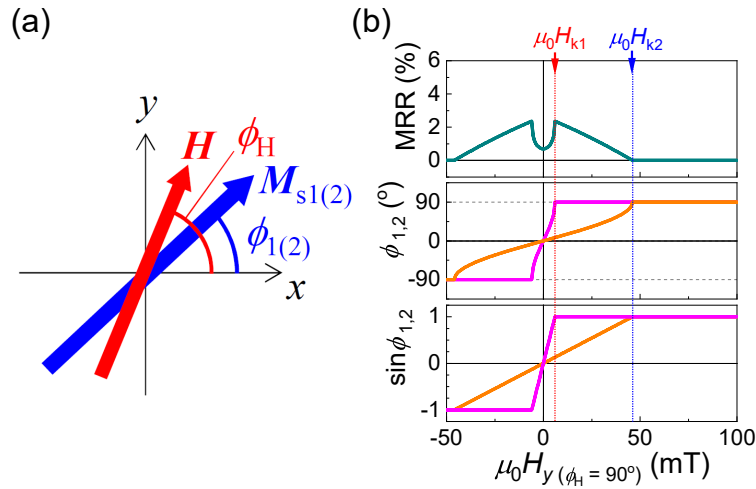
Figure 4.6: (a) The definition of angles used in the simulations. (b) An example of calculated results. Dependence of magnetoresistance ratio (MRR), magnetization direction $\phi_{1(2)}$ and y component of normalized magnetization $\sin\phi_{1(2)}$ on external magnetic field in y direction (H_y). The figures are taken from Ref. [57].

to the coherent rotation model, $\phi_{1(2)}$ for each H is determined as the value that satisfies the following conditions: $\partial E_{1(2)}/\partial \phi_{1(2)} = 0$ and $\partial^2 E_{1(2)}/\partial \phi_{1(2)}^2 > 0$. The middle panel of Fig. 4.6 (b) shows $\phi_{1(2)}$ dependence on H calculated with above method under $\mu_0 H_{k1(2)} = 6(46)$ mT. The bottom panel of Fig. 4.6 (b) shows the normalized magnetization curves, where

$\sin\phi_{1(2)}$ corresponds to y component of the normalized magnetization. The MR curve is then, calculated by

$$
\begin{aligned}
R &= R_0 + \Delta R_{\mathrm{GMR}} \frac{1 - \cos(\phi_1 - \phi_2)}{2} \\
&+ \Delta R_{\mathrm{AMR},1} \cos^2(\phi_1 - \phi_{\mathrm{J}}) + \Delta R_{\mathrm{AMR},2} \cos^2(\phi_2 - \phi_{\mathrm{J}}),
\end{aligned} \tag{4.3}
$$

where R_0, ΔR_{GMR}, $\Delta R_{\mathrm{AMR},1(2)}$ and ϕ_{J} are a constant part of resistance, GMR ratio, AMR ratio for ferromagnetic layer 1(2) and direction of the current, respectively. For the calculation of the top panel of Fig. 4.6 (b), the following parameters were used: $\Delta R_{\mathrm{GMR}}/R_0 = 4.3\%$, $\Delta R_{\mathrm{AMR},1(2)}/R_0 = 0.2(0.5)\%$ and $\phi_{\mathrm{J}} = 0°$.

The hysteresis is one of the differences between the experiment [Fig. 4.2 (c)] and the calculation [Fig. 4.6 (b)]. By introducing a small angle deviation which is difficult to be eliminated experimentally, such hysteresis is reproduced as shown in Fig. 4.7. The result
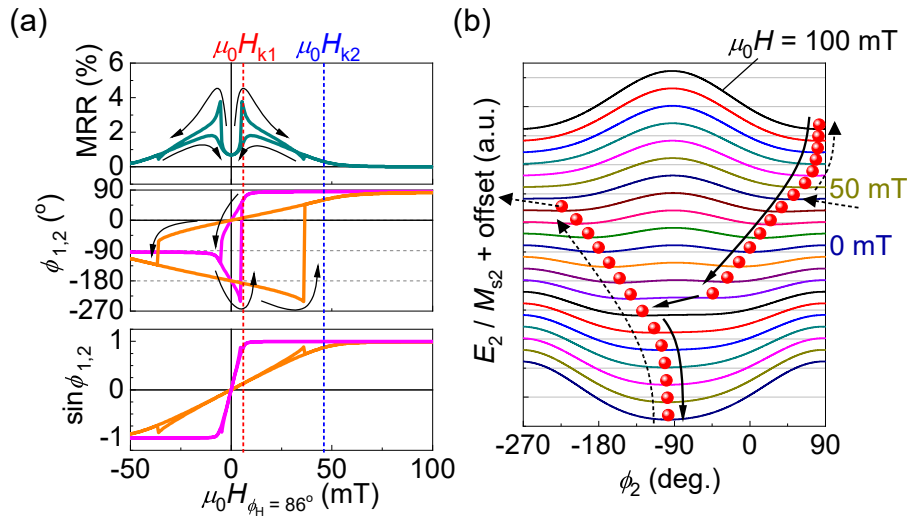
Figure 4.7: (a) The simulated results for magnetoresistance ratio (MRR), magnetization direction $\phi_{1(2)}$ and y component of normalized magnetization $\sin\phi_{1(2)}$ dependence on external magnetic field in $\phi_{\mathrm{H}} = 86°$ direction. (b) The ϕ_2 dependence of $E_2/M_{\mathrm{s}2}$ for each H with $\phi_{\mathrm{H}} = 86°$ (solid lines). The filled symbols represent the resultant magnetization angles for ferromagnetic layer 2. The figures are taken from Ref. [57].

shown in Fig. 4.7 (a) was calculated using the same parameters except for $\phi_{\mathrm{H}} = 86°$. The trajectory of the magnetization direction for the ferromagnetic layer 2 is shown in Fig. 4.7 (b), using the ϕ_2 dependence of $E_2/M_{\mathrm{s}2}$ for each H as an example. The slight deviation of

H from the y axis breaks the symmetry of the energy valley in $E_{1(2)}/M_{s1(2)}$ in the vicinity of $\phi_{1(2)} = \pm 90°$, which results in the hysteresis-behavior. The jumps in $\phi_{1(2)}$ were set to occur when the energy barrier on the way toward the energy minimum point was eliminated. In the realistic case, however, such a jump occurs despite the existence of the energy barrier (e.g. a coercivity is usually much smaller than an anisotropy field). Therefore, a better setting for the $\phi_{1(2)}$ jump conditions may lead to a better simulation result.

The influence of the jumps to the MR curve is, however, occasionally small due to the symmetry of the GMR effect [e.g. around $\mu_0 H_{\phi_\text{H}=86°} = 30$ mT in Fig. 4.7 (a)]. Another effect of the ϕ_H deviation is the increase in the saturation field. Though the saturation field corresponds exactly to H_{k2} in Fig. 4.6 (b), the saturation field becomes slightly larger than H_{k2} in Fig. 4.7 (a). This point should be in consideration for the analysis of MR curves.

4.2.5   Pseudo spin valve with strain insensitive Co

So far, we have discussed the basis of the inverse magnetostriction effect on a pseudo spin valve. One may suppose that a use of a strain-insensitive ($B_\text{eff} = 0$) ferromagnetic layer is instrumental in using the pseudo spin valve as a strain sensor. For a large resistance change, $\phi_1 - \phi_2$ should be largely changed. Therefor, one of the ferromagnetic layers should be strain-sensitive (large B_eff), whose magnetization can be sensitively rotated by an external strain application, and the other should be strain-insensitive being invariant with the external strain. The results in Chap. 3 will help control B_eff of Co, e.g. a Cu under layer reduces B_eff. However, in a layer structure of Pt/Co/Cu/Co from the lower side, the upper Co layer tends to have a larger B_eff since the fcc (111) texture is inherited from the lower layers as can be seen in Fig. 4.5. A thick Co layer, which also gives a small B_eff, decreases the GMR ratio due to the increase of a shunt current.

Finally we tried to make the lower Co layer strain-insensitive. The layer structure used was Ta(2.5 nm)/Cu(2.0 nm)/Co(4.0 nm)/Cu(4.5 nm)/Co(1.6 nm)/Pt(1.8 nm) from the substrate side [Fig. 4.8 (c)], hereinafter, referred to as the insensitive-Co-GMR. The upper Co layer was made thin in order to enhance B_eff in the Cu/Co/Pt structure. Figure 4.8 (a) shows the MR curves for H_x under various ε_x. Magnetization switching of the upper Co layer is abrupt, and the magnitude of the switching field increases with increasing ε_x, indicating that

Figure 4.8: Magnetoresistance curves of the insensitive-Co-GMR with different strains ε_x under external magnetic fields (a) parallel and (b) perpendicular to the tensile strain direction. Each curve has an offset in the magnetoresistance ratio (MRR). (c) Layer structure of the insensitive-Co-GMR. The figures are taken from Ref. [57].

the top layer has a positive B_{eff} value. Indeed, the saturation field under H_y increases as ε_x increases. No sharp switching is observed in the lower Co layer, probably because the application of a strain cannot cause the film to take on a single-domain state in the vicinity of zero magnetic field because of the small magnetic anisotropy. Although the Co layers were successfully engineered to be strain-sensitive and strain-insensitive, GMR ratio and H_k induced by the strain are not so high. Better characteristics are observed in another sample, which is discussed in the following part.

4.2.6   Pseudo spin valve with strain insensitive NiFe

Here, a $Ni_{80}Fe_{20}$ alloy (denoted as NiFe) layer was used as the strain-insensitive layer. The NiFe is known to have a small magnetoelastic constant (e.g. $B_{\text{eff}} = -0.08$ MJ/m^3 as a bulk [58]). The layer structure used here was Ta(2.5 nm)/Pt(2.0 nm)/Co(3.5 nm)/Cu(4.0 nm)/Co(0.4 nm)/NiFe(3.8 nm)/Cu(2.0 nm) from the substrate side [Fig. 4.9 (c)], hereinafter, referred to as the insensitive-NiFe-GMR. Since the Co/Cu interfaces contribute to the high GMR ratio, an extremely thin Co layer was inserted between Cu and NiFe layers, which is known to enhance the GMR ratio of spin valves using NiFe [83].

Figure 4.9 (a) shows the MR curves for H_x obtained under various values of ε_x. Typical GMR characteristics are observed when $\varepsilon_x > 0\%$. The GMR ratio ($\sim 6.5\%$) is even higher than
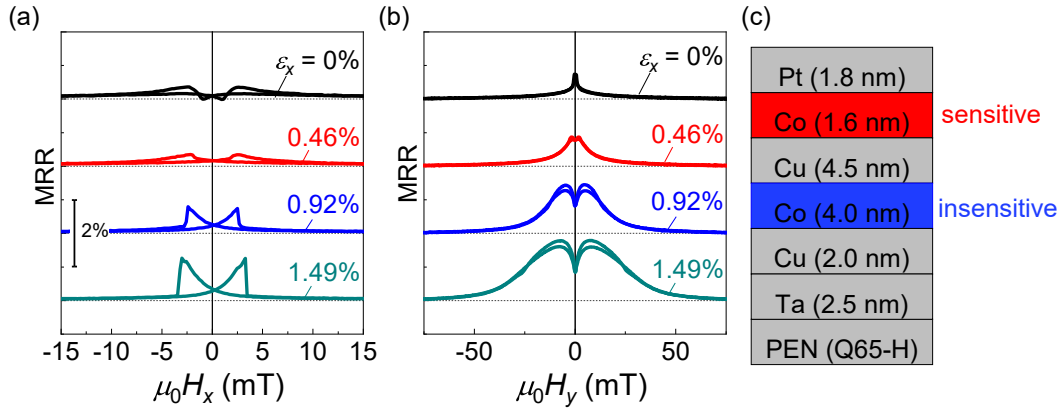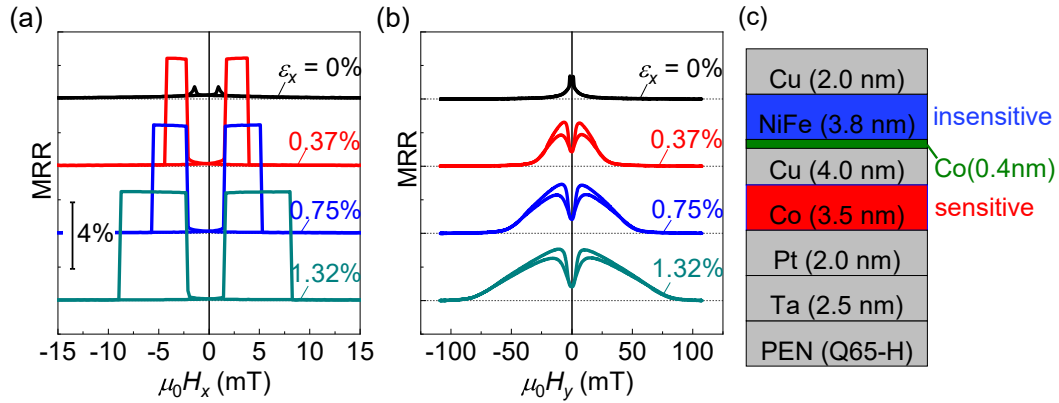
Figure 4.9: Magnetoresistance curves of the insensitive-NiFe-GMR with different strains ε_x under external magnetic fields (a) parallel and (b) perpendicular to the tensile strain direction. Each curve has an offset in the magnetoresistance ratio (MRR). (c) Layer structure of the insensitive-NiFe-GMR. The figures are taken from Ref. [57].

that of the basic sample. Importantly, the inner switching field is insensitive to ε_x, whereas the magnitude of the outer one clearly increases with increasing ε_x. This indicates that the NiFe and Co layers are indeed the strain-insensitive and strain-sensitive layers, respectively, as expected. Figure 4.9 (b) shows the MR curves for H_y obtained under various values of ε_x, from which the dependence on ε_x of the anisotropy fields H_k of the NiFe and Co layers could be determined by fitting simulated curves to the experimental data.
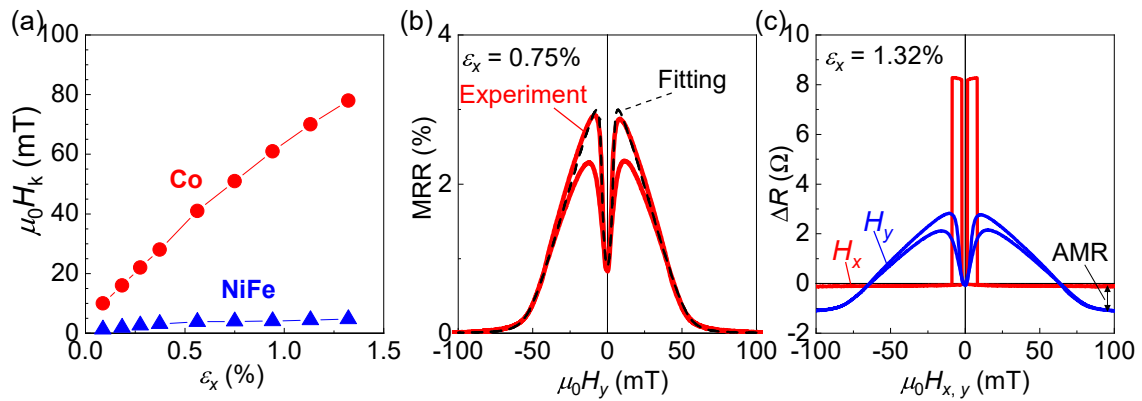
Figure 4.10: (a) Fitting parameters (anisotropy fields H_k) dependence on the external strain ε_x for the Co and NiFe layers. (b) An example of the fitting for $\varepsilon_x = 0.75\%$. (c) Magnetoresistance curves for different field directions (H_x and H_y) for $\varepsilon_x = 1.32\%$. The vertical axis ΔR is a resistance difference from the resistance at zero field. The figures are taken from Ref. [57].

Figure 4.10 (a) shows ε_x dependence of the fitting parameters H_k for the Co and NiFe layers. For the NiFe layer, H_k is nearly insensitive to ε_x, whereas for the Co layer it increases almost linearly with increasing ε_x. An example of best-fit simulated results is shown in Fig. 4.10 (b). Only one of the hysteresis was fitted for simplicity. The influence of the multi-domain state appears to be small for this experiment as shown in Fig. 4.10 (c), in contrary to the case of Fig. 4.3. The fittings of H_k for different ε_x were performed with other parameters fixed: $\Delta R_{\mathrm{GMR}}/R_0 = 6.48\%$, $\Delta R_{\mathrm{AMR,1}}/R_0 = 0.25\%$ for the NiFe layer and $\Delta R_{\mathrm{AMR,2}}/R_0 = 0.6\%$ for the Co layer.

4.3 Strain sensing characteristic

In this section, the resistance change under a continuous change in the external strain ε_x is discussed.

4.3.1 Pseudo spin valve

Here, the insensitive-NiFe-GMR in the previous section is used. Figure 4.11 (a) shows raw data of R change while sweeping ε_x under different H_y. Under a large field (the top panel), R change is linear due to the metal-size dependence (Eq. 3.2), where the magnetization directions are fixed by the large field. On the other hand under a smaller field (the bottom panel), a non-linear behavior appears, suggesting magnetoresistive contribution. The magnetoresistive contribution is shown in Fig. 4.11 (b). The metal-size contribution (slope of the top panel) is subtracted from the bottom panel and converted to the resistance change ratio $\Delta R/R_0$, where $\Delta R = R - R_0$ and R_0 is R at $\varepsilon_x = 0$. Around $\varepsilon_x = 0\%$, R is small since the magnetization directions are parallel obeying H_y, while R becomes larger at a larger ε_x since the magnetization direction of the strain-sensitive Co layer changes with the inverse magnetostriction effect.
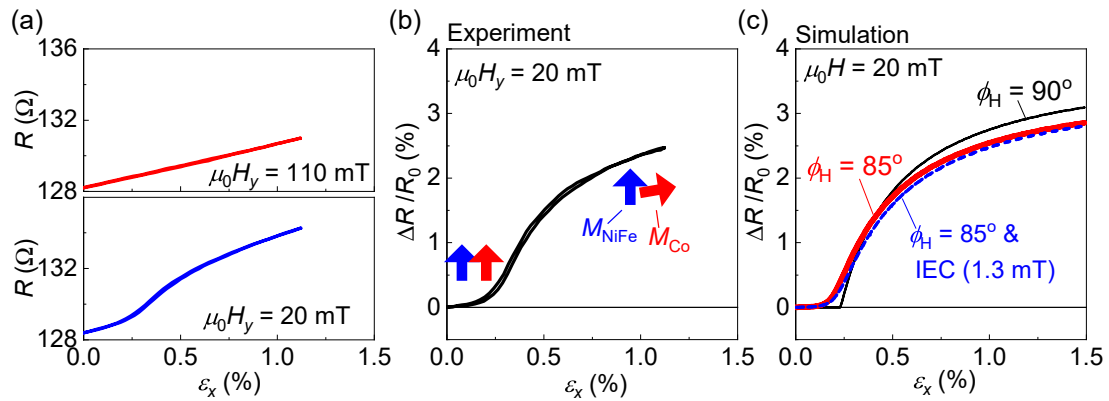
Figure 4.11: (a) Raw resistance R data with strain ε_x sweeping under different field H_y in the y direction. (b) Resistance change rate without the metal-size dependence. The arrows denote the magnetization directions of Co and NiFe. (c) Simulation results for resistance change. The figures are taken from Ref. [57].

This behavior can be simulated by expanding the coherent magnetization rotation model, as shown in Fig. 4.11 (c). We assumed that the additional uniaxial anisotropy field $H_{k1(2)}$

is induced proportionally to the applied strain ε_x as $H_{k1(2)} = h_{k1(2)}\varepsilon_x$, where magnetoelastic anisotropy field constant $h_{k1(2)}$ is related to B_{eff} as $\mu_0 h_k = 2B_{eff1(2)}/M_{s1(2)}$. By adding this effect to Eq. 4.2 and generalizing the direction ϕ_ε of a strain ε, the energy densities for the two ferromagnetic layer ($E_{1(2)}$) can be written as

$$\frac{E_{1(2)}}{M_{s1(2)}} = -\frac{\mu_0 h_{k1(2)}}{2}\varepsilon\cos^2(\phi_{1(2)} - \phi_\varepsilon) - \frac{\mu_0 H_{u1(2)}}{2}\cos^2\phi_{1(2)} - \mu_0 H\cos(\phi_H - \phi_{1(2)}), \quad (4.4)$$

where $H_{u1(2)}$ is the anisotropy field initially exists in the ferromagnetic layer 1(2). The magnetization direction $\phi_{1(2)}$ that makes $E_{1(2)}$ minimum is determined for each ε value and R is calculated with Eq. 4.3. Lines in Fig. 4.11 (c) are calculated using the results obtained in Fig. 4.10: $B_{eff1(2)} = 0.99(4.0)$ MJ/m^3, $M_{s1(2)} = 0.80(1.4)$ MA/m, $\Delta R_{GMR}/R_0 = 6.48\%$, $\Delta R_{AMR1(2)}/R_0 = 0.25(0.6)\%$, $H_{u1(2)} = 1.8(7.0)$ mT, where the ferromagnetic layer 1(2) corresponds to NiFe(Co), and $\phi_\varepsilon = 0°$. The thin black line is calculated under $\phi_H = 90°$, $\mu_0 H = 20$ mT, showing abrupt R increase around $\varepsilon_x = 0.25\%$. The threshold strain ε_{th} is analytically derived from $\partial^2 E_2/\partial\phi_2^2|_{\phi_2=90°} = 0$ if $\phi_\varepsilon = 0°$, $\phi_H = 90°$ as

$$\varepsilon_{th} = \frac{H - H_{u2}}{h_{k2}}. \quad (4.5)$$

The resistance change due to magnetoresistance effects is suppressed if $\varepsilon < \varepsilon_{th}$, verifying that the resistance change in the top panel of Fig. 4.11 (a) can attributed purely to the metal-size dependence. The smooth change in Fig. 4.11 (b) is reproduced by assuming a small angle deviation ($\phi_H = 85°$), shown as the thick red line in Fig. 4.11 (c). The dashed blue line verifies that the inter layer exchange coupling (IEC) of 1.3 mT, which is aware in Fig. 4.4, has negligible effect.

The strain ε sweeping measurements with various strain directions ϕ_ε were also performed as shown in Fig. 4.12. In order to change ϕ_ε, samples with different current directions ϕ_J with respect to the longitudinal direction of the substrate were used and a magnetic field was applied perpendicular to ϕ_J ($\phi_H = 90°$). This condition was set to make the AMR (as well as GMR) contribution to be the same as a situation that strains with different ϕ_ε are applied with respect to the fixed ϕ_J and ϕ_H. Figure 4.12 (a) shows experimental results under different ϕ_ε. The resistance change becomes smaller as ϕ_ε becomes smaller since the magnetization

direction change in the Co layer becomes smaller. The similar curves can be reproduced by the simulations as shown in Fig. 4.12 (b). At a large strain ($\varepsilon > 1.0\%$), the resistance saturates to a value depending on ϕ_ε. Figure 4.12 (c) compares the resistance at $\varepsilon = 1.0\%$ of the experiments and the simulations. The difference between the experiments and the simulations is probably caused by an angle deviation in the experimental setup as suggested in Fig. 4.11 (c). These results show that the strain direction can be measured with this device.
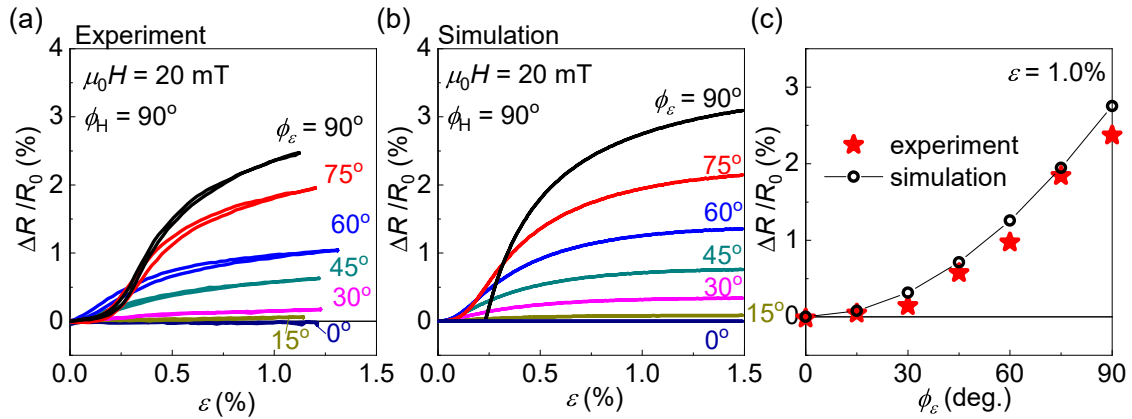
Figure 4.12: Resistance change ratio $\Delta R/R_0$ dependence on strains ε with various strain directions ϕ_ε of (a) experiments and (b) simulations. (c) Comparison of the experiments and simulations of $\Delta R/R_0$ dependence on ϕ_ε at $\varepsilon = 1.0\%$. The figures are taken from Ref. [57].

By using conventional strain gauges, the strain direction is determined by using three strain gauges. On the other hand, this magnetoresistive strain sensor determines the strain direction with a single resistance measurement (if the magnitude of the strain is large enough). The requirement of a large strain is, however, one of the problems. The external magnetic field H, which was applied to avoid magnetization rotation or occurrence of the multi-domain state in the NiFe layer, is the main factor for the gradual saturation behavior since H hampers the magnetization rotation of the strain-sensitive Co layer. In the following section, reduction of the required strain is attempted using the exchange bias [70], which can induces an internal field to a selective ferromagnetic layer.

4.3.2 Spin valve

Here, a spin valve sample with the layer structure of Ta(2.2 nm)/Pt(2.0 nm)/Co(2.1 nm)/Cu(4.0 nm)/Co(0.5 nm)/NiFe(2.0 nm)/FeMn(10.5 nm)/ Pt(2.2 nm) from the substrate side was used. The composition of the antiferromagnetic FeMn layer was $Fe_{50}Mn_{50}$. The sample was annealed at 220°C for 10 minutes and cooled down to the room temperature under an magnetic field of 0.5 T whose direction determines the exchange bias direction. A polyimide film (UPILEX® S50) was used as a substrate so that the sample can bare the annealing process.
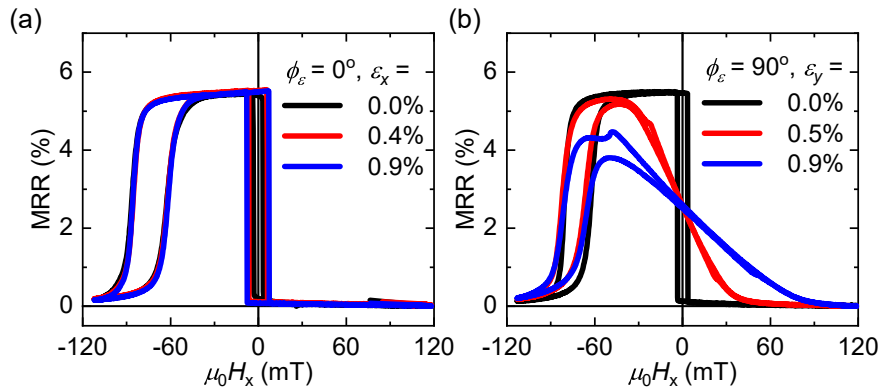
Figure 4.13: Magnetoresistance curves of the spin valve sample under external field H_x in $\phi_H = 0°$ with different strain directions (a) $\phi_\varepsilon = 0°$ and (b) $\phi_\varepsilon = 90°$. The figures are taken from Ref. [84].

Figures 4.13 (a) and (b) show MR curves of the spin valve sample under strain directions $\phi_\varepsilon = 0°$ and $\phi_\varepsilon = 90°$, respectively. The magnetic field direction $\phi_H = 0°$ was parallel to the direction of the exchange bias field H_{EB} for both cases. Typical MR curves for the exchange biased spin valves, i.e. abrupt resistance changes around $\mu_o H_x = -80$ mT due to the magnetization reversal in the exchange biased NiFe layer and those around $\mu_o H_x = 0$ mT due to the magnetization reversal in the Co layer, are seen in Fig. 4.13 (a). The magnetization reversal field of the Co layer increases as ε_x increase, while that of the NiFe layer remains unchanged, suggesting that both exchange bias and coercivity of the NiFe are invariant with the strain ε_x. When a strain is applied in y direction [Fig. 4.13 (b)], the MR curves change clearly since the magnetic easy axis of the Co layer becomes in y direction. Though a change in the MR curves around $\mu_0 H_x = -80$ mT is aware, the exchange bias is supposed to be

invariant also with ε_y since the fields for NiFe magnetization reversal are almost unchanged.
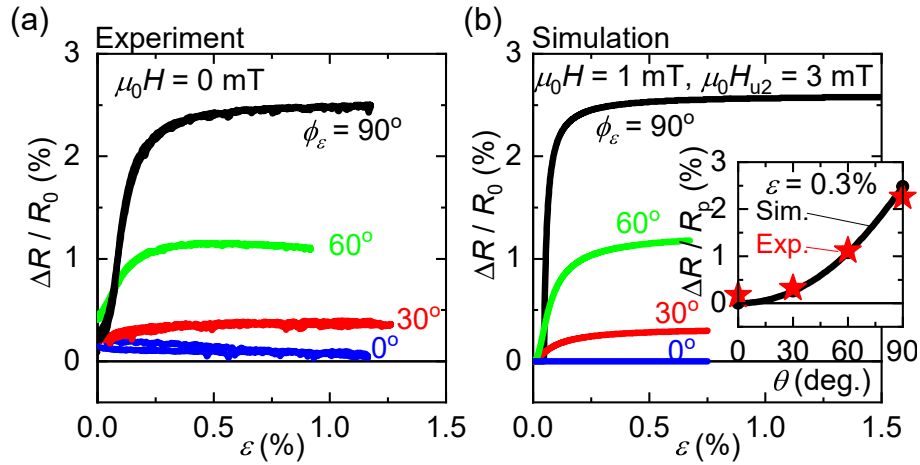
Figure 4.14: (a) Resistance change ratio dependence on strains ε with different strain directions ϕ_ε of the spin valve sample. Here, R_0 is the resistance under a large magnetic field. (b) Simulation results of the resistance change. The inset compares values of the experiments and the simulations at $\varepsilon = 0.3\%$. The figures are taken from Ref. [84].

Figure 4.14 (a) shows ϕ_ε dependence of resistance change with the ε sweeping without an external magnetic field. The resistance changes more rapidly compared to Fig. 4.12 (a) and saturates around $\varepsilon = 0.3\%$. Simulation results are shown in Fig. 4.14 (b). For the simulation, $\mu_0 H = 1$ mT in $\phi_H = 90°$ was assumed though the field was not applied experimentally. This assumption is supposed to successfully reflects an existence of the inter layer exchange coupling (Fig. 4.4), which affects the magnetization rotation of the Co layer. The uniaxial anisotropy field in the Co layer $\mu_0 H_{u2} = 3$ mT is also important to simulate the behavior. For the enhancement of the strain direction sensitivity, minimization of the inter layer exchange coupling and the initially induced uniaxial magnetic anisotropy in the strain-sensitive layer (H_{u2}) is effective according to Eq. 4.5.

Anyway, the introduction of the exchange bias largely improves the strain direction sensing characteristic. At the same time, the unnecessity of the external magnetic field makes the device suitable for practical use. Figure 4.15 shows the demonstration of finger motion sensing by the spin valve device. Here, 25-μm-thick Kapton® EN was used as a substrate and cut into the shape shown in Fig. 4.15 (a) and mounted on the back of a human hand, where a tensile strain in the direction of each finger is applied to the spin valve device at the center
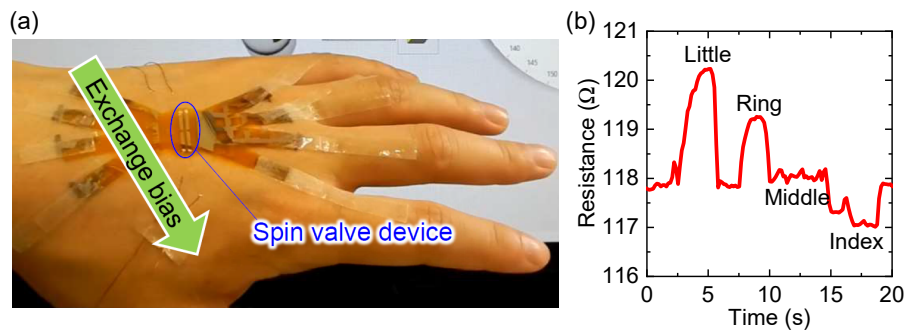
Figure 4.15: (a) A photograph of the spin valve device mounted on the back of a human hand. The exchange bias direction is perpendicular to the little finger direction. (b) Resistance of the spin valve device monitored while bending fingers in order. The figures are taken from Ref. [84].

when each finger is bent. The exchange bias direction was set to be perpendicular to the little finger direction. The current (wire) direction was parallel to the little finger direction. Figure 4.15 (b) shows the resistance monitored while the little, ring, middle and index fingers were bent in order. The resistance is highest when the little finger is bent corresponding to $\phi_\varepsilon = 90°$ in Fig. 4.14, and the resistance is lower for other fingers with smaller ϕ_ε. The resistance when the middle finger is bent seems to be the same as the resistance without strain, indicating that the initial magnetization direction of the Co layer is in the middle finger direction, which is probably a result of a conflict between the interlayer exchange coupling (parallel to the exchange bias direction) and the initially induced uniaxial anisotropy H_{u2} in the wire direction.

4.4 Summary of this chapter

In this chapter, the combination of the giant magnetoresistance and inverse magnetostriction effects has been studied. The magnetoresistance curves of the pseudo spin valve devices have changed drastically with the strain application. In consideration of the uniaxial magnetic anisotropy induced by the strain, the anisotropic magnetoresistance effect, the slight experimental angle deviation and so on, the coherent magnetization rotation model has reproduced the magnetoresistance curves. The resistance changes with strain sweeping have been measured under various strain directions. The strain sweeping characteristic has also been reproduced by the simulation similar to the magnetoresistance curve simulation. The pseudo spin valve device with one of the magnetic layers insensitive to strain and the other sensitive to strain, is supposed to be used as a strain direction sensor, whose resistance saturates with strain application to the value depending on the strain direction.

The use of the exchange bias has decreased the strain necessary to determine the strain direction. At the same time, it becomes unnecessary to apply an external field, which makes the device suitable for a practical application. In fact, the finger motion sensing has been demonstrated.

One of the problems to be solved is the magnetoresistance ratio. The devices shown in this chapter have the giant magnetoresistance ratio of ~5-7%, and only a half of the ratio can be used in these devices, which is still comparable to the conventional resistance dependence on the metal shape. In the next chapter, following the history of the spintronics, the tunnel magnetoresistance effect is focused on.

Chapter 5

Formation of magnetic tunnel junction on flexible substrate

In this chapter, the magnetic tunnel junction (MTJ) on a flexible substrate is discussed. Section 5.1 briefly introduces the tunnel magnetoresistance (TMR) effect and previous studies for the formation of MTJ on a flexible substrate. In Sec. 5.2, the fabrication process and annealing temperature dependence of the TMR properties are shown. In Sec. 5.3, the results of the strain application to the MTJ samples are shown and discussed. In Sec. 5.4, the characteristics of the magnetoelastic strain sensors (including the GMR-based sensors in the previous chapter) are discussed and other types of the magnetoelastic sensors are proposed.

5.1 Tunnel magnetoresistance effect

5.1.1 Introduction of tunnel magnetoresistance effect

The MTJ is the structure of an insulator layer sandwiched by two ferromagnetic layers. Similarly to the giant magnetoresistance (GMR) effect, a tunnel resistance of the MTJ depends on the relative angle of the two magnetizations as Eq. 4.1 in the TMR effect. The TMR effect is explained by the spin dependent tunneling as follows (Julliere's model [85]). At the Fermi level of a ferromagnetic metal, up and down spins have different electronic state due to the exchange interaction. Assuming electrons tunnel without spin flip, the conductance

is proportional to $a_1 a_2 + (1 - a_1)(1 - a_2)$ with parallel magnetizations and to $a_1(1 - a_2) +$ $a_2(1 - a_2)$ with antiparallel magnetizations, where $a_{1(2)}$ is the fraction of tunneling electrons in ferromagnetic layer 1(2) whose magnetic moments are parallel to the magnetization direction. Starting from the above assumption, the magnetoresistance ratio (MRR) can be written as

$$\frac{R_{AP} - R_P}{R_P} = \frac{2P_1 P_2}{1 - P_1 P_2}, \tag{5.1}$$

where R_{AP}, R_P are the resistance for antiparallel and parallel magnetizations, and the spin polarization is $P_{1(2)} = 2a_{1(2)} - 1$.

The TMR effect in room temperature was firstly observed using an amorphous aluminum oxide tunnel barrier [86, 87]. Although the MRR is higher than that of a GMR with two ferromagnetic layers, the TMR cannot exceed 70% with the spin polarization of the conventional $3d$ transition metals based on the Julliere's model. There are two ways to enhance the TMR ratio. One of them is to use the half metal, whose spin polarization is $P_{1(2)} = 1$ and Eq. 5.1 can be infinitely large. The other is to use the coherent tunneling effect, or the spin filtering effect, which is firstly proposed theoretically [88]. Normally, various Bloch states
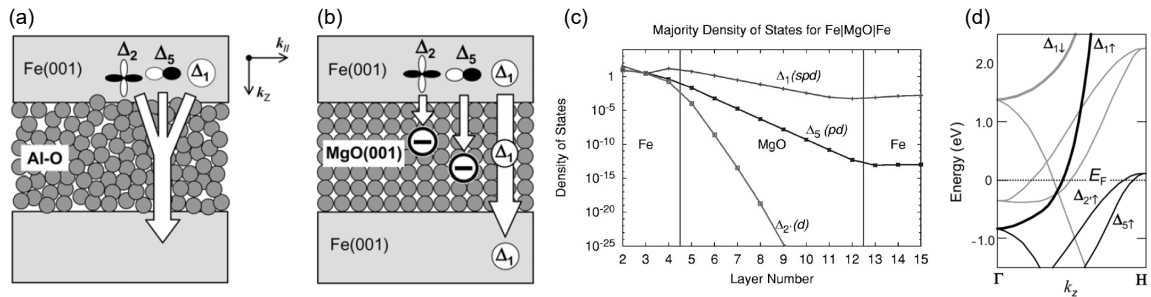
Figure 5.1: (a) Schematics of electron tunneling through (a) an amorphous aluminum oxide barrier and (b) a crystalline MgO (001) barrier, taken from [89]. (c) Tunneling density of state for majority spins in Fe/8MgO/Fe with (001) orientation, taken from [88]. (d) Band dispersion of bcc Fe in the [001] direction, taken from [89].

with different symmetries exist in a ferromagnetic electrode as shown in Figs. 5.1 (a) and (b). In case of the amorphous aluminum oxide tunnel barrier without crystallographic symmetry, Bloch states with various symmetries couples with evanescent states in the aluminum oxide and have finite tunneling probabilities [Fig. 5.1 (a)]. On the other hand in case of a crystalline MgO(001) tunnel barrier, only a Δ_1 state (spd hybridized state) coherently tunnel through the

barrier as shown in Fig. 5.1 (b). Figure 5.1 (c) shows the density of states (DOS) obtained by first-principle calculations of the Fe/MgO/Fe system, whose evanescent states in the MgO layer decay. The decay of the Δ_1 state is the slowest of the various Bloch states. Since the Δ_1 state often has a high spin polarization, this band selective tunneling results in a high TMR ratio. Figure 5.1 (d) shows the band structure of bcc Fe for example. Only DOS of up spin exists at the Fermi level E_F for the Δ_1 state.

The MRR well above the Julliere's limit $\sim$70% was experimentally observed later [90,91]. The epitaxially grown Fe/MgO/Fe MTJ shows MRR of $\sim$180% at room temperature [90]. It was also reported that even a sputter deposited CoFe/MgO/CoFe structure [Fig. 5.2 (a)] shows a high MRR of $\sim$220% after annealing at 350°C [91]. Further higher TMR ratios (604% at highest) have been obtained using amorphous CoFeB (CFB) electrodes [89, 92–98]. These CFB/MgO-based MTJs are also suitable for high density memory since a thin CFB layer has perpendicular magnetic anisotropy [99]. The amorphous CFB layer serves as a buffer
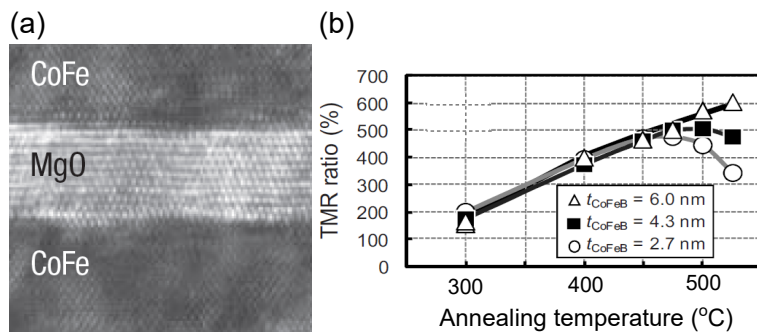
Figure 5.2: (a) A transmission electron microscope image of the sputter deposited CoFe/MgO/CoFe layers, taken from [91]. (b) Annealing temperature dependence of the TMR ratio of the CoFeB/MgO/CoFeB structures with different CoFeB layer thickness t_{CoFeB}, taken from [98] and modified.

layer for the growth of polycrystalline MgO (001). Then, bcc (001) crystallization in the CFB layers and the enhancement of the crystallinity in the MgO layer occur during annealing above 300°C, resulting in the structure suitable for the coherent tunneling effect. Figure 5.2 (b) shows the TMR ratio dependence on the annealing temperature, indicating that high TMR ratios are obtained by annealing at 400-550°C. The reduction in the TMR ratio over 500°C is supposed to be caused by the diffusion of Ta under the lower CFB layer, which is suppressed

with a thicker CFB layer [98].

Highly sensitive strain sensors using the high TMR ratio of the CFB/MgO-based MTJs have been reported for a rigid substrate case [100–104]. The highest Gauge factor [= $(\Delta R/R_0)/\Delta\varepsilon$] of 4016 has been obtained by adjusting magnetic properties of the CFB layer [102].

5.1.2 Examples of flexible magnetic tunnel junction

Our aims being the formation of MTJs on a flexible substrate, a few studies reporting flexible MTJs are referred to here [15, 20, 26, 27]. Two of them used the aluminum oxide tunnel barrier [15, 20], as shown in Fig. 5.3. Without the requirement of the annealing process, no special treatment seems to be needed for observing the TMR effect. The TMR ratio of the flexible MTJs is no less than that of control samples made on rigid substrates. It was also confirmed that almost no change in the TMR ratio is seen during or after bending of the substrate. The TMR ratio has been no more than 20% for these aluminum oxide based flexible MTJs.
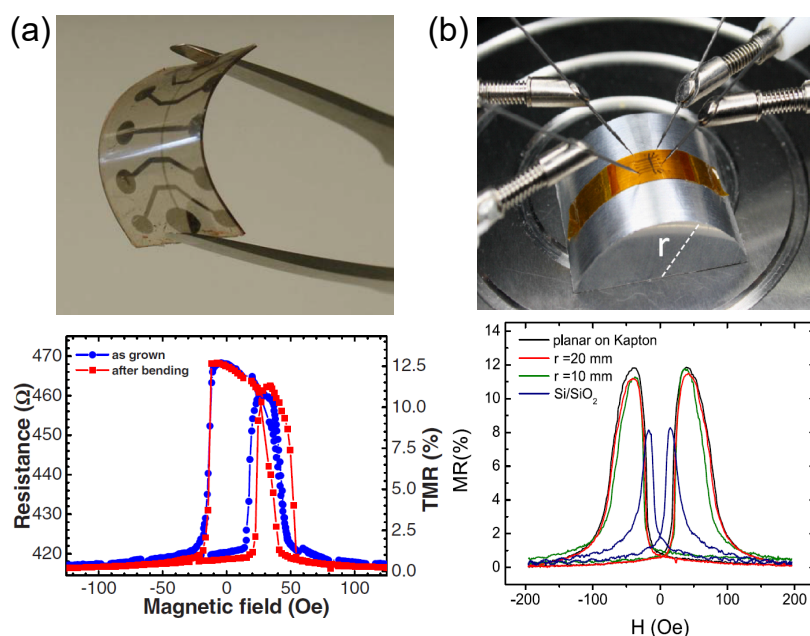
Figure 5.3: Photographs and the magnetoresistance curves of the aluminum oxide based MTJs on flexible substrates. (a) and (b) are taken from [15] and [20], respectively.

The CFB/MgO-based MTJs on flexible substrates were also reported, where the MTJs

were firstly made on a rigid substrate (including the annealing process) and transferred on to flexible substrates [26, 27]. Figure 5.4 (a) shows schematics of one of the transfer process. The Si under the MTJs was etched away and MTJs were transferred on to many kinds of substrates, one of which is shown in Fig. 5.4 (b). Interestingly, the MTJs after the transfer process have had a larger TMR ratio compared to that before the transfer process, as shown in Fig. 5.4 (c). The enhancement is attributed to the changes in magnetic anisotropy of the CFB layers or the electronic states caused by a strain induced by the transfer process. The
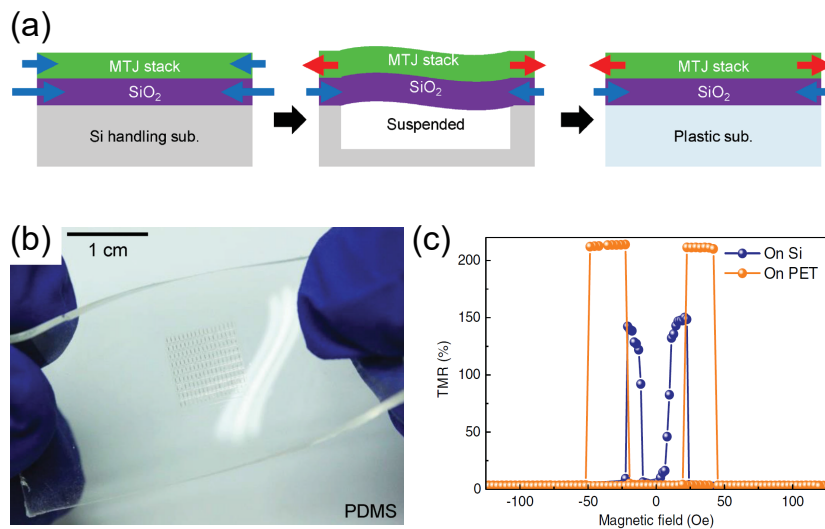
Figure 5.4: (a) Schematics of the transfer process, where the red and blue arrows indicate the stress in the layers. (b) A photograph of the MTJs transferred on a polydimethylsiloxane (PDMS) film. (c) Magnetoresistance curves of the MTJs before and after the transfer to a polyethylene terephthalate (PET) substrate. The figures are taken from [26].

other example for the flexible CFB/MgO-based MTJs was realized by etching the Si substrate from its back-side, down to the thickness of 14 μm and placing on to a Kapton® tape [27].

Although these transfer methods successfully avoid the damage in flexible substrates with the annealing process, there is a problem for using as strain sensors. A weak adhesion of the MTJs to the flexible substrates will deteriorate the strain sensing characteristics. Therefore, we attempt to fabricate the CFB/MgO-based MTJs directly on a flexible substrate in the following sections. Using only conventional processes, the methods will be suitable for mass production compared with the transfer process for a small area [Fig. 5.4 (b)].

5.2 Fabrication of magnetic tunnel junctions

5.2.1 Fabrication process

In order to endure the annealing process with the high annealing temperature $T_A \geq 300°C$, the polyimide UPILEX® was used as a substrate. Though a high TMR ratio can also be obtained using Kapton®, UPILEX® seems to be better since deformation of the Kapton® film is aware after annealing at $T_A \geq 400°C$. The layer structure of one of the MTJs were Ta(4.9 nm)/Ru(11 nm)/Ta(4.9 nm)/CFB(4.1 nm)/MgO(2.0 nm)/CFB(2.7 nm)/Ta(4.9 nm)/Ru(2.2 nm) from the substrate side. Composition of the CFB target used in this study was $Co_{20}Fe_{60}B_{20}$. Xe was used as the process gas for sputtering the metal targets. The use of Xe tends to result in a larger coercivity difference of the two CFB layers compared with the Ar gas case. Ar gas was used for sputtering the MgO targets. A lower Ar pressure and a higher sputtering power tend to enhance the TMR ratio.
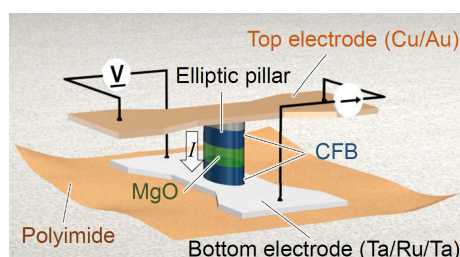
Figure 5.5: Schematics of the MTJ device. The aluminum oxide isolator is omitted from the illustration for simplicity. The figure is taken from Ref. [105].

In contrast to the GMR case in Chap. 4, an electric current needs to flow perpendicularly to the MgO tunnel barrier (pillar) for the measurements as shown in Fig. 5.5. Therefore, the following relatively complex fabrication processes were adopted (see also Fig. 5.6).

1. Photo-lithography and Ar-ion milling for the dog-bone shaped bottom electrode. This milling may be stopped before the substrate is exposed in order not to etch the substrate deeply with the additional milling process below.

2. Photo-lithography and Ar-ion milling for the pillar (and parts of the bottom electrode). The pillar was typically ellipse, where the lengths of the major and minor axes were 11 and 4 µm respectively. The sample plane may be tilted during the milling to avoid the

re-deposition of metal on the side of the pillar. This second milling should etch deeper than the MgO layer. The photo-resist was not removed at this point.

3. Atomic layer deposition of a 30-nm-thick aluminum oxide layer that electrically isolate the top and bottom electrodes. The photo-resist on the pillar was dissolved by sonication in N-methylpyrrolidone. The aluminum oxide layer on the photo-resist is eliminated simultaneously.

4. Formation of the top electrode by the lift-off process. Cu(30 nm)/Au(2.0 nm) layers were deposited using a resistance heating evaporation system after a photo-lithography. Although Cr deposition at first may enhance the adhesion of the top electrode, it was not adopted because the radiant heat during the Cr layer deposition scorches the photo-resist and makes the lift-off difficult, which is possibly because of a low thermal conductivity of the flexible substrate.

5. Annealing in vacuum. The sample is annealed in a tubular furnace without magnetic field. The temperature was kept at the specified temperature T_A for 1 hour (otherwise noted).

Note that their is no special difference from the conventional processes for a rigid substrate.
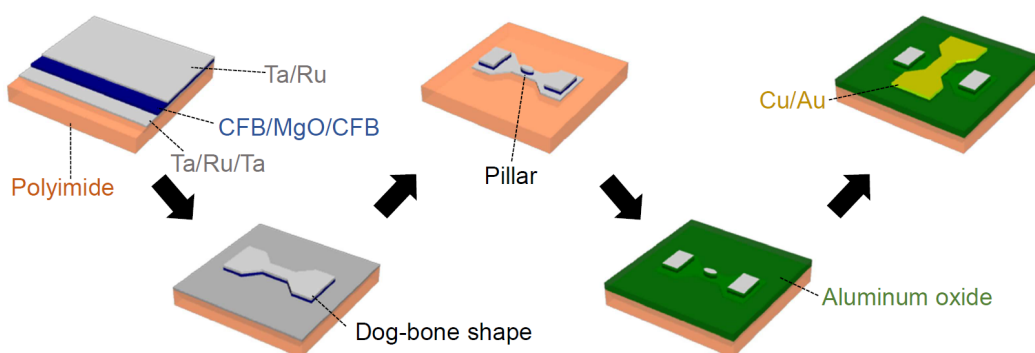
Figure 5.6: Schematics of the MTJ device fabrication processes.

For the 4-wire resistance measurement of the MTJs, the voltage-source mode of the SourceMeter® was used. This sets the voltage applied to the MTJ to be constant regardless of the resistance change. In the following measurements, a bias voltage V_B = +10 mV was

applied if not mentioned. Here, the positive sign of the voltage is defined that a current I flows from top to bottom electrodes through the pillar as illustrated in Fig. 5.5.

5.2.2 Annealing temperature
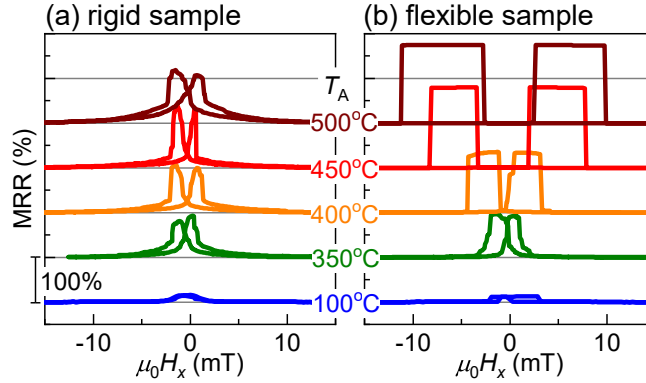
Figure 5.7: Magnetoresistance curves with different annealing temperature T_A on (a) a thermally oxidized Si substrate and (b) a polyimide substrate. The figures are taken from Ref. [105].

The typical magnetoresistance (MR) curves for the rigid (with a thermally oxidized Si substrate) and flexible (with a UPILEX® substrate) samples for various T_A are shown in Figs. 5.7 (a) and (b), respectively. Here, $T_A = 100°C$ indicates that the samples have no intentional annealing, since there are unavoidable heating processes (e.g. prebaking of the photo-resist at 90°C) during the MTJ fabrication. An external magnetic field (H_x) was swept in the minor axis direction of the elliptic pillar, which is defined to be the x axis. As a result, a clear TMR effect is observed in both samples. The TMR ratio reached 100% for the flexible sample after the 350°C annealing. What is more important is that a further increases in the TMR ratio in both samples are seen with the additional annealing at higher temperatures. Interestingly, the flexible sample tends to have a higher TMR ratio. It seems that the x axis is not perfectly the magnetic easy axis direction for the top and the bottom CFB layers in the rigid sample, judging from the MR curves with the moderate shapes and the small coercivity differences. On the other hand, clear square-like MR curves can be seen for the flexible sample with the higher T_A, which suggests that the x axis is the magnetic easy axis and the clear coercivity difference

of the two CFB layers is realized. The etching or heating processes to the ellipse pillar on the flexible substrate is supposed to induce an additional uniaxial magnetic anisotropy in the CFB layers, which can cause such a coercivity difference. As for the heating process, the larger thermal expansion (the linear thermal expansion coefficients of the polyimide and Si at room temperature are 1.6×10^{-5} /K and 2.6×10^{-6} /K, respectively) or the thermal contraction of the plastic may yield anisotropic strains in the ellipse pillar. In addition to the strain induced during the MTJ fabrication process, a difference in the effective magnetoelastic constants B_{eff} of the top and bottom CFB layers, which will be discussed in the next section, results in the coercivity difference observed here.
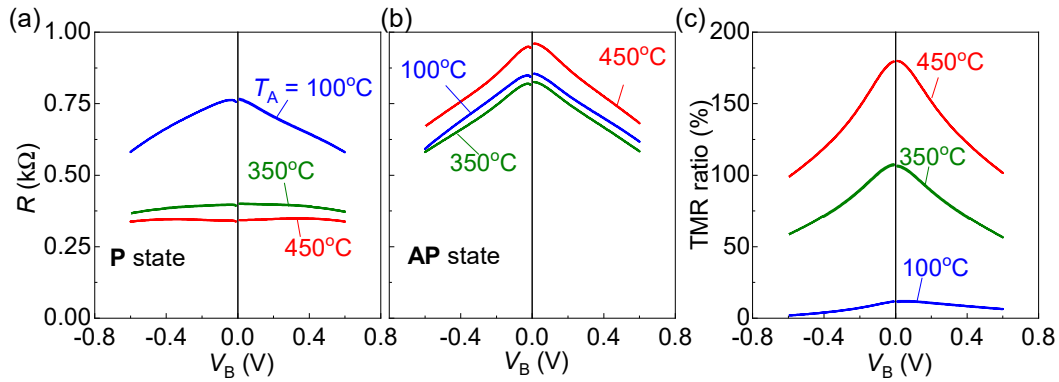
Figure 5.8: Bias voltage V_B dependence of resistance R for the flexible sample with (a) a parallel (P) magnetization state and (b) an antiparallel (AP) magnetization state. (c) TMR ratio dependence on V_B calculated from (a) and (b). The figures are taken from Ref. [105].

Figures 5.8 (a) and (b) show the resistance R of the flexible sample as a function of V_B at parallel (P) and antiparallel (AP) magnetization states (R_P and R_{AP}). The R_P becomes almost independent of V_B after the high temperature annealing ($T_A \geq 350°C$), while the mountain-like shape of R_{AP}-V_B curves is almost unchanged. Figure 5.8 (c) shows TMR ratio dependence on V_B, calculated from the data in Figs. 5.8 (a) and (b). The TMR ratio decreases as $|V_B|$ increases. For $T_A = 450°C$, the TMR ratio is larger than 100% for $|V_B| \leq 0.6$ V, assuring an output voltage [(TMR ratio) $\times |V_B|$] can be higher than 0.5 V, which is one of the requirements for gigabit-scale MRAMs [90]. Since these characteristics have generally been seen in similar CFB/MgO-based MTJs formed on a rigid Si substrate [94], it is supposed that the high temperature annealing of the flexible sample also improves crystallization of the

MgO layer.
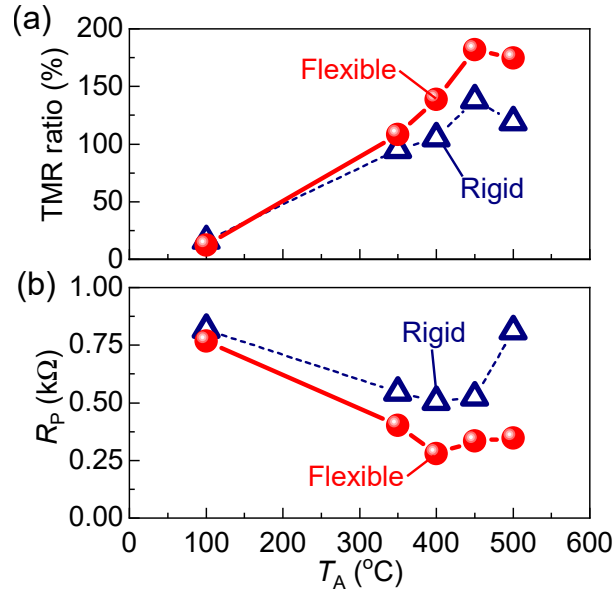
Figure 5.9: Dependence of (a) the TMR ratio and (b) the resistance at the parallel magnetization state (R_P) on annealing temperature T_A for the rigid and flexible samples. The figures are taken from Ref. [105].

Figures 5.9 (a) and (b) summarize the T_A dependence of the TMR ratio and R_P for both samples. The previous report using MTJs formed on a rigid Si substrate also shows a similar trend [98] [Fig. 5.2 (b)]. Interesting point is that the TMR ratio reduction and the R_P increase at T_A = 500°C are suppressed in the flexible sample. Although the reason is yet to be understood, this may suggest that Ta diffusion into the bottom CFB layer, which is supposed to be a cause of the reduction in the TMR ratio [98], is suppressed.

Figures. 5.10 (a) and (b) show the bright-field scanning transmission electron microscope (STEM) images for the flexible samples annealed at 350°C and 500°C, respectively. The exactly same MTJ fabrication process applied to the samples for the above resistivity measurements was also applied to the samples used for the STEM observation. The two dimensional fast Fourier transform (FFT) images for the upper CFB, MgO and lower CFB layers are shown in panels A, B, and C in Fig. 5.10, respectively. An improved crystallinity is confirmed at a higher T_A (= 500°C) from the FFT images, particularly in the lower CFB layer. Although the upper CFB and MgO layers show only a small change in FFT images, the sharper CFB/MgO interface and MgO layers can be confirmed in the enlarged view (inset)
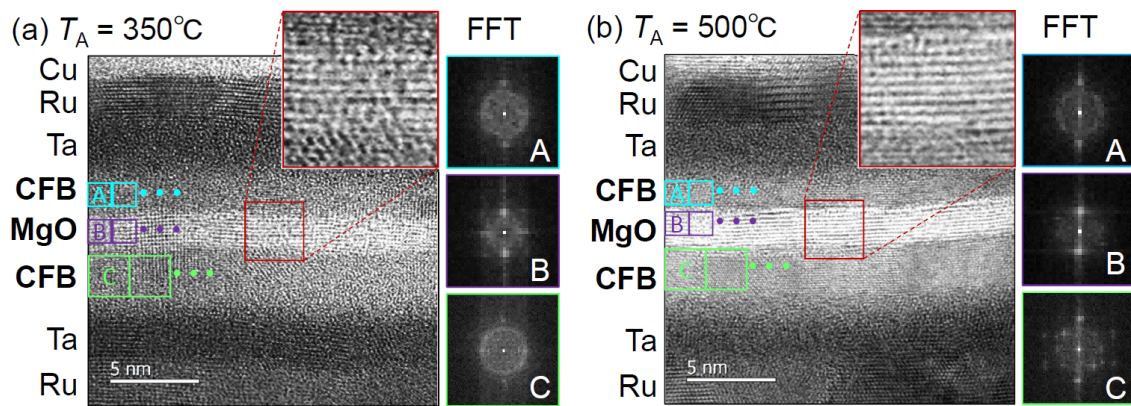
Figure 5.10: Bright-field scanning transmission electron microscope (STEM) images for the flexible sample annealed at (a) 350°C and (b) and 500°C. Panels A, B, and C show the two dimensional fast Fourier transform (FFT) images of the upper CFB, MgO, and lower CFB layers, respectively. The square areas in the STEM images indicated as A, B and C were used to perform the FFT, which was averaged by the FFT images for the multiple areas. The enlarged STEM images around the MgO layers are shown as insets. The figures are taken from Ref. [105].

for T_A = 500°C, which can be seen in a whole region. These results confirm that a property

suitable for the spin coherent tunneling is realized on the flexible substrate.

5.3 Strain effect

5.3.1 Strain effect on magnetoresistance curve

Figures 5.11 (a) and 5.12 (a) show changes of the magnetoresistance (MR) curves with strain ε_x application to a flexible MTJ sample under magnetic fields parallel (H_x) and perpendicular (H_y) to ε_x. The layer structure of the sample used here was Ta(1.7 nm)/Ru(3.1 nm)/Ta(1.9 nm)/CFB(2.7 nm)/MgO(3.3 nm)/CFB(4.3 nm)/Ta(2.2 nm)/Ru(1.8 nm) from the substrate side and the sample was annealed at T_A = 350°C. The pillar shape was ellipse with 16.5-μm-major-axis and 8.5-μm-minor-axis. Increases in the coercivities are clearly seen as ε_x
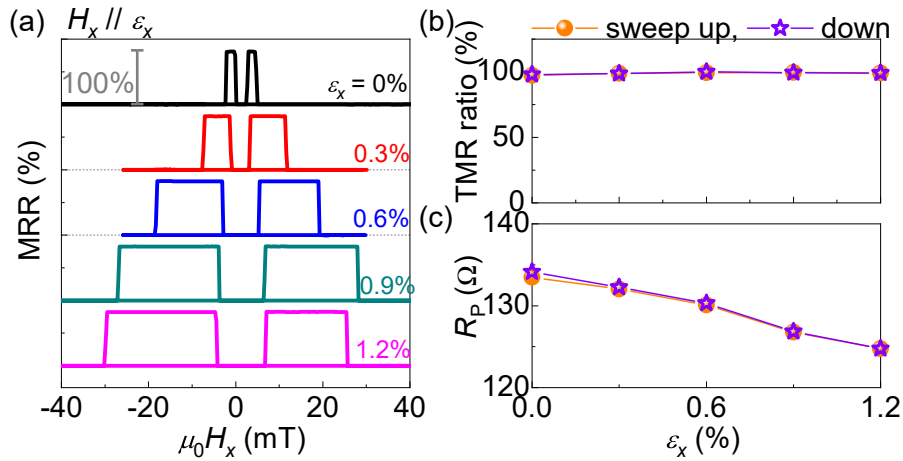
Figure 5.11: (a) The MR curves measured under various strain ε_x. The magnetic field H_x is parallel to the stretched direction. Dependence of (b) the TMR ratio and (c) a resistance with the parallel magnetization state (R_P) on ε_x. The figures are taken from Ref. [106].

increases, indicating the CFB layers have positive magnetoelastic constants B_{eff}. Here, the TMR ratio is almost independent of ε_x, and maintains the value after the sweeping up and down of ε_x as shown in Fig. 5.11 (b). Figure 5.11 (c) shows that the resistance with the parallel (P) magnetization state (R_P) reversibly decreases with the ε_x application. This probably reflects the increase in the tunneling electrons with the MgO thickness reduction caused by the in-plane tensile strain ε_x. Since the tunnel resistance R_t is exponential to the barrier thickness t ($R_t \propto e^{at}$, where a is a constant), the resistance change ratio $\Delta R_t / R_t$ with

the Poisson's compression becomes

$$\Delta R_t / R_t = e^{-a\nu\varepsilon_x t} - 1, \tag{5.2}$$

where ν is the Poisson's ratio. Therefor, this effect is suppressed if the MgO tunnel barrier is thinner.

For the quantitative discussion of the magnetic anisotropy, MR curves under H_y were analyzed [Fig. 5.12 (a) shows an example for $\varepsilon_x = 0.6\%$]. At first, the magnetizations of both
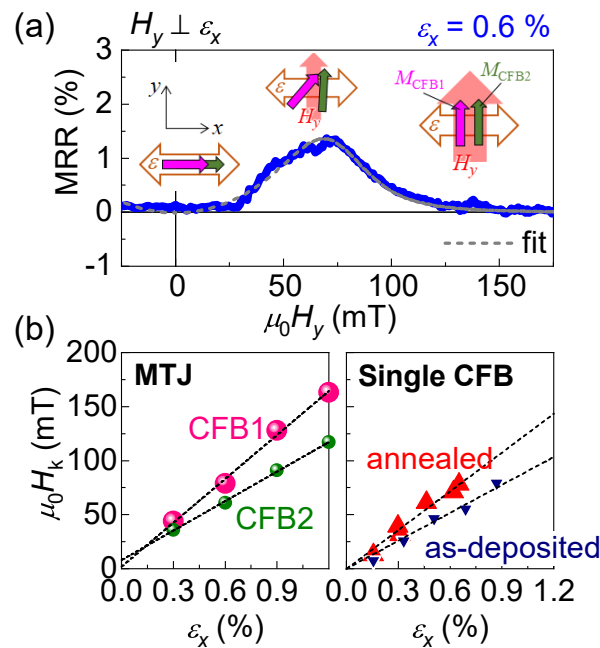
Figure 5.12: (a) An MR curve measured under a strain $\varepsilon_x = 0.6\%$. Direction of the magnetic field H_y is perpendicular to the tensile strain direction and swept from positive to negative field. The fitting curve is indicated by a dashed line. The magnetization directions for CFB1 and CFB2 layers at three situations are indicated by arrows. (b) The ε_x dependence of anisotropy fields H_k for CFB1 and CFB2 layers in the MTJ (left panel) and for the as-deposited and annealed samples with a single CFB layer (right panel). The figures are taken from Ref. [106].

CFB layers align in y direction under high H_y, and thus the resistance is low. By reducing H_y, the resistance increases as the magnetization of one CFB layer with a stronger magnetic anisotropy (denoted as CFB1) starts to direct x direction due to the magnetic anisotropy created by ε_x. At $\mu_0 H_y = 0$ mT, the direction of the magnetization of CFB1 and that of the other layer (denoted as CFB2) becomes parallel along x axis due to the uniaxial anisotropy

induced by the strain, and thus the resistance again becomes low. As shown in Fig. 5.12 (a), the MR curve can be fitted well by the simulated curve. See section 4.2 for the detail of the simulation. Here, contribution from the anisotropic magnetoresistance (AMR) effect is not included. Anisotropy fields H_k for CFB1 and CFB2 were determined as best fit parameters for various ε_x, as plotted in Fig. 5.12 (b). The slope h_k of the linear fitting to the data for CFB1(2) is 135(91) mT per $\varepsilon_x = 1\%$.

On the other hand, Fig. 5.12 (c) shows H_k for a single CFB sample [Ta(1.7 nm)/Ru(3.1 nm)/Ta(1.9 nm)/CFB(4.3 nm)/MgO(3.3 nm)] determined using the AMR effect. See Sec. 3.1 for details of the AMR experiment. As-deposited and 350°C-annealed samples were prepared for the measurement. In the single CFB samples, the slope h_k for the annealed (as-deposited) sample is 127(93) mT per $\varepsilon_x = 1\%$. This B_{eff} increase by the annealing is qualitatively consistent with a previous report [107]. Since h_k of the CFB layers in the MTJ are comparable to that of the single CFB sample, the strain seems to be well transferred from the substrate to CFB layers in spite of the aluminum oxide surrounding the MTJ pillar. The CFB1 in the MTJ is supposed to be the lower CFB layer since its h_k is similar to that of the annealed single CFB, whose layer structure is the same except for the existence of the upper layers. The smaller h_k in the CFB2 (upper CFB layer) is attributed to the weaker crystallization of the upper CFB layer which can be, confirmed in Fig. 5.10 (a).

5.3.2 Strain sweeping

Here, resistance R changes with a continuous strain sweeping are discussed. Figure 5.13 shows the R change with ε_x sweeping under $\mu_0 H_y = 20$ mT for a sample annealed at 450°C for 3 hours. The layer structure is the same with that of the sample used in Sec. 5.2. The negative slope of the background is caused by the MgO thickness reduction with the Poisson effect (Eq. 5.2). Two magnetizations (M_1 and M_2) initially direct y direction under H_y and gradually change the direction toward x direction when ε_x increases due to the positive magnetoelastic effect in the CFB. A peak of R at around $\varepsilon_x = 0.8\%$ appears because the two magnetizations rotate slightly differently, and a small difference in magnetization angle is made. This suggests there are differences in h_k (i.e. B_{eff}) and/or the initial magnetic anisotropies between the two CFB layers. The angle difference of ~25° is supposed to arise

at the maximum, which is calculated using the R increase by ~40 Ω. This R-ε_x characteristic is quit different from those seen in Sec. 4.3 and shows a moderate resistance change ratio in spite of the large TMR ratio. This is because both magnetization layers are strain-sensitive, in contrast to the existence of a strain-insensitive layer in Sec. 4.3. One should make one of the magnetization layer strain-insensitive, maintaining the TMR ratio as high as possible to obtain a large R change or the strain direction sensing characteristic.
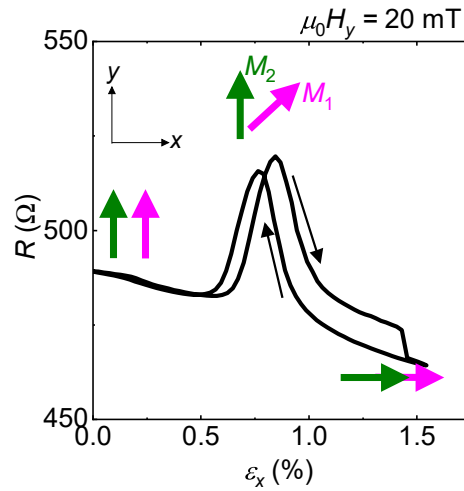
Figure 5.13: Change in resistance R while sweeping the strain ε_x under a constant magnetic field H_y. The thick arrows denote the magnetization directions M_1 and M_2 for the lower and upper CFB layers, respectively. An MTJ sample annealed at 450°C for 3 hours is used here. The figure is taken from Ref. [105].

However, a large R change is unexpectedly observed when the strain application is started from an anti-parallel (AP) magnetization state as shown in Fig. 5.14. The AP state was firstly set by sweeping a small H_x in the magnetic easy axis direction (the minor axis direction of the elliptic pillar). With ε_y application under a small H_y, R drastically decreased implying the realization of P state. When ε_y is swept back, the AP state surprisingly appears again. The abrupt R change around $\varepsilon_y = 0.5\%$ correspond to a large Gauge factor of ~1000. Because of the large R change of the full TMR ratio (~200%), the background R reduction is negligible this case.
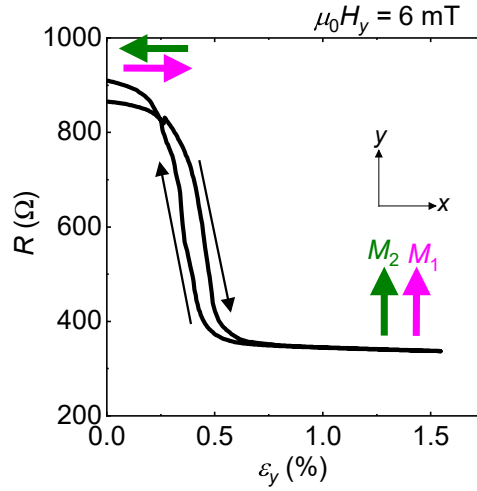
Figure 5.14: Change in resistance R while sweeping the strain ε_y under a constant magnetic field H_y. The measurement was started after an anti-parallel (AP) state was set by sweeping H_x. The thick arrows denote the magnetization directions M_1 and M_2 for the lower and upper CFB layers, respectively. An MTJ sample annealed at 500°C is used here.

5.3.3 Durability

So far, it has been confirmed that the flexible MTJ is not broken with a cycle of the over-1%-strain application. Here, sample's endurance against multiple cycles of the strain application was checked. The sample and condition of the strain application for a cycle were the same as those in Fig. 5.13. Figure 5.15 (a) shows strain cycle number N dependence of R_P and the TMR ratio. The MR curves were measured at $\varepsilon_x = 0\%$ before and after every 100 cycles. Figure 5.15 (b) shows MR curves for $N = 500$ and $N = 1000$. The results show that the
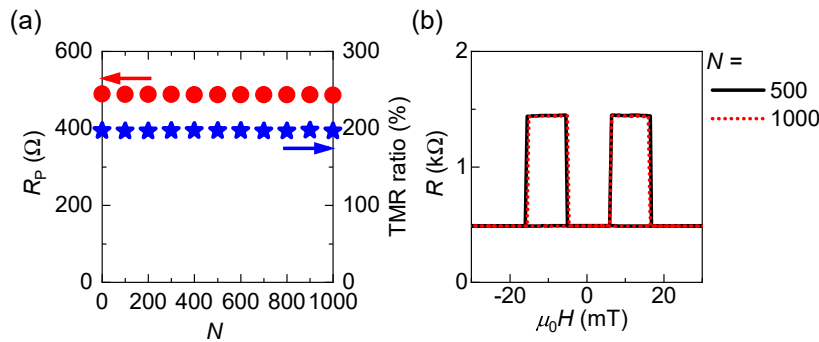
Figure 5.15: (a) Resistance at P state (R_P) and TMR ratio dependence on strain cycle number N. (b) Magnetoresistance curves after $N = 500, 1000$. The figures are taken from Ref. [105].

flexible MTJ is not degraded by 1000 times of strain (of 1.6% at the maximum) applications. Although R_{P} and the coercivities decrease slightly, which is hardly seen in Fig. 5.15, the changes decay and the MTJ characteristics settle as N increases.

5.4 Perspectives of magnetoelastic strain sensor

So far, it has been demonstrated that the TMR effect can be used for the flexible magnetoelastic strain sensors as well as the GMR effect. In order to clarify the features of our magnetoelastic strain sensors (including the GMR based sensors in Chap. 4), strain sensors based on other mechanisms are referenced and compared with the magnetoelastic sensors in Sec. 5.4.1. As for future perspectives, designs of other strain sensing characteristics using the magnetoelastic effect are shown in Sec. 5.4.2.

5.4.1 Comparison with other strain sensors

At first, commercially available metal and semiconductor strain gauges are introduced [108]. The most commonly used metal strain gauges consist of plastic carrier and zigzag metal wire or foil as schematically shown in Fig. 5.16. The zigzag structure is usually formed
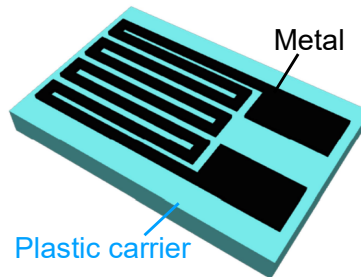
Figure 5.16: A schematic of a metal strain gauge.

in one direction to measure a strain in the longitudinal direction most sensitively. Note that three strain gauges are needed to determine the direction of the applied strain and the zigzag structure limits miniaturization of the sensors. The metal strain gauge reflects the applied strain as resistance R. Since R is written as $R = \rho l/(wt)$, where ρ, l, w and t are resistivity, length, width and thickness, respectively, one can derive

$$\frac{\Delta R}{R} = \frac{\Delta l}{l} - \frac{\Delta w}{w} - \frac{\Delta t}{t} + \frac{\Delta \rho}{\rho}. \tag{5.3}$$

Using the Poisson's ratio v, where $\Delta w/w = -v\Delta l/l$ and $\Delta t/t = -v\Delta l/l$, the gauge factor GF $\equiv (\Delta R/R)/\varepsilon = (\Delta R/R)/(\Delta l/l)$ is written as

$$\text{GF} = (1 + 2v) + \frac{\Delta\rho/\rho}{\Delta l/l}. \tag{5.4}$$

Here, the actual GF of most metal strain gauges is around 2, almost independent of the metal material [108]. In contrast, semiconductor strain gauges show a higher sensitivity ($|\text{GF}| = 10$-200) [108]. Change in R of the semiconductor strain gauges (usually single-crystals of doped Si or Ge) is caused by the band structural changes with strain applications. In exchange for the high GF, the semiconductor strain gauges require careful treatments to suppress the problems such as non-linearity or temperature dependence. In comparison to these conventional strain gauges, our magnetoelastic strain sensors have not only strong points of both types, e.g. a high GF and the temperature stability better than semiconductors, but also the higher stretchability ($\varepsilon \sim 2\%$), c.f. $\varepsilon \sim 0.2\%$ for the conventional strain gauges.

Secondly, flexible strain sensors in the process of research and development are introduced. Although there are many mechanisms used for flexible strain sensors such as optical back scattering in a fiber, Raman shift, Bragg grating, triboelectricity, and capacitance [109–113], here we mainly focus on resistive-type strain sensors with a relatively simple read-out system. Conductive part of the flexible resistive-type sensors are made of carbon nanotubes, graphene, or nanowires and silicone-based elastomers or rubbers are often used as supporting materials [114–122].

Figure 5.17: (a) A scanning electron microscope image of the surface of a strain sensor with Ag nanowires. (b) Resistance change ratio $\Delta R/R_0$ with a strain application to the strain sensor. The figures are taken from [118].

80

Stretchability of these sensors ranges in 1.5%-800%. The percolating network of conductive wires [e.g. Fig. 5.17 (a)] or particles helps the stretchability exceed 10% together with the highly elastic supporting materials, while sensors with a 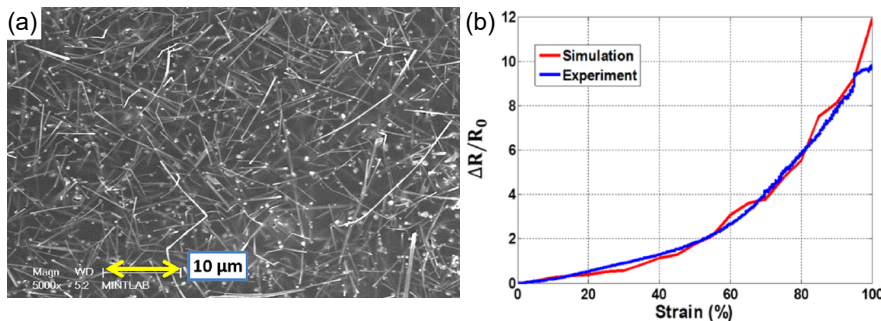single conductive component (including our magnetoelastic films) break with a relatively smaller strain. Comparing multiple reports, it seems difficult to establish both the high stretchability and the high GF. A high GF of 200-1200 (varies because of non-linearity) is achieved in the low-stretchable (~1.5%) sensor [114], while GF is lower (10-40) for the sensor with the record stretchability (~800%) [120]. The GF (~1000 in the strain range $\Delta\varepsilon \sim 0.1\%$) and the stretchability (~2%) of our TMR based magnetoelastic strain sensor range with those of the former sensor. A further highly sensitive (GF~4000) TMR based sensor with narrow stretchability (~0.1%) has also been reported [102]. Though increase in the stretchability of TMR based sensors may be possible somehow, the GF will be smaller with a relation GF $\propto$ MRR/$\Delta\varepsilon$ as long as the magnetoresistance ratio (MRR) in room temperature is limited (MRR $\leq$ 600% [98]).

One of the features of the magnetoelastic strain sensors is "decoupled strain and pressure sensing" [123] which is one of the challenges for most strain sensors. Since the resistivity, capacitance, and piezoelectricity can also be used for pressure sensors [124], the strain sensors are affected by a pressure, or compression in the thickness direction. In in-plane magnetized magnetoelastic strain sensors, effects of the pressure is negligible if the MRR is large. Thus it can prevent the erroneous detection of a compression as a stretch.

The strain direction sensing proposed in Sec. 4.3 is a unique feature making use of magnetism that has the information of direction. In conventional or above mentioned strain sensors, the strain direction can be determined only when three differently oriented strain sensors are read-out, while the magnetoelastic strain direction sensor determines the direction of a strain in the exactly single device with a single measurement of the resistance. This merit, together with the integration technology of the spintronics, will enable strain direction mapping. Although layered integration of differently oriented sensors [117, 125] will also enable the strain direction mapping, it requires more wires, impairing the integration and easy-handling.

In the semiconductor strain gauge and the flexible strain sensors, linearity is often low as shown in Fig. 5.17 (b). Although our magnetoelastic strain sensors shown so far also have

the non-linear strain sensing characteristic, an appropriate design of the magnetic property can enhance the linearity. The details are discussed in the following subsection.

5.4.2 Future designs of other magnetoelastic strain sensors

Here, multiple strain sensing characteristics are proposed apart from the strain direction sensing. Such a controlability of the characteristics is another feature of the magnetoelastic strain sensors.
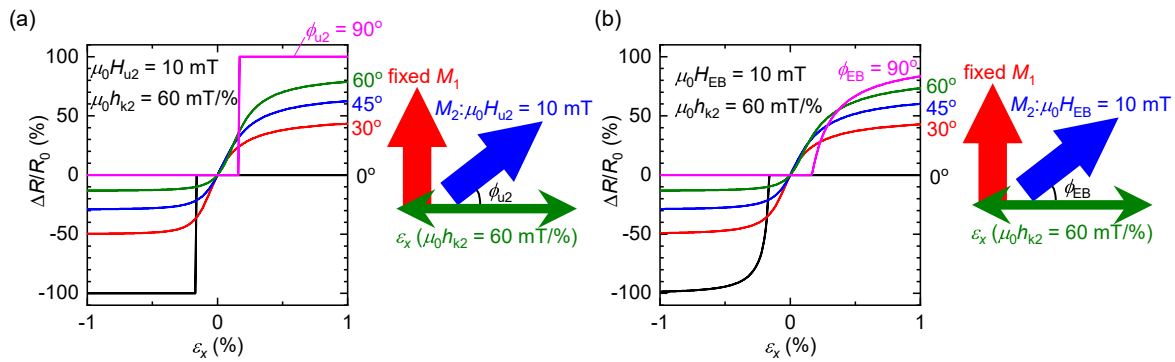
Figure 5.18: Simulated strain sensing characteristics for different (a) initial uniaxial anisotropy directions ϕ_{u2} and (b) exchange bias direction ϕ_{EB} with constant values of the initial uniaxial anisotropy $\mu_0 H_{u2} = 10$ mT and the exchange bias $\mu_0 H_{EB} = 10$ mT, respectively. Strain-insensitive M_1 is fixed while strain-sensitive M_2 obtains magnetic anisotropy as $H_{k2} = h_{k2}\varepsilon_x$, where ε_x and $\mu_0 h_{k2}$ (= 60 mT/%) are strain and magnetoelastic anisotropy field constant, respectively. A negative value of ε_x correspond to a compressive strain in x direction or a tensile strain in y direction. The magnetoresistance ratio of 200% is assumed.

Figure 5.18 (a) shows simulated strain sensing characteristics with different initial uniaxial anisotropy directions ϕ_{u2} in the strain-sensitive layer. Note that ϕ_{u2} has been fixed to be 0 in the simulations in Sec. 4.3. The oblique initial anisotrpy ($0° < \phi_{u2} < 90°$) results in nearly linear responses around $\varepsilon_x = 0\%$. Such a control of ϕ_{u2} can be realized by depositing magnetic films on a strained substrate [126, 127]. The similar control is also possible by inducing the exchange bias H_{EB} in different directions ϕ_{EB} as shown in Fig. 5.18 (b). This can be easily achieved by changing the magnetic field direction during the field cooling process. Although the exchange bias may also be used for fixing the strain-insensitive layer, it is possible to induce different exchange bias direction to each ferromagnetic layer by using two antifferomagnetic layers with different blocking temperatures [104].
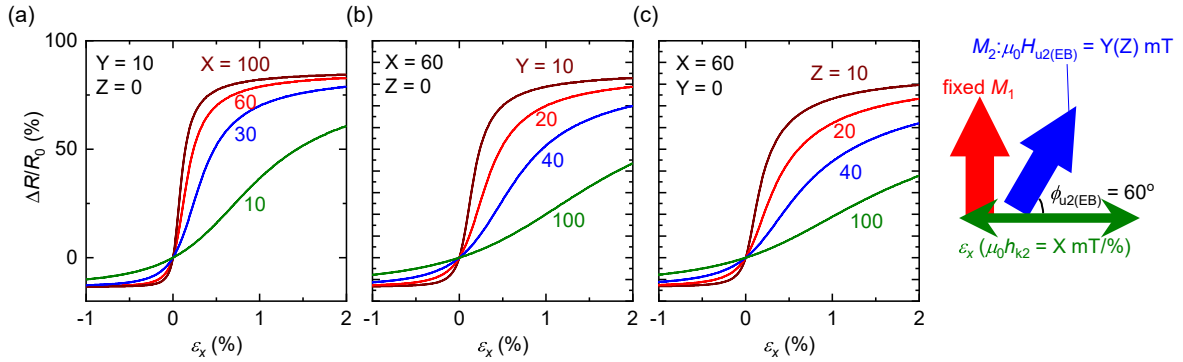
Figure 5.19: Simulated strain sensing characteristics for different (a) magnetoelastic anisotropy field constants h_{k2}, (b) initial uniaxial anisotropy field H_{u2} and (c) exchange bias field H_{EB} with 60° initial magnetization direction. The other conditions are same as those in Fig. 5.18.

The linear strain sensing range can be extended by reducing h_{k2}, increasing H_{u2} or increasing H_{EB}, in exchange for reduction of GF as shown in Figs. (a), (b) and (c) respectively. The adjustment of H_{u2} by changing the magnitude of the strain applied during the deposition [126, 127] seems to leave the most degree of freedom for the sensor design, though any of the adjustments are possible.

Such controls of the magnetic parameters can also lead to qualitatively different types of strain sensors. By setting initial magnetization directions perpendicular to each others using above methods, a full range strain direction sensing is possible as shown in Fig. 5.20 (a). The strain direction sensors in Sec. 4.3 have utilized only a half of the GMR ratio, since the
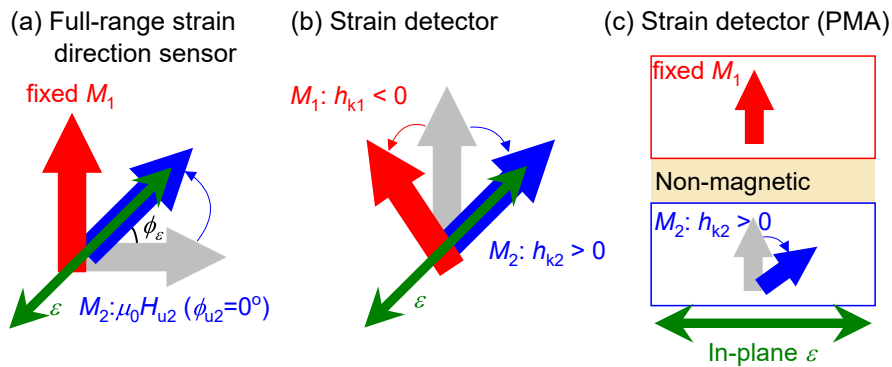
Figure 5.20: Designs for various types of magnetoelastic strain sensors.

sensor response is an even function against the strain direction ϕ_ε if the initial magnetizations are parallel. One the other hand, the initially perpendicular magnetization configuration not only uses the full GMR ratio but also detects the all strain direction (-90° < ϕ_ε < 90°).

Two types of strain detectors regardless of the strain direction are shown in Figs. 5.20 (b) and (c). Figure 5.20 (b) has two strain-sensitive layers with opposite signs of magnetoelastic constants (B_{eff} or h_{k}). The two magnetizations direct perpendicular to each others when a strain in any direction is applied. Ni can be used as the negative-strain-sensitive layer for example. The interlayer exchange coupling can force the magnetizations to be (anti-)parallel when no strain is applied.

Figure 5.20 (c) shows a schematic of a strain detector with perpendicular magnetic anisotropy (PMA). The two magnetic layers have different PMA and only one magnetization with a weaker PMA falls down to in-plane direction when an in-plane tensile strain (in any direction) is applied. The other layer keeps PMA as long as the strain is smaller than a threshold Eq. 4.5. The CFB/MgO-based MTJ will be suitable for this type of sensor because the PMA is obtained by thinning the CFB layer and its magnitude can be adjusted by the thickness or the annealing condition [99]. We have also confirmed that a CFB layer with PMA switches its magnetic easy axis into in-plane with a strain application (not shown). Although the capacitive-type sensors also isotropically detect an in-plane strain, the GF is usually low ~1 and they require a certain device area, which can be improved by the magnetoelastic strain sensors.

5.5 Summary of this chapter

In this chapter, the CoFeB(CFB)/MgO-based magnetic tunnel junctions (MTJs) have been fabricated on a flexible polyimide substrate. The tunnel magnetoresistance (TMR) ratio of ~200% has been obtained at annealing temperature of 450°C. Significant strain effects are also confirmed in the MTJs with a relatively complex pillar structure. A drastic resistance change with strain application (whose Gauge factor being ~1000) has been unexpectedly observed in spite of the absence of the strain-insensitive layer. This is due to a magnetization configuration switching between parallel and anti-parallel states, as well as the high TMR ratio. The strain durability test has also been conducted.

Different designs of magnetoelastic strain sensors have also been proposed. By adjusting the magnetic properties of the two ferromagnetic layers, linear responses with various sensitivities, full-range strain direction sensing or strain detecting can be realized.

In addition to the relatively high Gauge factors, the features unique to the magnetoelastic strain sensors have been discussed to be the controllability of strain sensing characteristic, the decoupled strain and pressure sensing, and strain direction sensing with less wires, which simplifies a strain direction mapping. Needs for an integrated small area strain mapping may fulfil the potential of the magnetoelastic strain sensors.

Chapter 6

Strain control of heat currnt generated by magneto thermoelectric effects

So far, combination of the inverse magnetostriction effect and the magnetoresistance effects, in other words coupling between the electric charge transport phenomena and a strain via the magnetoelastic effect, has been studied. In this chapter, coupling between heat transport phenomena and a strain is discussed. Section 6.1 briefly introduces the spin caloritronic or magneto-thermoelectronic effects. In Sec. 6.2, strain-induced 180° switching of a heat current in a Ni film on a sapphire substrate is demonstrated. In Sec. 6.3, 90° rotation and switching on/off of heat currents with strain application are demonstrated using a TbFeCo film on a flexible substrate. These provide novel methods for controlling thermal energy in electronic devices.

6.1 Magneto thermoelectric effects

6.1.1 Anomalous Ettingshausen effect and spin Peltier effect

Spin caloritronics has been triggered by an observation of the spin Seebeck effect [128] and attracts attention for future applications of energy harvesting or thermal managements [129]. Among the numerical spin-caloritronic and magneto-thermoelectric phenomena, the spin Peltier effect (SPE) [130–132] and the anomalous Ettingshausen effect (AEE) [133] may be

used for active thermal management in combination with the inverse magnetostriction effect. In these effects, the direction of a heat current $\boldsymbol{J}_q$ is determined by a magnetization $\boldsymbol{M}$.

In the AEE, which is the reciprocal effect of the anomalous Nernst effect [134], $\boldsymbol{J}_q$ generated by a charge current $\boldsymbol{J}_c$ follows the relation of

$$\boldsymbol{J}_q \propto \boldsymbol{J}_c \times \boldsymbol{M}, \tag{6.1}$$

indicating that the $\boldsymbol{J}_q$ direction can be rotated or reversed by changing the $\boldsymbol{M}$ direction [133]. In the SPE, which is the reciprocal effect of the spin Seebeck effect, a spin current in magnetic material induces $\boldsymbol{J}_q$ depending on the directions of the spin in the spin current and $\boldsymbol{M}$. Supposing a hetero-structure of a ferromagnetic layer and a non-magnetic layer with a large spin Hall angle [135], the spin current is excited by $\boldsymbol{J}_c$ and the resultant experimental relation of the SPE becomes the same as Eq. 6.1 as long as $\boldsymbol{M}$ directs in-plane [131]. Figure 6.1 shows schematics of $\boldsymbol{J}_q$ control with a strain via the AEE and/or SPE and the inverse magnetostriction effect.
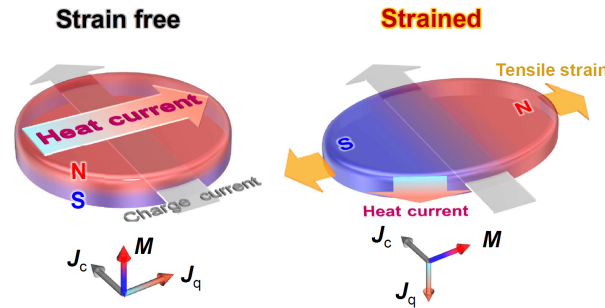
Figure 6.1: Schematics of the strain-induced heat control. $\boldsymbol{M}$, $\boldsymbol{J}_q$ and $\boldsymbol{J}_c$ are vectors of the magnetization, heat current and electric charge current, respectively. The figure is taken from Ref. [136].

6.1.2 Lock-in thermography

Temperature modulation caused by the AEE (and SPE)-induced $\boldsymbol{J}_q$ in samples was observed using the lock-in thermography (LIT) technique [131–133, 137–141] at room temperature, whose schematics are shown in Fig. 6.2. For the experiments in Secs. 6.2 and 6.3, magnetic films deposited on substrates were defined into Π-shaped wires with the width
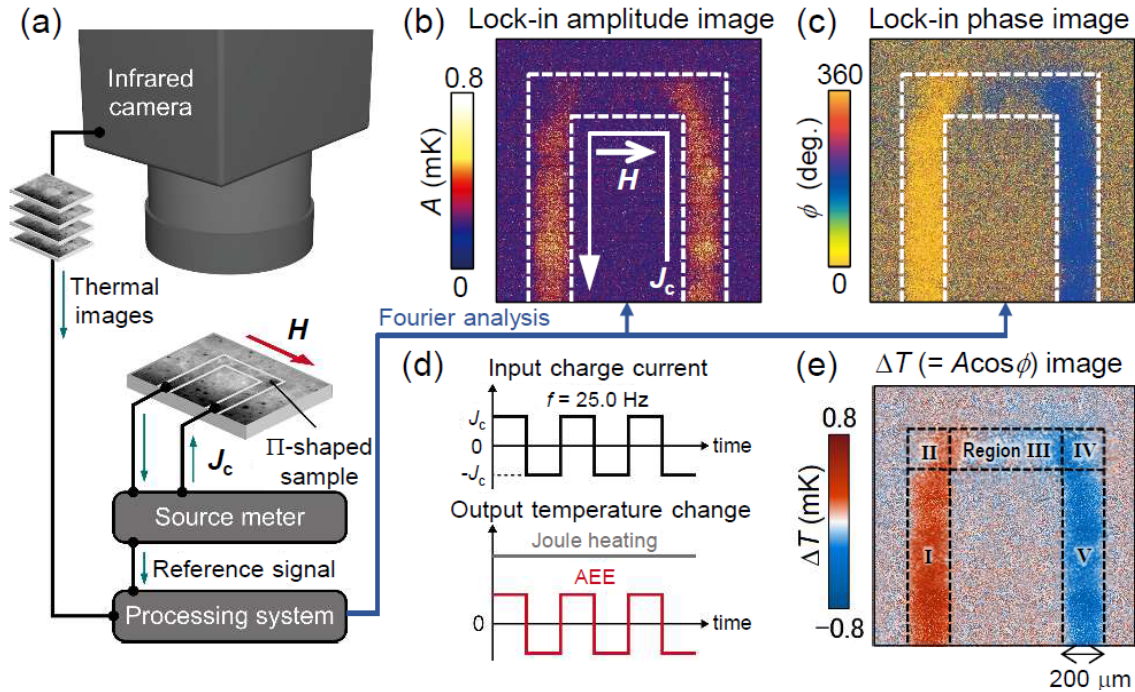
Figure 6.2: (a) A schematic of the lock-in thermography (LIT) measurement. Thermal images of (b) a lock-in amplitude A and (c) phase ϕ. A Π-shaped sample wire is in the area highlighted by the white dashed lines. (d) Schematic charts for the charge current input to the Π-shaped sample and the expected output thermal signals, i.e. time dependence of temperature changes generated by the Joule heating and the AEE (SPE). (e) $\Delta T (= A \cos \phi)$ image calculated from A and ϕ shown in (b) and (c), respectively. The thermal images shown here as examples were observed using a Ni sample in Sec. 6.2 at $\mu_0 H = +5.6$ mT without strain application. Definition of the regions I-V are shown by the black dashed lines in (e). The figures are taken from Ref. [136].

of 200-μm. The sample surface was coated with insulating black ink whose emissivity is >95% in order to enhance the infrared emissivity and ensure uniform emission properties. A rectangular alternating charge current with zero offset and a frequency f of 25 Hz was applied to the Π-shaped wire. While the Joule heating occurring with the alternating current is invariable because of the even function nature, the thermal responses caused by the AEE oscillate with f because the AEE is an odd function of $\boldsymbol{J}_c$ [see Fig. 6.2 (d)]. Therefore, an extraction of the first harmonic component of the temperature modulation with the Fourier analysis can eliminate the thermal contribution of the Joule heating, purely detecting the AEE. Therefor, the distributions of the lock-in amplitude A and phase ϕ of the AEE(SPE)-induced temperature modulation can be visualized by this LIT technique. The ϕ represents the sign of

the temperature modulation with respect to the sign of the input charge current as well as the time delay caused by the thermal diffusion. Figures. 6.2 (b) and (c) show typical examples of the A and ϕ images, respectively. Figure 6.2 (e) shows the conclusive ΔT $(= A \cos \phi)$ image. Here, ΔT is the temperature modulation including the sign information, if the thermal diffusion is negligible [139], which is the case of our experiments.

6.2   180° switching of heat current

Strain-induced control of the heat current switching field using an in-plane-magnetized Ni sample is demonstrated in this section. A Ni layer (15 nm) and a Pt cap layer (3 nm) were deposited in order with rf-sputtering on a c-plane sapphire substrate with the thickness of 100 μm. The Π-shape was formed by covering the substrate with a Π-shaped metal mask during the film deposition. An alternating charge current with the amplitude of 10 mA was input to obtain thermal images of the Ni sample under an in-plane magnetic field along the y axis (H_y) [see Fig. 6.3 (a) for the experimental configuration]. The field $\mu_0 H_y$ was reduced
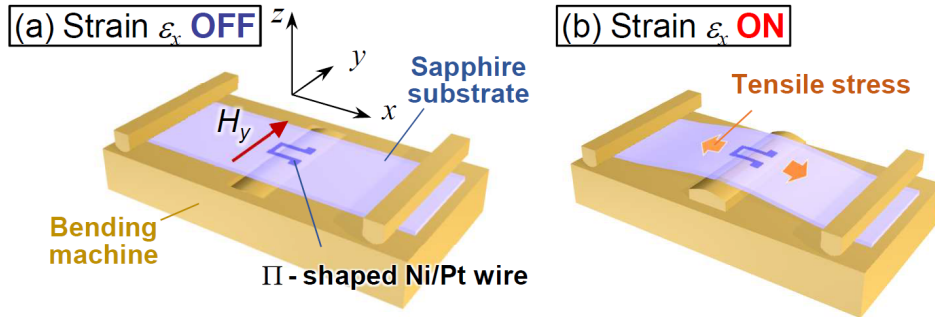
Figure 6.3: Schematics of the experimental setup for the cases (a) without strain and (b) with a strain. The figures are taken from Ref. [136].

from +5.6 mT to -5.5 mT, and the thermal images were taken with the LIT at each H_y. When the Ni sample is magnetized to the saturation in $+y$ direction with $\mu_0 H_y$ = +5.6 mT, the generation (positive ΔT) and absorption (negative ΔT) of heat at the sample surface on the regions I and V [see Fig 6.2 (e) for definition of the regions] are seen, respectively, as shown in the right panel in Fig. 6.4 (a). The $\boldsymbol{J}_q$ perpendicular to the film plane from the bottom side to the top side is generated according to Eq. 6.1, where $\boldsymbol{J}_c$ ($\boldsymbol{M}$) is along the $+x$ ($+y$) direction, and the heating of the sample surface is observed at the region I. The opposite situation except for the $\boldsymbol{M}$ direction happens at the region V. The thermal images are reversed under negative H_y, where $\boldsymbol{M}$ directs $-y$ direction. The switching occurs between $\mu_0 H_y$ = 0 mT and $\mu_0 H_y$ = -2.5 mT without strain (ε_x = 0%). In region III, $\boldsymbol{J}_c$ and $\boldsymbol{M}$ are expected to direct parallel to each other. Actually, the absolute value of ΔT for region III is much smaller than that for regions I and V, which is consistent with the symmetry of the AEE (Eq. 6.1). Note that the SPE also occurs at the same time and contributes to the ΔT because of the
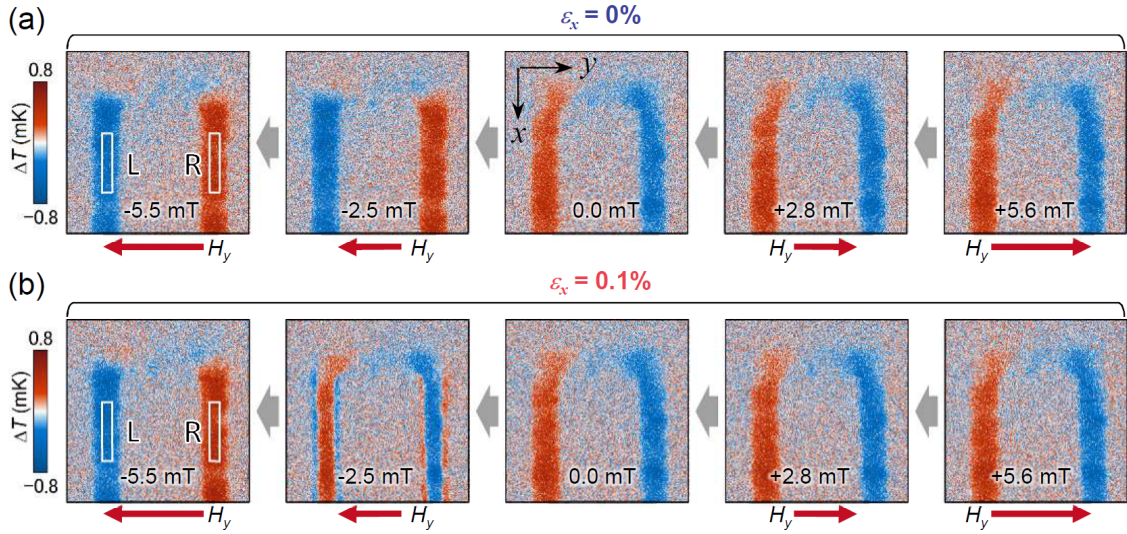
Figure 6.4: ΔT images for the cases (a) without bending ($\varepsilon_x = 0\%$) and (b) with bending ($\varepsilon_x = 0.1\%$). Areas indicated as L and R are the areas used for the numerical averaging for Fig. 6.5. The figures are taken from Ref. [136].

adjacent Pt layer.

A tensile strain ε_x was applied to the Ni sample along the x axis by bending the sapphire substrate using a three-point bending jig made of brass [see Fig. 6.3 (b)]. The strain at the sample surface ($\varepsilon_x = 0.1\%$) was calculated from the displacement of the sample center and the substrate thickness assuming arc-shaped deformation of the sapphire substrate. Since Ni has a negative magnetoelastic constant B_{eff} [54], the y axis becomes the magnetic easy axis when the substrate is bent in the present configuration. This magnetic anisotropy modulation leads to a coercivity increase. As a result, the negative field of $\mu_0 H_y = -5.5$ mT manages to completely switch the sign of ΔT under $\varepsilon_x = 0.1\%$ as can be seen in Fig. 6.4 (b). The direction of $\boldsymbol{J}_q$ between $\varepsilon_x = 0$ and 0.1% is opposite at $\mu_0 H_y = -2.5$ mT, which demonstrates that the strain application reverses the $\boldsymbol{J}_q$ direction by $180°$. It should be noted that $\boldsymbol{M}$ reversal only at the edge of the Π-shaped wire is seen at $\mu_0 H_y = -2.5$ mT and $\varepsilon_x = 0.1\%$, which is probably due to a weak magnetic anisotropy at the edges originated from the metal-mask-deposition. Figures 6.5 (a) and (b) summarize the behavior of ΔT as a function of $\mu_0 H_y$ for the $\varepsilon_x = 0$ and 0.1% cases, respectively. Here, the averaged ΔT values in areas L and R indicated in Figs. 6.4 (a) and (b) are plotted, where the error bars are the standard deviation. This clearly shows the enhancement in the switching field with the strain application.
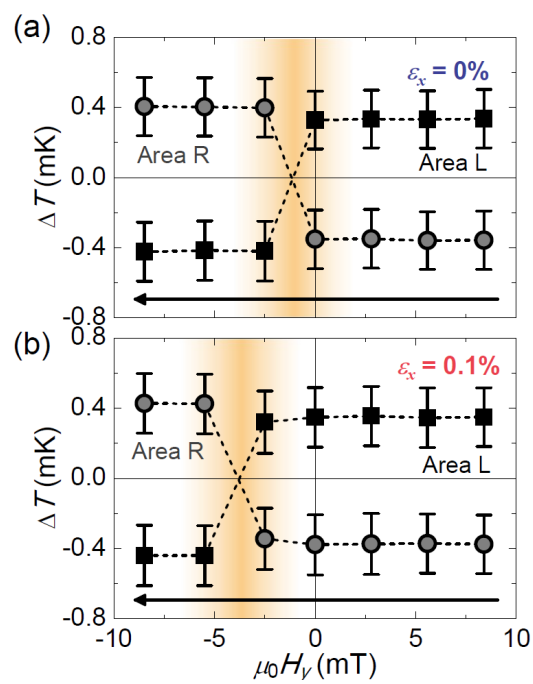
Figure 6.5: Averaged ΔT in areas L and R indicated in Fig 6.4 as a function of H_y for the cases of (a) $\varepsilon_x = 0\%$ and (b) $\varepsilon_x = 0.1\%$. The figures are taken from Ref. [136].

6.3　90° rotation of heat current

Strain-induced modulation of the heat current direction using a perpendicularly magnetized $Tb_{21}Fe_{67}Co_{12}$ (TFC) sample is demonstrated in this section. The layer structure of the TFC sample is Pt(4 nm)/TFC(6 nm)/Pt(4 nm) on a PEN substrate. The small tensile jig (see Fig. 2.6) was used to apply a strain ε_x as schematically shown in Fig. 6.6 (a). The TFC sample is known to switch its magnetic easy axis from perpendicular-to-plane to in-plane with a strain application [53]. Such a switching was confirmed by measuring the anomalous Hall resistance R_{Hall}, which is proportional to the perpendicular M component, under the perpendicular magnetic field H_z as shown in Fig. 6.6 (b). Although it is still unclear from Fig. 6.6 (b) which direction in in-plane the M directs at $\mu_0 H_z = 0$ with $\varepsilon_x > 0$, it was confirmed using the AMR effect that the magnetic easy axis is parallel to the tensile strain direction (x direction) when the strain ε_x is applied.
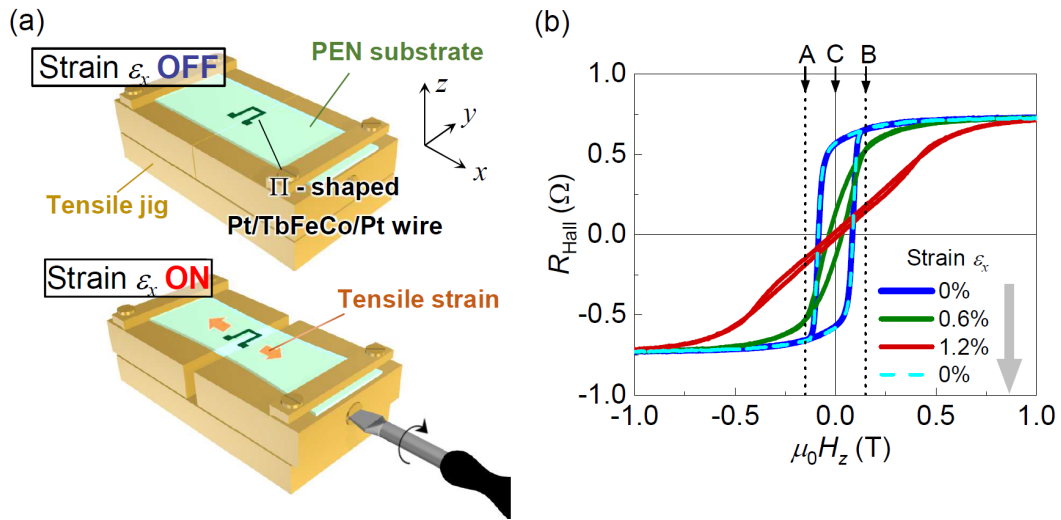
Figure 6.6: (a) Schematics of the experimental setup for the LIT measurement of the TFC sample. ε_x was applied using the small jig (Fig. 2.6). (b) Results of the anomalous Hall measurement with different in-plane tensile strain conditions of the TFC sample under magnetic field perpendicular to the film plane. R_{Hall} is a Hall resistance proportional to a perpendicular component of the magnetization. A, B and C indicate the field, at which the LIT measurements in Fig. 6.7 were performed. The figures are taken from Ref. [136].

Next, results of the LIT measurements using the Π-shaped TFC wire are shown. In the configuration for this experiment [Fig. 6.6 (a)], regions I and V are along the y axis. The ΔT images obtained under $\mu_0 H_z =$ (A) -0.15 T, (B) +0.15 T, and (C) 0.00 T for $\varepsilon_x =$
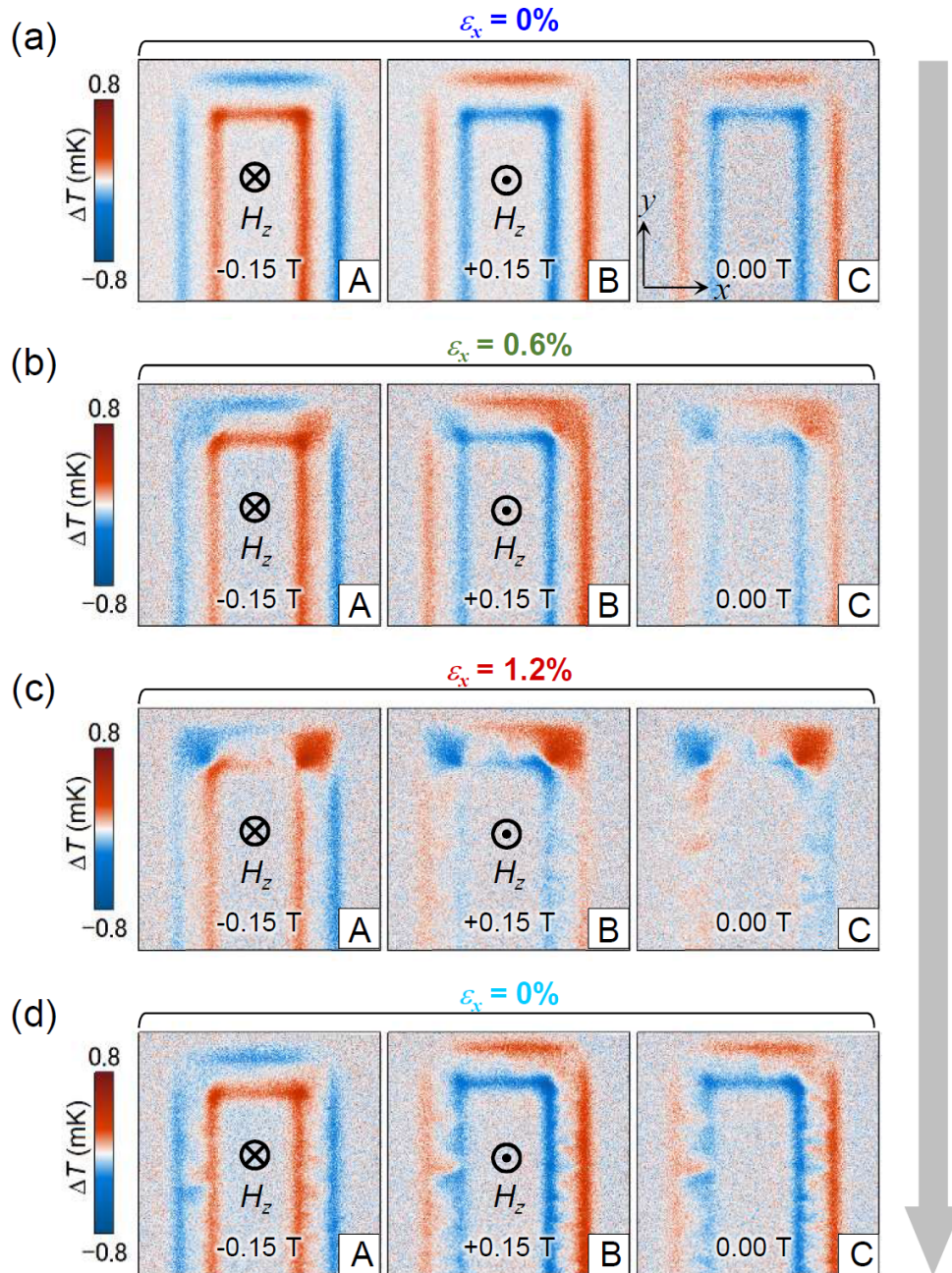
Figure 6.7: (a)-(d) ΔT images obtained under three different H_z conditions [dashed lines A-C in Fig. 6.6 (b) indicate the field] for $\varepsilon_x = 0$, 0.6, 1.2% and 0% for second time, respectively. The figures are taken from Ref. [136].

0, 0.6, 1.2% and 0% for the second time are respectively shown in Figs. 6.7 (a), (b), (c) and (d). An alternating charge current with the amplitude of 5 mA was input to obtain the thermal images of the TFC sample. H_z was applied in the order of A → B → C. In this experiment, background signals independent of the magnetic field were eliminated from the thermal images, where the background signals were calculated from the raw thermal images at $\mu_0 H_z = \pm 0.15$ T and $\varepsilon_x = 0\%$. The J_q generated by the AEE becomes parallel to the plane and perpendicular to the wire direction J_c since there is a perpendicular M component under any H_z at $\varepsilon_x = 0\%$. Actually, heat generation and absorption at the edges of the wire are seen in Fig. 6.7 (a), which is consistent with the AEE-induced signals for the perpendicularly magnetized case [133]. The areas of generation and absorption of the heat are switched for the cases A ($-$ 0.15 T) and B (+0.15 T) because of the opposite M directions. For the case C (0.00 T), the thermal image is qualitatively similar to that for the case B (+0.15 T) because there is negative component in the remanent M.

The perpendicular magnetic anisotropy of the sample is reduced when ε_x is increased, as shown in Fig. 6.6 (b) (see the curve for $\varepsilon_x = 1.2\%$), and M directs toward the in-plane (x) direction under low H_z. Here, the amplitude of ΔT at the wire edges for the case C (0.00 T) decreases in response to this behavior, as can be seen in the images in Figs. 6.7 (b) and (c). An important point is that the ΔT signals at the wire edges disappeared at $\varepsilon_x = 1.2\%$ C, indicating that the J_q in in-plane direction is eliminated. It is noted that the ΔT signals at regions I (heat generation) and V (heat absorption) under $\varepsilon_x = 1.2\%$ are similar to those in the case of the in-plane magnetized Ni sample (Fig. 6.4). This suggests that the 90° rotation of J_q from the in-plane (x) direction to the perpendicular (z) direction occurs as a result of M switching from the perpendicular to in-plane (x) with the ε_x application. Although a patchy pattern is seen in regions I and V of Fig. 6.7 (c) C, which reflects random M orientations, the sign of ΔT indicates that most of M directs the +x direction, which is likely caused by a small tilt of H_z. The thermal images at $\varepsilon_x = 0\%$ for the second time [Fig. 6.7 (d)] again show the signals similar to those for the perpendicularly magnetized situation, confirming an almost reversible change. However, the patchy pattern seen in Fig. 6.7 (c) seems to remain also in Fig. 6.7 (d), which is probably caused by degradation of the perpendicular magnetic anisotropy with the long-time stretching and heating for the LIT measurements. As for the

SPE in the TFC sample, the contribution is supposed to be small because of the cancellation of spin currents from the two Pt layers. Particularly for perpendicularly magnetized case, the SPE do not occurs because of the symmetry of the SPE [131].

It should be kept in mind that ΔT is proportional to the length of the ferromagnetic material along the heat current [132], when discussing the magnitude of the ΔT in the TFC sample. Since the width of the TFC wire (200 μm) is larger by several orders of magnitude than the thickness (6 nm), the ΔT signals in the perpendicularly magnetized case can be orders of magnitude larger than those in the in-plane magnetized case. The difference in the ΔT magnitude between these cases is, however, not so large, as shown in Fig. 6.7 (c). The following hypotheses may explain the situation.

1. Heat dissipates into the substrate or the black ink from the TFC layer and the resultant temperature modulation in the sample plane (perpendicularly magnetized case) is reduced [133]. A calculation of temperature modulation for the perpendicularly magnetized case using the finite element method is shown in Fig. 6.8, where the ΔT normalized by that for the case without heat dissipation is on the order of 10^{-3}.

2. The dependence of the temperature modulation on the lock-in frequency f differs between the two cases [141], where the magnitude of the ΔT in the perpendicularly magnetized case is smaller for higher f, and on the other hand, that is almost independent of f in the in-plane magnetized case (note that the present LIT measurements were performed at a high f value of 25 Hz).

In consideration of previous studies [133, 141] and Fig. 6.8, the first hypothesis seems to be the dominant reason.

The comparison between the ΔT of the Ni and TFC samples in the in-plane magnetized case is another point to be discussed. The magnitude of ΔT at regions I and V for the TFC sample [Fig. 6.7 (c) C] is much smaller than that for the Ni sample (Fig. 6.4). This result may be explained by the smaller amplitude of the input current, the thinner magnetic layer (a shorter length for the heat current accumulation [132]), the multi-domain state, the cancellation of the SPE and the smaller coefficients for AEE in the TFC sample.

The ΔT signals at regions II and IV, which are clearly seen in the TFC sample with
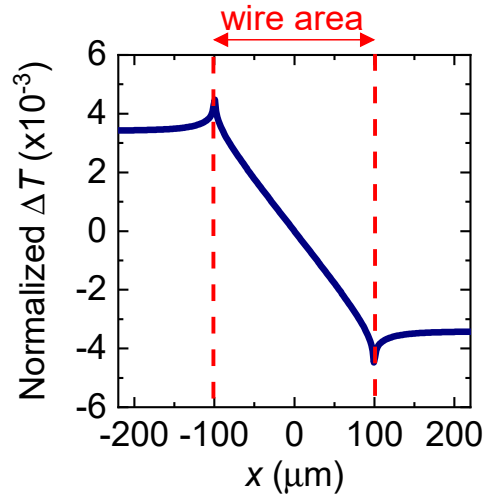
Figure 6.8: A result of the finite element method calculation for the distribution of temperature modulation ΔT assuming the heat dissipation into the black ink and the substrate for the perpendicularly magnetized (in-plane heat flow) case. The vertical axis is normalized by the expected value for an isolated sample system. The 14-nm-thick TFC sample wire was assumed to reside in $-100\ \mu\mathrm{m} < x < 100\ \mu\mathrm{m}$ and thickness of the PEN substrate and black ink were assumed to be 50 and 10 μm, respectively. The thermal conductivity of the sample wire, PEN substrate and black ink were set to be 10, 0.3 and 0.5 W/m/K, respectively. The calculation was performed by Dr. Ryo Iguchi.

strains ($\varepsilon_x > 0\%$), are also mentioned. These are consistent with signals from the anisotropic magneto-Peltier effect (AMPE) if the sign of the AMPE-coefficient of the TFC is opposite to that of the bulk Ni [140] and M aligns along the $\pm x$ direction. Although the AMPE can also occur in the Ni sample, ΔT at regions II and IV is not apparent (Fig. 6.4) probably because the high thermal conductivity of the sapphire substrate reduces ΔT signals induced by the AMPE, while the AEE-induced ΔT for the in-plane magnetized case are almost independent of the thermal conductivity of the substrate [141].

6.4 Summary of this chapter

In this chapter, combination of the magneto-thermoelectric effects and the inverse magnetostriction effect has been studied. In other words, the thermal transport phenomena have been controlled by applying a strain. In the Ni sample on a sapphire substrate, a switching field of the heat current generated by the anomalous Ettingshausen effect (AEE) has been changed by bending the substrate. This suggests that the heat current direction can be switched 180° by applying a strain. In the TbFeCo sample on a flexible substrate, the direction of the heat current generated by the AEE has been rotated 90° from in-plane to perpendicular-to-plane due to the magnetization rotation from perpendicular-to-plane to in-plane. At the same time, additional signals from the anisotropic magneto-Peltier effect (AMPE) have appeared. The observation of the AMPE signals has become possible thanks to the low thermal conductance of the flexible substrate.

These heat current control may be useful for thermal management in increasingly complex electronic and spintronic circuits. It will be important to find a material that has both the high magneto-thermoelectric coefficients and the effective magnetoelastic constant for a further efficient thermal management.

Chapter 7

Summary

7.1 Conclusion

In this thesis, strain effects on flexible spintronic devices have been investigated. In contrast to the conventional flexible spintronic devices that should be invariant with the strain, mechanical functions using the inverse magnetostriction effect have been discussed. On a flexible substrate, the clear inverse magnetostriction effect is easily observed due to a large strain. Such an inverse magnetostriction effect are combined with spintronics effects to realize new functions.

Inverse magnetostriction effect on single magnetic layer

In Chap. 3, before combining with the spintronics effects, the basic inverse magnetostriction effect in samples with a single Co magnetic layer has been studied. The effective magnetoelastic coupling constant of the Co sample largely depends on the layer structure. The thickness of the layers, material species of the layer adjacent to the Co layer and crystalline structures are the factor that determines the magnitude and even the sign of the inverse magnetostriction effect of the Co thin films. These findings are not only scientifically interesting, but also useful for designing the flexible spintronic devices.

The extended X-ray absorption fine structure (EXAFS) spectroscopy has also revealed that the strain in the flexible substrate is not perfectly transferred to the magnetic layer. And furthermore, the degree of the strain-transfer depends on the layer structure of the sample.

Similar investigations on other sample structures will give better understandings about the strain-transfer, contributing to a field of flexible electronics as well as the flexible spintronics.

Combination with giant magnetoresistance effect

In Chap. 4, the giant magnetoresistance effect has been combined with the inverse magnetostriction effect. Methods for analyzing peculiar magnetoresistance curves that appear with strain applications have been discussed based on the coherent magnetization rotation model. The model has appeared to be useful also for discussing the resistance change with a continuous strain application. By optimizing the layer structure, i.e. making one magnetic layer strain-insensitive and the other strain-sensitive, a new type of strain sensor, the strain direction sensor has been demonstrated. In addition, the performance of the strain direction sensor has become better by introducing the exchange bias. A higher sensitivity and the usability without an external magnetic field have enabled the practical human motion sensing. The sensor identifies the finger bent only from a single resistance measurement.

Combination with tunnel magnetoresistance effect

In Chap. 5, fabrication of the magnetic tunnel junctions (MTJs) on a flexible substrate has been explored, in order to enhance the magnetoresistance ratio. With annealing at 450°C, the CoFeB/MgO-based MTJ on a flexible polyimide substrate has showed a high magnetoresistance ratio of ~200%. Contrary to the expectation that the resistance change would be small if two magnetic layers are strain-sensitive, the flexible MTJ has showed a large Gauge factor (~1000) as a result of the magnetization configuration switching from anti-parallel to parallel.

Characteristics of the magnetoelastic strain sensors in comparison with other flexible strain sensors are discussed to be high Gauge factors, the decoupled strain and pressure sensing, controllability of strain sensing characteristic, and strain direction sensing with less wires. Designs for different strain sensing characteristics such as linear response or strain detection independent of the strain direction are also proposed.

Combination with magneto-thermoelectric effects

In Chap. 6, heat transport phenomena have been controlled by a strain, in contrast to the control of electric charge transport phenomena in other chapters. The heat current generated by the anomalous Ettingshausen effect depends on the electric current and the magnetization. The magnetization control by a strain direction can change the configuration resulting into the heat current controls with strain. The demonstration of the novel heat control mechanism will stimulate researches of physics and material science and contribute to thermal energy engineering in nanoscale devices.

7.2   Future research directions

For the improvement in characteristics of the flexible spintronic devices, the effective magnetoelastic coupling constants B_{eff} should be researched for many kinds of layer structures. Even for the Co thin films studied in Chap. 3, there still remains a plenty of room because the combinations with non-magnetic materials are enormous. The physics that determines B_{eff} also needs to be investigated. The methods used in Chap. 3, including the EXAFS spectroscopy, will be useful. Searches for not only the strain-sensitive materials but also the strain-insensitive materials are important, since the strain-insensitive materials have been limited to NiFe, with which it is difficult to obtain a large tunnel magnetoresistance ratio.

Integration of the strain sensors is one of the directions expected. The strain direction mapping can be achieved more easily and densely using the strain direction sensors compared with other strain mapping techniques [117, 125]. It is also interesting to realize the other types of magnetoelastic strain sensors as discussed in Chap. 5. An expressive strain sensor sheet may be made by integrating the sensors of multiple types, whose outputs may be processed by the machine learning techniques developing these days. A magnetoelastic memory or a magnetoelastice nanomagnet logic circuit [142, 143] are also the candidates to be developed with the flexible spntronics. Realization of these devices adds non-volatility of information, which is a virtue of magnetism, to the above sensors and opens up possibilities of the flexible spintronic devices.

Appendix A

Magnetoelastic effect in oriented polycrystalline film

A.1 Fcc (111)

Thin films deposited by the sputtering often have oriented poly-crystalline, or textured, structures. Here relations between the magnetoelastic coupling constants B_1, B_2 for cubic single crystal and the effective magnetoelastic coupling constants are derived based on the discussion in Ref. [35].

An xyz rectangular coordinate system with the z axis normal to the film plane and a $\xi\eta\zeta$ rectangular coordinate system are assumed, where [100], [010], [001] directions of a crystal grain are respectively the ξ, η, ζ axes. In contrast to the Eq. 1.3, where the two coordinate systems are matched, here the [111] direction is set to be the z axis. To express the situation for example, the coordinate system is firstly rotated by -45° around the z axis and secondly by $-\beta$ around the y axis, where β is the angle between the [111] and [001] directions ($\sin\beta = \sqrt{2/3}$, $\cos\beta = \sqrt{1/3}$). An additional rotation by any angle φ around the z axis reflects the in-plane random crystalline orientation. See also Fig. A.1 for the
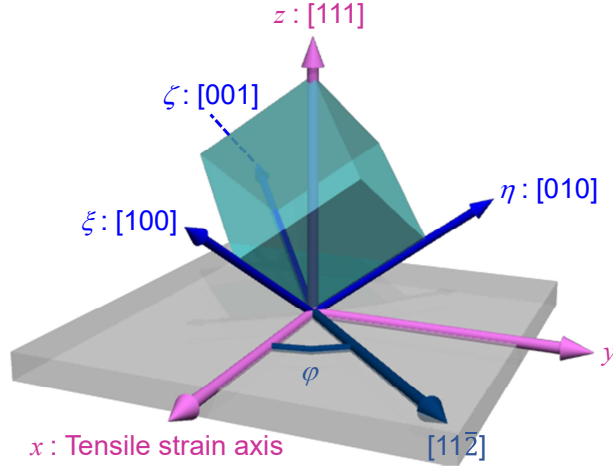
Figure A.1: Positional relation of the xyz and $\xi\eta\zeta$ coordinates.

configuration. The rotation matrixes $R_z^{-45°}$, $R_y^{-\beta}$, R_z^{φ} are expressed as

$$
R_z^{-45°} = \begin{pmatrix} 1/\sqrt{2} & 1/\sqrt{2} & 0 \\ -1/\sqrt{2} & 1/\sqrt{2} & 0 \\ 0 & 0 & 1 \end{pmatrix}, \quad R_y^{-\beta} = \begin{pmatrix} 1/\sqrt{3} & 0 & -\sqrt{2/3} \\ 0 & 1 & 0 \\ \sqrt{2/3} & 0 & 1/\sqrt{3} \end{pmatrix},
$$

$$
R_z^{\varphi} = \begin{pmatrix} \cos\varphi & -\sin\varphi & 0 \\ \sin\varphi & \cos\varphi & 0 \\ 0 & 0 & 1 \end{pmatrix}. \tag{A.1}
$$

Thus, the coordination transformation matrix T from the xyz to $\xi\eta\zeta$ systems is

$$
T = (R_z^{\varphi} R_y^{\beta} R_z^{45°})^{t} = \begin{pmatrix} \frac{\cos\varphi}{\sqrt{6}} + \frac{\sin\varphi}{\sqrt{2}} & -\frac{\cos\varphi}{\sqrt{2}} + \frac{\sin\varphi}{\sqrt{6}} & \frac{1}{\sqrt{3}} \\ \frac{\cos\varphi}{\sqrt{6}} - \frac{\sin\varphi}{\sqrt{2}} & \frac{\cos\varphi}{\sqrt{2}} + \frac{\sin\varphi}{\sqrt{6}} & \frac{1}{\sqrt{3}} \\ -\sqrt{\frac{2}{3}}\cos\varphi & -\sqrt{\frac{2}{3}}\sin\varphi & \frac{1}{\sqrt{3}} \end{pmatrix}. \tag{A.2}
$$

The strain tensor E in the xyz system (where diagonal components are ε_x, ε_y, ε_z and non-diagonal components are $\varepsilon_{xy} = \varepsilon_{yz} = \varepsilon_{zx} = 0$) is transformed to a new strain tensor E' in the $\xi\eta\zeta$ system as $E' = TET^t$. The magnetization direction cosines $\alpha = (\alpha_x \; \alpha_y \; \alpha_z)^t$ are also transformed as $\alpha' = T\alpha$.

If the magnetization direction is in the film plane, the direction cosines α in the xyz system can be expressed as $\alpha = (\cos\phi \ \sin\phi \ 0)^{\mathrm{t}}$. By substituting E' and α' into the original magnetoelastic coupling energy (Eq. 1.3) and organizing the expression, the target formula Eq. 1.11,

$$E_{\mathrm{magel}}^{xy} = \frac{B_1 + B_2}{3}(\varepsilon_x - \varepsilon_y)\cos^2\phi + \mathrm{const.}, \tag{A.3}$$

is obtained. Although the formula was obtained by averaging with respect to all the in-plane crystalline orientation φ in Ref. [35], this is already independent of φ, which means that the crystalline grains with different orientations obtain the same in-plane magnetic anisotropy with respect to the tensile strain direction, as long as [111] direction is perpendicular to the film plane.

In order to determine both B_1 and B_2 from experiments of the inverse magnetostriction effect, one needs another relational expression. For example, the magnetic anisotropy in xz plane should be obtained. One can derive

$$E_{\mathrm{magel}}^{xz} = \left[\frac{B_1}{6}(\varepsilon_x - \varepsilon_y) + \frac{B_2}{12}(5\varepsilon_x + \varepsilon_y - \varepsilon_z)\right]\cos^2\psi + \mathrm{const.}, \tag{A.4}$$

by assuming $\alpha = (\sin\psi \ 0 \ \cos\psi)^{\mathrm{t}}$. This case, the averaging with respect to φ is needed in contrast to the in-plane magnetization case.

A.2   Hcp (0001)

Bulk Co is known to have the hexagonal close packed (hcp) structure, whose magnetoelastic constants are obtained in literatures [144, 145]. Here, the effective magnetoelastic coupling constant B_{eff} of an hcp (0001) textured structure is derived to compare to B_{eff} of Co films obtained in Chap. 3, because the hcp (0001) structure is similar to the fcc (111) structure.

In hexagonal material, the magnetoelastic energy $E_{\mathrm{magel}}^{\mathrm{hex}}$ [33, 146] is expressed as

$$\begin{aligned} E_{\mathrm{magel}}^{\mathrm{hex}} &= B_1(\alpha_x^2 \varepsilon_{xx} + 2\alpha_x\alpha_y\varepsilon_{xy} + \alpha_y^2\varepsilon_{yy}) + B_2(1 - \alpha_z^2)\varepsilon_{zz} \\ &+ B_3(1 - \alpha_z^2)(\varepsilon_{xx} + \varepsilon_{yy}) + B_4(\alpha_y\alpha_z\varepsilon_{yz} + \alpha_x\alpha_z\varepsilon_{xz}), \end{aligned} \tag{A.5}$$

where the four magnetoelastic coupling constants B_1-B_4 are related to the elastic constants c_{ij} and four magnetostriction constants λ_A-λ_D as

$$
\begin{aligned}
B_1 &= -(c_{11} - c_{12})(\lambda_A - \lambda_B), \quad B_2 = -c_{13}(\lambda_A + \lambda_B) - c_{33}\lambda_C, \\
B_3 &= -c_{12}\lambda_A - c_{11}\lambda_B - c_{13}\lambda_C, \quad B_4 = c_{44}(\lambda_A + \lambda_B + \lambda_C - 4\lambda_D).
\end{aligned} \tag{A.6}
$$

In the hcp (0001) texture case, the coordination transformation matrix T is simply $(R_z^{\varphi})^t$. Assuming that magnetization direction is in-plane [$\alpha = (\cos\phi \ \sin\phi \ 0)^t$], the strain tensor and the magnetization direction cosines α are transformed to be

$$
\begin{aligned}
\varepsilon'_{xx} &= \varepsilon_x \cos^2\varphi + \varepsilon_y \sin^2\varphi, \quad \varepsilon'_{yy} = \varepsilon_x \sin^2\varphi + \varepsilon_y \cos^2\varphi, \\
\varepsilon'_{xz} &= \varepsilon'_{yz} = 0, \quad \varepsilon'_{xy} = -\varepsilon_x \sin\varphi \cos\varphi + \varepsilon_y \sin\varphi \cos\varphi,
\end{aligned} \tag{A.7}
$$

$$
\alpha'_x = \cos\varphi \cos\phi + \sin\varphi \sin\phi, \quad \alpha'_y = -\sin\varphi \cos\phi + \cos\varphi \sin\phi, \quad \alpha'_z = 0. \tag{A.8}
$$

Because of some zero components, only the first term in Eq. A.5 induces the magnetic anisotropy. The induced in-plane magnetic anisotropy is independent of the in-plane crystalline orientation φ, which is expressed as

$$
\begin{aligned}
E_{\text{magel}}^{\text{hex}-xy} &= B_1(\varepsilon_x - \varepsilon_y)\cos^2\phi \tag{A.9} \\
&= -(c_{11} - c_{12})(\lambda_A - \lambda_B)(1 + \nu)\varepsilon_x \cos^2\phi. \tag{A.10}
\end{aligned}
$$

With values $c_{11} = 307$ GPa, $c_{12} = 165$ GPa [33], $\lambda_A = -50 \times 10^{-6}, \lambda_B = -107 \times 10^{-6}$ [145] and Poisson's ratio $\nu = 0.4$, B_{eff} is calculated to be 11.3 MJ/m^3.

Appendix B

Average atomic distance change under uniaxial strain

A process of the calculation of atomic distance changes observed in the extended X-ray absorption fine structure (EXAFS) spectroscopy under a perfect strain-transfer case, whose results are shown in Tabs. 3.1 and 3.2, is explained here. Although the use of a polarized X-ray in the EXAFS enables direction-dependent measurement, it also acquires signals from the atoms at positions making an angle α with respect to the electric field E in the X-ray with weighting of $\cos^2 \alpha$ [65].

When a path between two atoms $\overrightarrow{OR} = (r \sin \theta \cos \phi, \ r \sin \theta \sin \phi, \ r \cos \theta)$ changes to $\overrightarrow{OR'} = (r \sin \theta \cos \phi (1 + \varepsilon_x), \ r \sin \theta \sin \phi (1 - \nu \varepsilon_x), \ r \cos \theta (1 - \nu \varepsilon_x))$ using polar coordinates parameters $(r, \ \theta, \ \phi$ with application of a tensile strain ε_x in x direction and compressive strains $-\nu \varepsilon_x$ in y and z directions with a Poisson's ratio ν, the atomic distance change ratio of the atom in the $(\theta, \ \phi)$ direction is

$$\frac{|\overrightarrow{OR'}|}{|\overrightarrow{OR}|} - 1 \approx \varepsilon_x [\sin^2 \theta (\cos^2 \phi - \nu \sin^2 \phi) - \nu \cos^2 \theta], \tag{B.1}$$

where higher orders of ε_x are excluded. For example, the atomic distance change ratio in $(\theta, \ \phi) = (\frac{\pi}{4}, \ 0)$ direction is calculated to be only 0.56% at $\varepsilon_x = 1.6\%$ if $\nu = 0.3$, indicating that the change ratio smaller than ε_x is reasonable even for the perfect strain-transfer case. Actually, paths are often in such directions in oriented polycrystalline structures.

In the following part, the above discussion is adapted to our experiment. Hereafter, all the calculation results assume $\varepsilon_x = 1.6\%$ and $\nu = 0.3$. For the case of the Fe sample, bcc (110) texture is firstly assumed. Calculations are based on structures that are at random in in-plane but complete in out-of-plane. Thus, in bcc (110) texture, a half of the nearest neighbor (NN) paths is expected to distribute at $\theta = \frac{\pi}{2}$ and the other half at $\theta = \arcsin\frac{1}{\sqrt{3}}$ for any ϕ. See Figs. B.1 (a) and (b) for visualization of the atomic positions. In case of the $\perp$ configuration, where

Figure B.1: (a) Distribution of the nearest neighbor (NN) and the second nearest neighbor (SN) atoms in one of the cases for the bcc (110) texture. (b) Distribution of the NN atoms in the bcc (110) texture considering the in-plane randomness.

the E direction corresponds to z direction ($\alpha = \theta$), the paths in $\theta = \frac{\pi}{2}$ have no contribution to the EXAFS signal because of the $\cos^2 \alpha$ weight, and therefore the atomic distance change ratio measured with EXAFS is calculated to be

$$\frac{1}{2\pi} \int_0^{2\pi} \left| \frac{|\overrightarrow{OR'}|}{|\overrightarrow{OR}|} - 1 \right|_{\theta=\arcsin\frac{1}{\sqrt{3}}} d\phi \approx -0.13\%. \tag{B.2}$$

In case of $\parallel$ configuration, where the E is in $(\theta, \phi) = (\frac{\pi}{2}, 0)$ direction, the atomic distance

change ratio is calculated as

$$\frac{1}{4}\frac{1}{2\pi}\int_0^{2\pi}\left|\frac{|\overrightarrow{OR'}|}{|\overrightarrow{OR}|}-1\right|_{\theta=\arcsin\frac{1}{\sqrt{3}}}2\cos^2\phi d\phi$$

$$+\frac{3}{4}\frac{1}{2\pi}\int_0^{2\pi}\left|\frac{|\overrightarrow{OR'}|}{|\overrightarrow{OR}|}-1\right|_{\theta=\frac{\pi}{2}}2\cos^2\phi d\phi\approx 0.82\%,\tag{B.3}$$

with a rough assumption that ϕ corresponds to α and the contribution from the paths in $\theta=\arcsin\frac{1}{\sqrt{3}}$ are a third weighted compared to those in $\theta=\frac{\pi}{2}$. Similarly, the calculations for second nearest neighbor (SN) atoms in bcc (110) texture, where four paths are at $\theta=\frac{\pi}{4}$, $\frac{3\pi}{4}$ and two are at $\theta=\frac{\pi}{2}$ [see SN in Fig. B.1 (a)], can be performed.

For calculations of bcc (001) texture, all of the NN paths are at $\theta=\frac{\pi}{4}$, $\frac{3\pi}{4}$, and two and four of the SN paths are at $\theta=0$, π and $\theta=\frac{\pi}{2}$, respectively. See Fig. B.2 (a) for this case.
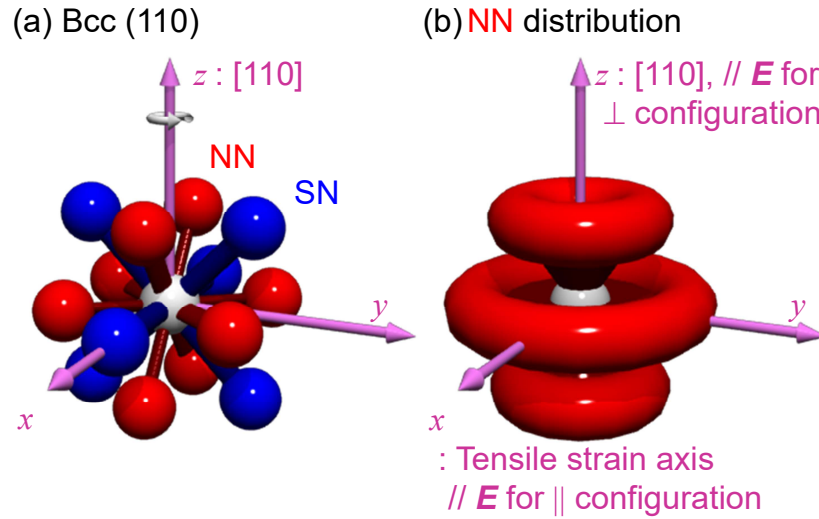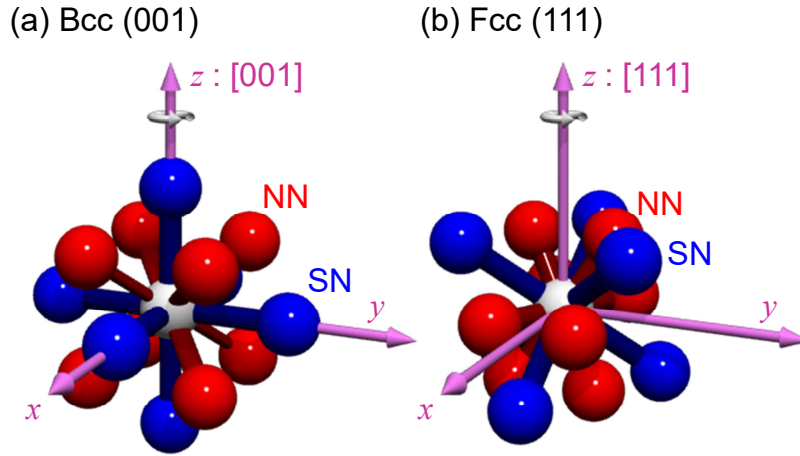

Figure B.2: Distributions of the nearest neighbor (NN) and the second nearest neighbor (SN) atoms in one of the cases for the bcc (001) texture (a) and fcc (111) texture.

In case of Co, though the Co sample includes hcp (0001) structure, calculations are performed using fcc (111) texture for simplicity because the NN paths in hcp and fcc are almost the same. The NN paths of fcc (111) texture are at $\theta=\arcsin\frac{1}{\sqrt{3}}$ and the other half at $\theta=\frac{\pi}{2}$, which leads to the same calculations as for bcc(110) [see Fig. B.2 (b)].

Bibliography

[1] Baibich, M. *et al.* Giant magnetoresistance of (001)Fe/(001)Cr magnetic superlattices. *Physical Review Letters* **61**, 2472–2475 (1988).

[2] Binasch, G., Grünberg, P., Saurenbach, F. & Zinn, W. Enhanced magnetoresistance in layered magnetic structures with antiferromagnetic interlayer exchange. *Physical Review B* **39**, 4828–4830 (1989).

[3] Huai, Y., Albert, F., Nguyen, P., Pakala, M. & Valet, T. Observation of spin-transfer switching in deep submicron-sized and low-resistance magnetic tunnel junctions. *Applied Physics Letters* **84**, 3118–3120 (2004).

[4] Miron, I. M. *et al.* Perpendicular switching of a single ferromagnetic layer induced by in-plane current injection. *Nature* **476**, 189–193 (2011).

[5] Liu, L. *et al.* Spin-Torque Switching with the Giant Spin Hall Effect of Tantalum. *Science* **336**, 555–558 (2012).

[6] Rogers, J. a., Someya, T. & Huang, Y. Materials and mechanics for stretchable electronics. *Science* **327**, 1603–1607 (2010).

[7] Keum, H., Mccormick, M., Liu, P., Zhang, Y.-w. & Omenetto, F. G. Epidermal Electronics. *Science* **333**, 838–843 (2011).

[8] Kaltenbrunner, M. *et al.* An ultra-lightweight design for imperceptible plastic electronics. *Nature* **499**, 458–463 (2013).

[9] Mohammed, M. G. & Kramer, R. All-Printed Flexible and Stretchable Electronics. *Advanced Materials* **29**, 1604965 (2017).

[10] Parkin, S. S. P., Roche, K. P. & Suzuki, T. Giant magnetoresistance in antiferromagnetic Co/Cu multilayers grown on kapton. *Japanese Journal of Applied Physics* **31**, L1246–L1249 (1992).

[11] Melzer, M. *et al.* Imperceptible magnetoelectronics. *Nature Communications* **6**, 6080 (2015).

[12] Parkin, S. S. P. Flexible giant magnetoresistance sensors. *Applied Physics Letters* **69**, 3092–3094 (1996).

[13] Yamamoto, S. *et al.* High coercivity ferrite thin-film tape media for perpendicular recording. *Journal of Magnetism and Magnetic Materials* **235**, 342–346 (2001).

[14] Chen, Y. F. *et al.* Towards flexible magnetoelectronics: Buffer-enhanced and mechanically tunable GMR of Co/Cu multilayers on plastic substrates. *Advanced Materials* **20**, 3224–3228 (2008).

[15] Barraud, C. *et al.* Magnetoresistance in magnetic tunnel junctions grown on flexible organic substrates. *Applied Physics Letters* **96**, 072502 (2010).

[16] Melzer, M. *et al.* Stretchable magnetoelectronics. *Nano Letters* **11**, 2522–2526 (2011).

[17] Donolato, M., Tollan, C., Porro, J. M., Berger, A. & Vavassori, P. Flexible and stretchable polymers with embedded magnetic nanostructures. *Advanced Materials* **25**, 623–629 (2013).

[18] Kirihara, A., Nakamura, Y., Yorozu, S., Uchida, K. & Saitoh, E. Thermoelectric converter element, method of manufacturing thermoelectronic converter element, and thermoelectric conversion method. *U.S. Patent 0312802 A1* (2013).

[19] Lin, G., Makarov, D., Melzer, M., Si, W. & Schmidt, O. G. Lab on a Chip analytic device. *Lab on a Chip* **14**, 4050–4058 (2014).

[20] Bedoya-Pinto, A., Donolato, M., Gobbi, M., Hueso, L. E. & Vavassori, P. Flexible spintronic devices on Kapton. *Applied Physics Letters* **104**, 062412 (2014).

[21] Pérez, N. *et al.* High-performance giant magnetoresistive sensorics on flexible Si membranes. *Applied Physics Letters* **106**, 153501 (2015).

[22] Lee, O., You, L., Jang, J., Subramanian, V. & Salahuddin, S. Flexible spin-orbit torque devices. *Applied Physics Letters* **107**, 252401 (2015).

[23] Karnaushenko, D. *et al.* High-Performance Magnetic Sensorics for Printable and Flexible Electronics. *Advanced Materials* **27**, 880–885 (2015).

[24] Tseng, P. *et al.* Flexible and Stretchable Micromagnet Arrays for Tunable Biointerfacing. *Advanced Materials* **27**, 1083–1089 (2015).

[25] Makarov, D., Melzer, M., Karnaushenko, D. & Schmidt, O. G. Shapeable magnetoelectronics. *Applied Physics Reviews* **3**, 011101 (2016).

[26] Loong, L. M. *et al.* Flexible MgO Barrier Magnetic Tunnel Junctions. *Advanced Materials* **28**, 4983–4990 (2016).

[27] Chen, J. Y., Lau, Y. C., Coey, J. M., Li, M. & Wang, J. P. High performance MgO-barrier magnetic tunnel junctions for flexible and wearable spintronic applications. *Scientific Reports* **7**, 42001 (2017).

[28] Qiao, X. *et al.* Enhanced stress-invariance of magnetization direction in magnetic thin films. *Applied Physics Letters* **111**, 132405 (2017).

[29] Sheng, P., Wang, B. & Li, R. Flexible magnetic thin films and devices. *Journal of Semiconductors* **39**, 011006 (2018).

[30] Yang, Q. *et al.* Ionic Gel Modulation of RKKY Interactions in Synthetic Anti-Ferromagnetic Nanostructures for Low Power Wearable Spintronic Devices. *Advanced Materials* **30**, 1800449 (2018).

[31] Serrano, I. G. *et al.* Two-Dimensional Flexible High Diffusive Spin Circuits. *Nano Letters* **19**, 666–673 (2019).

[32] Kittel, C. Physical theory of ferromagnetic domains. *Reviews of modern physics* **21**, 541–583 (1949).

[33] Sander, D. The correlation between mechanical stress and magnetic anisotropy in ultrathin films. *Reports on Progress in Physics* **62**, 809–858 (1999).

[34] Sander, D. *et al.* Stress , strain and magnetostriction in epitaxial films. *Journal of Physics: Condensed Matter* **14**, 4165–4176 (2002).

[35] Takahashi, H., Tsunashima, S., Iwata, S. & Uchiyama, S. Measurement of magnetostriction constants in (111)-oriented polycrystalline PdCo alloy and multilayered films. *Japanese Journal of Applied Physics* **32**, 1328–1331 (1993).

[36] Arai, K., Muranaka, C. & Yamaguchi, M. A new hybrid device using magnetostrictive amorphous films and piezoelectric substrates. *IEEE Transactions on Magnetics* **30**, 916–918 (1994).

[37] Kim, S. K. *et al.* Voltage control of a magnetization easy axis in piezoelectric/ ferromagnetic hybrid films. *Journal of Magnetism and Magnetic Materials* **267**, 127–132 (2003).

[38] Lee, J. W., Shin, S. C. & Kim, S. K. Spin engineering of CoPd alloy films via the inverse piezoelectric effect. *Applied Physics Letters* **82**, 2458–2460 (2003).

[39] Taniyama, T. *et al.* Electrical voltage manipulation of ferromagnetic microdomain structures in a ferromagnetic/ferroelectric hybrid structure. *Journal of Applied Physics* **101**, 09F512 (2007).

[40] Overby, M., Chernyshov, A., Rokhinson, L. P., Liu, X. & Furdyna, J. K. GaMnAs-based hybrid multiferroic memory device. *Applied Physics Letters* **92**, 192501 (2008).

[41] Rushforth, A. W. *et al.* Voltage control of magnetocrystalline anisotropy in ferromagnetic-semiconductor-piezoelectric hybrid structures. *Physical Review B* **78**, 085314 (2008).

[42] Weiler, M. *et al.* Voltage controlled inversion of magnetic anisotropy in a ferromagnetic thin film at room temperature. *New Journal of Physics* **11**, 013021 (2009).

[43] Geprägs, S., Brandlmaier, A., Opel, M., Gross, R. & Goennenwein, S. T. B. Electric field controlled manipulation of the magnetization in Ni/BaTiO₃ hybrid structures. *Applied Physics Letters* **96**, 142509 (2010).

[44] De Ranieri, E. *et al.* Piezoelectric control of the mobility of a domain wall driven by adiabatic and non-adiabatic torques. *Nature materials* **12**, 808–814 (2013).

[45] Shepley, P. M., Rushforth, A. W., Wang, M., Burnell, G. & Moore, T. A. Modification of perpendicular magnetic anisotropy and domain wall velocity in Pt / Co / Pt by voltage-induced strain. *Scientific Reports* **5**, 7921 (2015).

[46] Lei, N. *et al.* Strain-controlled magnetic domain wall propagation in hybrid piezoelectric/ferromagnetic structures. *Nature communications* **4**, 1378 (2013).

[47] Macionczyk, F., Brückner, W., Pitschke, W. & Reiss, G. Young's modulus and tensile strength of CuNi(Mn) thin films on polyimide foils by tensile testing. *Journal of Materials Research* **13**, 2852–2858 (1998).

[48] Macionczyk, F. & Brückner, W. Tensile testing of AlCu thin films on polyimide foils. *Journal of Applied Physics* **86**, 4922–4929 (1999).

[49] Yu, D. Y. W. & Spaepen, F. The yield strength of thin copper films on Kapton. *Journal of Applied Physics* **95**, 2991–2997 (2004).

[50] Fredriksson, P. & Gudmundson, P. Size-dependent yield strength of thin films. *International Journal of Plasticity* **21**, 1834–1854 (2005).

[51] Uhrmann, T. *et al.* Magnetostrictive GMR sensor on flexible polyimide substrates. *Journal of Magnetism and Magnetic Materials* **307**, 209–211 (2006).

[52] Chen, Y. F., McCord, J., Freudenberger, J., Kaltofen, R. & Schmidt, O. G. Effects of strain on magnetic and transport properties of Co films on plastic substrates. *Journal of Applied Physics* **105**, 07C302 (2009).

[53] Ota, S. *et al.* Strain-induced reversible modulation of the magnetic anisotropy in perpendicularly magnetized metals deposited on a flexible substrate. *Appl. Phys. Express* **9**, 043004 (2016).

[54] Asai, R. *et al.* Stress-induced large anisotropy field modulation in Ni films deposited on a flexible substrate. *Journal of Applied Physics* **120**, 063906 (2016).

[55] Ma, T., Bhushan, B., Murooka, H., Kobayashi, I. & Osawa, T. A novel technique to measure the Poisson's ratio and submicron lateral dimensional changes of ultrathin polymeric films. *Review of Scientific Instruments* **73**, 1813 (2002).

[56] Chikazumi, S. *Physics of Ferromagnetism (in Japanese)* (Shokabo, 1978).

[57] Ota, S., Ando, A. & Chiba, D. A flexible giant magnetoresistive device for sensing strain direction. *Nature Electronics* **1**, 124–129 (2018).

[58] Song, O., Ballentine, C. A. & O'Handley, R. C. Giant surface magnetostriction in polycrystalline Ni and NiFe films. *Applied Physics Letters* **64**, 2593–2595 (1994).

[59] Kawai, T., Ouchi, S., Ohtake, M. & Futamoto, M. Thickness effect on magnetostriction of Fe and $Fe_{98}B_2$ thin films. *IEEE Transactions on Magnetics* **48**, 1585–1588 (2012).

[60] Suzuki, M. *et al.* Depth profile of spin and orbital magnetic moments in a subnanometer Pt film on Co. *Physical Review B* **72**, 054430 (2005).

[61] Ota, T. *et al. Foundations and applications of XAFS (in Japanese)* (Kodansha, 2017).

[62] Ravel, B. & Newville, M. ATHENA, ARTEMIS, HEPHAESTUS: Data analysis for X-ray absorption spectroscopy using IFEFFIT. *Journal of Synchrotron Radiation* **12**, 537–541 (2005).

[63] Zabinsky, S., Rehr, J., Ankudinov, A., Albers, R. & Eller, M. Multiple-scattering calculations of x-ray-absorption spectra. *Phys. Rev. B* **52**, 2995–3009 (1995).

[64] Uruga, T. *et al.* The XAFS beamline BL01B1 at SPring-8. *Journal of Synchrotron Radiation* **6**, 143–145 (1999).

[65] Figueroa, A. I. *et al.* Strain in epitaxial MnSi films on Si(111) in the thick film limit studied by polarization-dependent extended x-ray absorption fine structure. *Physical Review B* **94**, 174107 (2016).

[66] Kyuno, K., Ha, J., Yamamoto, R. & Asano, S. Theoretical study on the strain dependence of the magnetic anisotropy of X/Co(X=Pt, Cu, Ag, and Au) metallic multilayers. *Journal of Applied Physics* **79**, 7084–7089 (1996).

[67] Dieny, B. *et al.* Giant magnetoresistance in soft ferromagnetic multilayers. *Phys. Rev. B* **43**, 1297–1300 (1991).

[68] Tsymbal, E. Y. & Pettifor, D. G. Perspectives of giant magnetoresistance. *Solid State Physics - Advances in Research and Applications* **56**, 113–237 (2001).

[69] Parkin, S. S. P., Bhadra, R. & Roche, K. P. Oscillatory magnetic exchange coupling through thin copper layers. *Physical Review Letters* **66**, 2152–2155 (1991).

[70] Meiklejohn, W. & Bean, C. New Magnetic Anisotropy. *Phys. Rev.* **102**, 1413–1414 (1956).

[71] Cheng, S., Wun-Fogle, M., Restorff, J., Teter, J. & Hathaway, K. Magnetostrictive effects in Cu/Co/Cu/Fe spin valve structures. *Journal of Magnetism and Magnetic Materials* **148**, 344–345 (1995).

[72] Mamin, H. J., Gurney, B. A., Wilhoit, D. R. & Speriosu, V. S. High sensitivity spin-valve strain sensor. *Applied Physics Letters* **72**, 3220–3222 (1998).

[73] Löhndorf, M. *et al.* Strain sensors based on magnetostrictive GMR/TMR structures. *IEEE Transactions on Magnetics* **38**, 2826–2828 (2002).

[74] Duenas, T. *et al.* Micro-sensor coupling magnetostriction and magnetoresistive phenomena. *Journal of Magnetism and Magnetic Materials* **242-245**, 1132–1135 (2002).

[75] Florez, S. H. & Gomez, R. D. Strain-Induced Resistance Changes in CoFe/CuGMR Multilayers. *IEEE Transactions on Magnetics* **39**, 3411–3413 (2003).

[76] Dokupil, S., Bootsmann, M. T., Stein, S., Löhndorf, M. & Quandt, E. Positive/negative magnetostrictive GMR trilayer systems as strain gauges. *Journal of Magnetism and Magnetic Materials* **290-291**, 795–799 (2005).

115

[77] Áč, V., Anwarzai, B., Luby, S. & Majkova, E. Influence of mechanical strain on magnetic characteristics of spin valves. *Journal of Physics: Conference Series* **100**, 082025 (2008).

[78] Anwarzai, B., Ac, V., Luby, S., Majkova, E. & Senderak, R. Pseudo spin-valve on plastic substrate as sensing elements of mechanical strain. *Vacuum* **84**, 108–110 (2010).

[79] Luby, Š., Anwarzai, B., Áč, V., Majkova, E. & Senderák, R. Pseudo spin-valves with different spacer thickness as sensing elements of mechanical strain. *Vacuum* **86**, 718–720 (2012).

[80] Rizal, C., Gyawali, P., Kshattry, I. & Pokharel, R. K. Strain-induced magnetoresistance and magnetic anisotropy properties of Co/Cu multilayers. *Journal of Applied Physics* **111**, 07C107 (2012).

[81] Liu, L. *et al.* Magnetostrictive GMR spin valves with composite FeGa / FeCo free layers Magnetostrictive GMR spin valves with composite FeGa / FeCo free layers. *AIP Advances* **6**, 035206 (2016).

[82] Chopra, H. D., Yang, D. X., Chen, P. J., Parks, D. C. & Egelhoff, W. F. Nature of coupling and origin of coercivity in giant magnetoresistance NiO-Co-Cu-based spin valves. *Physical Review B* **61**, 9642–9652 (2000).

[83] Parkin, S. S. P. Origin of enhanced magnetoresistance of magnetic multilayers: Spin-dependent scattering from magnetic interface states. *Physical Review Letters* **71**, 1641–1644 (1993).

[84] Matsumoto, H., Ota, S., Ando, A. & Chiba, D. A flexible exchange-biased spin valve for sensing strain direction. *Applied Physics Letters* **114**, 132401 (2019).

[85] Julliere, M. Tunneling between ferromagnetic films. *Physics Letters* **54**, 225–226 (1975).

[86] Miyazaki, T. & Tezuka, N. Giant magnetic tunneling effect in Fe/Al$_2$O$_3$/Fe junction. *Journal of Magnetism and Magnetic Materials* **139**, 94–97 (1995).

[87] Moodera, J. S., Kinder, L. R., Wong, T. M. & Meservey, R. Large magnetoresistance at room temperature in ferromagnetic thin film tunnel junctions. *Physical Review Letters* **74**, 3273–3276 (1995).

[88] Butler, W. H., Zhang, X.-G., Schulthess, T. C. & MacLaren, J. M. Spin-dependent tunneling conductance of Fe|MgO|Fe sandwiches. *Physical Review B* **63**, 054416 (2001).

[89] Yuasa, S. & Djayaprawira, D. D. Giant tunnel magnetoresistance in magnetic tunnel junctions with a crystalline MgO(0 0 1) barrier. *Journal of Physics D: Applied Physics* **40**, 337–354 (2007).

[90] Yuasa, S., Nagahama, T., Fukushima, A., Suzuki, Y. & Ando, K. Giant room-temperature magnetoresistance in single-crystal Fe/MgO/Fe magnetic tunnel junctions. *Nature Materials* **3**, 868–871 (2004).

[91] Parkin, S. S. P. *et al.* Giant tunnelling magnetoresistance at room temperature with MgO (100) tunnel barriers. *Nature Materials* **3**, 862–867 (2004).

[92] Djayaprawira, D. D. *et al.* 230% room-temperature magnetoresistance in CoFeB/MgO/CoFeB magnetic tunnel junctions. *Applied Physics Letters* **86**, 092502 (2005).

[93] Tsunekawa, K. *et al.* Giant tunneling magnetoresistance effect in low-resistance CoFeB/MgO (001)/ CoFeB magnetic tunnel junctions for read-head applications. *Applied Physics Letters* **87**, 072503 (2005).

[94] Hayakawa, J., Ikeda, S., Matsukura, F., Takahashi, H. & Ohno, H. Dependence of giant tunnel magnetoresistance of sputtered CoFeB/MgO/CoFeB magnetic tunnel junctions on MgO barrier thickness and annealing temperature. *Japanese Journal of Applied Physics,* **44**, L587 (2005).

[95] Lee, Y. M., Hayakawa, J., Ikeda, S., Matsukura, F. & Ohno, H. Giant tunnel magnetoresistance and high annealing stability in CoFeB/MgO/CoFeB magnetic tunnel junctions with synthetic pinned layer. *Applied Physics Letters* **89**, 042506 (2006).

[96] Hayakawa, J., Ikeda, S., Lee, Y. M., Matsukura, F. & Ohno, H. Effect of high annealing temperature on giant tunnel magnetoresistance ratio of CoFeB/MgO/CoFeB magnetic tunnel junctions. *Applied Physics Letters* **89**, 87–90 (2006).

[97] Lee, Y. M., Hayakawa, J., Ikeda, S., Matsukura, F. & Ohno, H. Effect of electrode composition on the tunnel magnetoresistance of pseudo-spin-valve magnetic tunnel junction with a MgO tunnel barrier. *Applied Physics Letters* **90**, 212507 (2007).

[98] Ikeda, S. *et al.* Tunnel magnetoresistance of 604% at 300 K by suppression of Ta diffusion in CoFeB/MgO/CoFeB pseudo-spin-valves annealed at high temperature. *Applied Physics Letters* **93**, 082508 (2008).

[99] Ikeda, S. *et al.* A perpendicular-anisotropy CoFeB/MgO magnetic tunnel junction. *Nature Materials* **9**, 721–724 (2010).

[100] Tavassolizadeh, A. *et al.* Highly strain-sensitive magnetostrictive tunnel magnetoresistance junctions. *Journal of Magnetism and Magnetic Materials* **384**, 308–313 (2015).

[101] Tavassolizadeh, A. *et al.* Tunnel magnetoresistance sensors with magnetostrictive electrodes: Strain sensors. *Sensors* **16**, 1902 (2016).

[102] Fuji, Y. *et al.* Highly sensitive spintronic strain-gauge sensor based on a MgO magnetic tunnel junction with an amorphous CoFeB sensing layer. *Applied Physics Letters* **112**, 062405 (2018).

[103] Fuji, Y. *et al.* Spin-MEMS microphone integrating a series of magnetic tunnel junctions on a rectangular diaphragm. *Journal of Applied Physics* **123**, 163901 (2018).

[104] Dohmeier, N. *et al.* Inverse magnetostrictive stress sensors based on crossed pinned CoFeB/MgO/CoFeB tunnel junctions. *Journal of Applied Physics* **124**, 064501 (2018).

[105] Ota, S., Ando, A., Sekitani, T., Koyama, T. & Chiba, D. Flexible CoFeB / MgO-based magnetic tunnel junctions annealed at high temperature ($\geq 350°C$). *Applied Physics Letters* **115**, 202401 (2019).

[106] Ota, S. *et al.* CoFeB/MgO-based magnetic tunnel junction directly formed on a flexible substrate. *Applied Physics Express* **12**, 053001 (2019).

[107] Gowtham, P. G., Stiehl, G. M., Ralph, D. C. & Buhrman, R. A. Thickness-dependent magnetoelasticity and its effects on perpendicular magnetic anisotropy in Ta/CoFeB/MgO thin films. *Physical Review B* **93**, 024404 (2016).

[108] Higson, G. R. Recent advances in strain gauges. *Journal of Scientific Instruments* **41**, 405–414 (1964).

[109] Pritchard, E., Mahfouz, M., Evans, B., Eliza, S. & Haider, M. Flexible capacitive sensors for high resolution pressure measurement. *Proceedings of IEEE Sensors* 1484–1487 (2008).

[110] Liehr, S. *et al.* Polymer optical fiber sensors for distributed strain measurement and application in structural health monitoring. *IEEE Sensors Journal* **9**, 1330–1338 (2009).

[111] Raju, A. P. A. *et al.* Wide-area strain sensors based upon graphene-polymer composite coatings probed by raman spectroscopy. *Advanced Functional Materials* **24**, 2865–2874 (2014).

[112] Rosenberger, M., Hessler, S., Belle, S., Schmauss, B. & Hellmann, R. Compressive and tensile strain sensing using a polymer planar Bragg grating. *Optics Express* **22**, 5483 (2014).

[113] Yi, F. *et al.* Stretchable-rubber-based triboelectric nanogenerator and its application as self-powered body motion sensors. *Advanced Functional Materials* **25**, 3688–3696 (2015).

[114] Zhou, J. *et al.* Flexible piezotronic strain sensor. *Nano Letters* **8**, 3035–3040 (2008).

[115] Yamada, T. *et al.* A stretchable carbon nanotube strain sensor for human-motion detection. *Nature Nanotechnology* **6**, 296–301 (2011).

[116] Xiao, X. *et al.* High-strain sensors based on ZnO nanowire/polystyrene hybridized flexible films. *Advanced Materials* **23**, 5440–5444 (2011).

[117] Muth, J. T. *et al.* Embedded 3D printing of strain sensors within highly stretchable elastomers. *Advanced Materials* **26**, 6307–6312 (2014).

[118] Amjadi, M., Pichitpajongkit, A., Lee, S., Ryu, S. & Park, I. Highly stretchable and sensitive strain sensor based on silver nanowire-elastomer nanocomposite. *ACS Nano* **8**, 5154–5163 (2014).

[119] Yan, C. *et al.* Highly stretchable piezoresistive graphene-nanocellulose nanopaper for strain sensors. *Advanced Materials* **26**, 2022–2027 (2014).

[120] Boland, C. S. *et al.* Sensitive, high-strain, high-rate bodily motion sensors based on graphene-rubber composites. *ACS Nano* **8**, 8819–8830 (2014).

[121] Jeong, Y. R. *et al.* Highly Stretchable and Sensitive Strain Sensors Using Fragmentized Graphene Foam. *Advanced Functional Materials* **25**, 4228–4236 (2015).

[122] Gong, S. *et al.* Tattoolike Polyaniline Microparticle-Doped Gold Nanowire Patches as Highly Durable Wearable Sensors. *ACS Applied Materials and Interfaces* **7**, 19700–19708 (2015).

[123] Amjadi, M., Kyung, K. U., Park, I. & Sitti, M. Stretchable, Skin-Mountable, and Wearable Strain Sensors and Their Potential Applications: A Review. *Advanced Functional Materials* **26**, 1678–1698 (2016).

[124] Zang, Y., Zhang, F., Di, C. A. & Zhu, D. Advances of flexible pressure sensors toward artificial intelligence and health care applications. *Materials Horizons* **2**, 140–156 (2015).

[125] Kim, K. K. *et al.* Highly Sensitive and Stretchable Multidimensional Strain Sensor with Prestrained Anisotropic Metal Nanowire Percolation Networks. *Nano Letters* **15**, 5240–5247 (2015).

[126] Dai, G. *et al.* Controllable strain-induced uniaxial anisotropy of $Fe_{81}Ga_{19}$ films deposited on flexible bowed-substrates. *Journal of Applied Physics* **114**, 173913 (2013).

[127] Qiao, X. *et al.* Tuning magnetic anisotropy of amorphous CoFeB film by depositing on convex flexible substrates. *AIP Advances* **6**, 056106 (2016).

[128] Uchida, K. *et al.* Observation of the spin Seebeck effect. *Nature* **455**, 778–781 (2008).

[129] Bauer, G. E., Saitoh, E. & Van Wees, B. J. Spin caloritronics. *Nature Materials* **11**, 391–399 (2012).

[130] Flipse, J. *et al.* Observation of the spin peltier effect for magnetic insulators. *Physical Review Letters* **113**, 027601 (2014).

[131] Daimon, S., Iguchi, R., Hioki, T., Saitoh, E. & Uchida, K. I. Thermal imaging of spin Peltier effect. *Nature Communications* **7**, 13754 (2016).

[132] Iguchi, R. *et al.* Thermographic measurements of spin-current-induced temperature modulation in metallic bilayers. *Physical Review B* **98**, 014402 (2018).

[133] Seki, T., Iguchi, R., Takanashi, K. & Uchida, K. Visualization of Anomalous Ettingshausen Effect in a Ferromagnetic Film: Direct Evidence of Different Symmetry from Spin Peltier Effect. *Applied Physics Letters* **122**, 152403 (2018).

[134] Smith, A. W. The transverse thermomagnetic effect in nickel and cobalt. *Physical Review (Series I)* **33**, 295–306 (1911).

[135] Kimura, T., Otani, Y., Sato, T., Takahashi, S. & Maekawa, S. Room-temperature reversible spin hall effect. *Physical Review Letters* **98**, 156601 (2007).

[136] Ota, S., Uchida, K., Iguchi, R., Thach, P. V. & Awano, H. Strain-induced switching of heat current direction generated by magneto-thermoelectric effects. *Scientific Reports* **9**, 13197 (2019).

[137] Straube, H., Wagner, J. M. & Breitenstein, O. Measurement of the Peltier coefficient of semiconductors by lock-in thermography. *Applied Physics Letters* **95**, 052107 (2009).

[138] Wid, O. *et al.* Investigation of the unidirectional spin heat conveyer effect in a 200 nm thin Yttrium Iron Garnet film. *Scientific Reports* **6**, 28233 (2016).

[139] Iguchi, R. & Uchida, K. Charge-current angle and frequency dependences of the spin Peltier effect induced by the spin Hall effect. *Japanese Journal of Applied Physics* **57**, 0902B6 (2018).

[140] Uchida, K., Daimon, S., Iguchi, R. & Saitoh, E. Observation of anisotropic magneto-Peltier effect in nickel. *Nature* **558**, 95–99 (2018).

[141] Das, R., Iguchi, R. & Uchida, K. Systematic Investigation of Anisotropic Magneto-Peltier Effect and Anomalous Ettingshausen Effect in Ni Thin Films. *Physical Review Applied* **11**, 034022 (2019).

[142] Novosad, V. *et al.* Novel magnetostrictive memory device. *Journal of Applied Physics* **87**, 6400 (2000).

[143] Giri, D., Vacca, M., Causapruno, G., Zamboni, M. & Graziano, M. Modeling, Design, and Analysis of MagnetoElastic NML Circuits. *IEEE Transactions on Nanotechnology* **15**, 977–985 (2016).

[144] Bozorth, R. M. Magnetostriction and crystal anisotropy of single crystals of hexagonal cobalt. *Physical Review* **96**, 311–316 (1954).

[145] Hubert, A., Unger, W. & Kranz, J. Messung der Magnetostriktionskonstanten des Kobalts als Funktion der Temperatur. *Zeitschrift für Physik* **224**, 148–155 (1969).

[146] Bruno, P. Magnetic surface anisotropy of cobalt and surface roughness effects within Neel's model. *Journal of Physics F: Metal Physics* **18**, 1291–1298 (1988).

Publication list

1. <u>S. Ota</u>, Y. Hibino, D. Bang, H. Awano, T. Kozeki, H. Akamine, T. Fujii, T. Namazu, T. Takenobu, T. Koyama and D. Chiba,
"Strain-induced reversible modulation of the magnetic anisotropy in perpendicularly magnetized metals deposited on a flexible substrate",
Applied Physics Express **9**, 043004 (2016).
http://doi.org/10.7567/APEX.9.043004

2. R. Asai, <u>S. Ota</u>, T. Namazu, T. Takenobu, T. Koyama and D. Chiba,
"Stress-induced large anisotropy field modulation in Ni films deposited on a flexible substrate",
Journal of Applied Physics **120**, 083906 (2016).
http://dx.doi.org/10.1063/1.4961564

3. Y. Hibino, T. Koyama, A. Obinata, T. Hirai, <u>S. Ota</u>, K. Miwa, S. Ono, F. Matsukura, H. Ohno, and D. Chiba,
"Peculiar temperature dependence of electric-field effect on magnetic anisotropy in Co/Pd/MgO system",
Applied Physics Letters **109**, 082403 (2016).
https://doi.org/10.1063/1.4961621

4. <u>S. Ota</u>, A. Ando and D. Chiba,
"A flexible giant magnetoresistive device for sensing strain direction",
Nature Electronics **1**, 124 (2018).
https://doi.org/10.1038/s41928-018-0022-3

5. S. Ota, M. Ono, H. Matsumoto, A. Ando, T. Sekitani, R. Kohno, S. Iguchi, T. Koyama and D. Chiba,
   "CoFeB/MgO-based magnetic tunnel junction directly formed on a flexible substrate",
   Applied Physics Express **12**, 053991 (2019).
   https://doi.org/10.7567/1882-0786/ab0dca

6. H. Matsumoto, S. Ota, A. Ando and D. Chiba,
   "A flexible exchange-biased spin valve for sensing strain direction",
   Applied Physics Letters **114**, 132401 (2019).
   https://doi.org/10.1063/1.5091033

7. S. Ota, K. Uchida, R. Iguchi, P.V. Thach, H. Awano and D. Chiba,
   "Strain-induced switching of heat current direction generated by magneto-thermoelectric effects",
   Scientific Reports **9**, 13197 (2019).
   https://doi.org/10.1038/s41598-019-49567-2

8. K. Ochi, T. Hirai, S. Ota, T. Koyama, T. Sekitani and D. Chiba,
   "Solid-state capacitor for voltage control of magnetism formed on a flexible substrate",
   Japanese Journal of Applied Physics, **58**, 118003 (2019).
   https://doi.org/10.7567/1347-4065/ab4de9

9. S. Ota, A. Ando, T. Sekitani, T. Koyama and D. Chiba,
   "Flexible CoFeB/MgO-based magnetic tunnel junctions annealed at high temperature ($\geq 350°C$)",
   Applied Physics Letters **115**, 202401 (2019).
   https://doi.org/10.1063/1.5128952

Acknowledgments